UNIVERSITEIT VAN PRETORIA
UNIVERSITY OF PRETORIA
YUNIBESITHI YA PRETORIA

Haul road defect identification and condition assessment using measured truck response

by

Daniel Hugo

A dissertation submitted in partial fulfilment of
the requirements for the degree

Master of Engineering

in the

Department of Mechanical and Aeronautical Engineering
Faculty of Engineering, the Built Environment and Information Technology

University of Pretoria
Pretoria

January 2005

Haul road defect identification and condition assessment using measured truck response

Author Daniel Hugo
Supervisors Professors P.S. Heyns and R.J. Thompson
Department Department of Mechanical and Aeronautical Engineering
Degree Master of Engineering

Abstract

Mine haul road maintenance is traditionally done at scheduled intervals or after regular inspection. Both these methods can lead to unwarranted expenditure, either through over-maintaining the road, or failure to recognise significant deterioration, resulting in an increase in vehicle operating costs. Predictive maintenance management models for unpaved roads have been developed in recent years. These methods work well in a trivial environment where variables such as traffic volume can be predicted. However, many mining systems are too complex for such models to be effective.

This work investigates the possibility of using haul truck response to aid haul road maintenance management. The approach adopted for the study was twofold: Firstly, can truck response data be used to recognise specific road defects, in terms of location, type and size? This is important since different defect types require different road maintenance strategies. Secondly, can road roughness be measured on a qualitative basis?

With the emphasis on road defect reconstruction, a mathematical modelling approach was adopted. The truck was characterised in terms of its suspension and tyre properties. Dynamic truck response data was acquired during field measurements in which the vehicle was driven over defects of known dimensions. With these data sets available, mathematical modelling and simulation was possible.

Quarter vehicle and seven degree of freedom vehicle models played a vital role in this work by laying a foundation in the use of haul truck response for the purpose of road defect reconstruction. A modelling methodology that is based on dynamic equilibrium of an independent front unsprung mass of the truck is proposed in which the vertical dynamic tyre force and eventually the road geometry is calculated. It is shown that defects can be reconstructed from measured truck response data with an accuracy sufficient to fulfil the requirements of defect recognition for road maintenance management purposes.

Secondly, a preliminary investigation into the qualitative assessment of road condition via truck response measurements was conducted. The inherent response properties of the truck pertaining to road roughness measurement were studied and some correlation

between measured suspension motion and road roughness measured with a high speed profilometer was found.

Keywords

Mine haul road maintenance management, road defect identification, mine haul trucks, off-road vehicles, vehicle modelling, hydro-pneumatic suspension struts, road roughness assessment

Acknowledgements

I gladly thank the following people.

My supervisors Professors Stephan Heyns and Roger Thompson for their continual support and assistance. Also for the exposure to many aspects they gave me through this opportunity.

Professor Alex Visser for his role in structuring the project.

Mr. Schalk Els for his involvement and advice.

Mr. Frans Windell for his assistance during measurements and characterisation.

Mr. Jimmy Troup and personnel of the Structural Test Facility at Denel Aviation for accommodating and participating in the suspension strut characterisation at their facility.

Mr. Jeff van der Merwe of Denel LIW for allowing and arranging the use of their actuator in the suspension strut characterisation.

Messrs. Rico van Staden, Gerrit van der Merwe and Gert Horn of Kumba Resources (Grootegeluk Coal Mine) for their assistance during and between measurements at the mine.

Messrs. Bill Boshoff and Herman Potgieter of Komatsu Mining Southern Africa for their continual collaboration and assistance.

Mr. Michael Abbott of CT Hydraulics for hosting visits to their premises with the permission of Komatsu Mining Southern Africa.

Finally, I thank the Spirit of God who empowered me and has been the joy inside of me so many days; the Lord Jesus Christ for this great learning opportunity and His gracious attitude towards me.

The research was made possible through the support of my industry partners, Kumba Resources and De Beers Venetia Mine, as well as the Technology and Human Resources for Industry Programme (THRIP) managed by the National Research Foundation (NRF) and financed by the Department of Trade and Industry.

Contents

Nomenclature

List of symbols

a_1, a_2	length
a_x	vehicle longitudinal acceleration
A	effective inside area of the suspension strut
b, b_1, b_2, …	length
c	length
c_s	suspension damping constant
C	parameter that describes the suspension strut stiffness characteristic
C_{port}	parameter that describes the pressure difference over a port
$C_{damping}$	parameter that describes the suspension strut damping force
d_1, d_2	distance
e	distance
f_{nroll}	roll natural frequency
f_{ns}	bounce natural frequency
f_{nu}	wheel hop frequency
F_{damper}, $F_{damping}$	suspension or suspension strut damping force
F_i	suspension strut spring force at state i
F_R	traction force at the rear wheels
F_s	force on the sprung mass
F_{spring}	suspension spring force
F_{static}	suspension strut spring force at the static position
$F_{suspension}$, F_{suspF1}, F_{suspF2}, ...	total force in the suspension strut
F_{suspR}	total force in the rear suspensions struts
F_{tyre}, F_{tyreF1}, F_{tyreF2}, ...	tyre force
F_{TX}	trailing arm force in the x direction
F_{TY}	trailing arm force in the y direction
F_u	force on the unsprung mass
H_m	measured defect height
H_r	reconstructed defect height

$I_{\theta s}$, $I_{\phi s}$, $I_{\phi uR}$	mass moment of inertia
k_{pitch}	pitch radius of gyration
k_{roll}	roll radius of gyration
k_s	suspension spring stiffness constant
k_{sf}	front suspension strut stiffness constant
k_{sr}	rear suspension strut stiffness constant
k_t	tyre vertical stiffness constant
k_{tf}	front tyre vertical stiffness constant
k_{tr}	dual rear tyre vertical stiffness constant
k_{fRR}	front ride rate
k_{rRR}	rear ride rate
L	length
L_f	front suspension strut separation distance
L_r	rear suspension strut separation distance
m	component mass, vehicle mass or gas mass
m_i	gas mass at state i
m_u, m_{uR}, m_{uF1}, ...	unsprung mass
M_s, M_q	sprung mass
M_{R1}, M_{R2}	axle bending moment
n	polytropic exponent
N_R	normal force at the rear wheels (i.e. tyre force)
P	gas pressure
P_c	critical pressure
P_i	gas pressure at state i
P_r	reduced pressure
P_{static}	pressure inside the suspension strut at the static position
R	gas constant
S	vehicle speed
S_{R1}, S_{R2}	axle shear force
T	gas temperature
T_c	critical temperature
T_i	gas temperature at state i
T_r	reduced temperature
V	gas volume

V_{port}	velocity of fluid flowing through a port
V_i	gas volume at state i
V_{static}	gas volume inside the suspension strut at the static position
$V_{suspension}$	relative velocity of the suspension strut
W_f	treadband filtered defect width
W_m	measured defect width
W_r	reconstructed defect width
x_i	gas height inside the suspension strut at state i
x_{static}	gas height inside the suspension strut at the static position
z	compressibility factor
z_r , z_{rF1} , …	road input displacement
z_s	sprung mass vertical displacement
z_{sF1}	sprung mass vertical displacement at location $sF1$
z_u , z_{uR} , z_{uF1} , …	unsprung mass vertical displacement
ΔP_{port}	pressure difference over a port
Δz_i	relative suspension strut displacement from the static position at state i
θ_s	rotational pitch displacement
ϕ_s , ϕ_{uR}	rotational roll displacement
ω	radial frequency

Operations

$\dot{(\ )}$	$\frac{d(\ )}{dt}$
$\ddot{(\ )}$	$\frac{d^2(\ )}{dt^2}$
$L\{\ \}$	Laplace transform of $\{\ \}$

Abbreviations

7DOF	Seven Degree of Freedom
GPS	Global Positioning System
HSP	High Speed Profilometer
IRI	International Roughness Index

LVDT	Linear Variable Displacement Transducer
PDRM	Preliminary Dynamic Response Measurements
RDRM	Refined Dynamic Response Measurements

Chapter 1

Introduction

1.1 The current state of haul road maintenance management

A changing economic climate and increasing size and variation in the design of haul trucks are creating increasing interest in the design and maintenance of open cast mine haul roads (Thompson & Visser, 2000).

Design of haul roads comprises structural and functional design. Structural design refers to the ability of a road to carry imposed loads over its design life without the need for excessive maintenance. Functional design mainly comprises the choice of wearing course material type with the purpose to create a safe, economic and vehicle friendly environment. Maintenance is very much related to both of these and an important aspect to consider during the design of a road. The structural and functional design of a road influences the frequency and type of maintenance required.

High haul road deterioration rates lead to maintenance intensive roads and management of maintenance is therefore important. Too little maintenance leads to excessive vehicle operation and maintenance costs, while excessive maintenance increases costs but produces little benefit in vehicle operation and reduced vehicle maintenance. Existing maintenance techniques such as *ad hoc blading* and *scheduled blading* fail to optimise this complex cost function. Ad hoc blading is typically managed by regular inspection of the road network and subjective assessment of road segment functionality. Scheduled blading refers to maintenance according to a fixed schedule. These techniques have potential to generate excessive costs due to over- or under-maintenance.

Thompson and Visser (2003) developed a *maintenance management system* applicable to haul roads. In this method empirical models are developed to describe the relation between appropriate cost factors and the road condition. From these, a change in road condition can be related to cost. They realize an important difference between haul road maintenance and public road maintenance – the company responsible for haul road design and maintenance also carry vehicle operating and maintenance costs. The aim for a mining company should therefore be to minimise the total cost (the combination of vehicle operating and road maintenance costs). Part of this maintenance management system is a visual assessment method that rates road defects according to their types and degrees of severity. The sum of defect ratings for a segment of road forms a defect score, which is related to rolling resistance through an empirical model. Every cost factor,

including fuel consumption, tyre consumption and vehicle maintenance on the one hand and road maintenance costs on the other hand, is then related empirically to the road defect score. Road deterioration rates after maintenance are also modelled. Combining these empirical models and optimising, it is possible to determine the optimal maintenance interval. There will be a certain maintenance interval that will keep the road from deteriorating to such a state (resulting in a high road defect score) that vehicle operating and maintenance costs would be so high that all cost savings resulting from a reduced maintenance interval are counteracted.

Current haul road maintenance management systems schedule maintenance based on prediction and are therefore very dependent on accurate inputs for their success. Thompson et al. (2003) note limitations of this technique. This method can be applied relatively easily for situations where segment characteristics are quasi-static and rapid changes are predictable (typical changes are hauling from another ramp, a change in tonnage hauled between ramps, etc.). For complex road networks where material is sourced and hauled from a large and highly variable number of loading points, repeated remodelling is necessary with no guarantee that variables assumed (e.g. traffic volume) will be realised.

The deficiency of these techniques – scheduled blading, ad hoc blading and maintenance management systems – leads to a quest for alternatives.

1.2 Vehicle response as a tool in paved road maintenance management

The use of vehicle response measurements to assess the condition of roads is not new. Over the years different systems have been developed to measure road quality. Some of these measure actual road profiles, while others describe the road in some indirect fashion. Bennett (2004) refers to Sayers et al. (1986) and discusses four classes of profilers

- Class 1: Precision profilers – *measure actual road profile.*
- Class 2: Other direct measuring profilers such as high speed profilometers (HSP) – *measure actual road profile.*
- Class 3: Response-type measurements or simple profilers – *measure road roughness indirectly.*
- Class 4: Subjective ratings – *subjective evaluation or indirect measurement of road roughness.*

Profilers based on vehicle response are generally either class 2 or class 3 profilers. Class 2 profilers in the form of high speed profilometers (HSP) measure road profile directly.

Class 3 profilers measure road profile indirectly, usually as suspension motion or its equivalent and is known as response-type systems. Appendix A contains more detail on these four classes of profilers.

Profiles measured with different instrumentation can be related through the International Roughness Index (IRI). IRI is probably the most popular measure of road roughness, used in both paved and unpaved road maintenance management systems. The difference however, is that unpaved road maintenance management systems use predicted road roughness information while paved road maintenance management systems use measured road roughness information.

The question that arises is why standard road profilers have never found application in unpaved road maintenance management schemes. Some reasons are

- Haul road maintenance in particular is done much more frequently than paved road maintenance. This means that haul roads will have to be profiled much more often than paved roads. Thus, a far greater more effort would be required, even if the agency maintaining the roads has unlimited access to a profiler.
- Not all profilers are suitable for deployment on unpaved roads. Archondo-Callao (1999b) mentions that the fragility of roughness measurement instruments makes them unsuitable such roads.
- Profiling methods might not have been considered to date, simply because existing maintenance techniques have sufficed until recently. However, larger haul trucks cause more rapid road deterioration rates than in the past.

None of the abovementioned reasons in essence excludes the possibility of a profiler being developed for the purpose of haul road condition assessment. Investigation into the viability of such a concept is not the topic of the current research, however. The current work investigates the possibility of using operational vehicles (haul trucks specifically) to aid haul road maintenance management decisions.

1.3 Haul truck response as a road maintenance management tool

The fact that paved road maintenance agencies use vehicles set apart for the purpose of profiling, is per se no indication that operational vehicles cannot be useful in some unpaved road maintenance management applications. As noted in section 1.1, the agency maintaining a paved road and the users of the road are normally independent. Consequently, paved road maintenance agencies use vehicles for the sole purpose of profiling. Since the total cost concept applies to the mining industry, it is appropriate to investigate the possible use of operational mine vehicles.

Haul roads are designed and maintained for the purpose of hosting vehicles that are part of the mining operation, of which haul trucks are foremost. Haul trucks have been chosen for the current research because they travel these roads most frequently and have the largest impact of all vehicles on road deterioration and vehicle operating cost that is influenced by the road condition. Moreover, it is possible to install positioning and communication equipment on these vehicles to communicate captured data and truck locations to a maintenance dispatch office. In fact, such equipment is standard on many mines.

The use of truck response measurements renders huge potential advantages over existing maintenance management techniques

- Utilising truck response has the potential for thorough, yet less labour intensive assessment. Thorough, since every stretch of road the truck drives over is assessed. The quality of assessment obviously depends on the ability and sophistication of techniques. Less labour intensive, since truck response can be measured and processed automatically – frequent visual inspection of long sections of road is not necessary.
- The inherent objectivity of truck response measurements is a second major advantage. Most of the existing techniques contain some form of visual inspection. Even maintenance management systems are derived from subjective measures in the form of human inspection.
- Thirdly, truck response measurements, as opposed to maintenance management systems, have great potential to identify localised defects.

Using operational vehicles also has advantages over specialised profilers

- There will be no concern about using a fragile profiler in harsh environments, since vehicles operate in their normal environments.
- These vehicles can capture road condition data while operating. This is a major advantage considering the requirement of frequent assessment. Specialised profilers require operation for the specific purpose of profiling.

Disadvantages of using operational vehicles as opposed to specialised profilers

- Specialised profilers can be designed and chosen to have the most desirable properties for the purpose of road profiling. Operational vehicles cannot, because they serve other functions that might require properties contrary to those ideal for profiling.
- The primary function of operational vehicles (hauling material) probably requires less strict control over dynamic response properties than would be the case for some profiling purposes. Consequently, difficulty might be experienced in establishing adequate levels of control over vehicle properties such as suspension strut pressure, tyre pressure and load.

1.4 The scope of this research

Recognising the deficiencies of current techniques in the mining environment and the potential benefits of haul trucks as a tool, this research aims to establish a basis in the use of haul truck response for the purpose of haul road maintenance management.

The ability to identify and maintain localised haul road defects, is desirable in an effort to minimise vehicle operating and maintenance costs. Apart from identifying defect locations on a qualitative basis, the ability to identify defects in terms of type and size will be advantageous, since the types and sizes of defects determine maintenance strategies. This work adopts a mathematical vehicle modelling approach and utilises measured haul truck response in pursuing this objective of reconstructing large defect geometries to aid road maintenance decisions.

The importance of road roughness evaluations in the management of road maintenance in general and for haul roads in particular is expressed in the preceding sections of this chapter. From the literature it is clear that objective evaluations are superior to subjective or predictive evaluations. This research further aims to introduce the concept of using haul truck response as a measure of road roughness and enhance understanding in its viability.

Haul truck response is used to pursue the abovementioned objectives but, given the pivotal role of haul trucks in the mining operation as a whole, and the associated vehicle design limitations, this work does not aim to redesign vehicles to facilitate response measurements.

1.5 Document overview

Chapter 2 commences by recognising different vehicle excitation sources. Quarter and seven degree of freedom (7DOF) vehicle models are introduced, after which a measurement methodology for the purpose of road defect reconstruction is proposed and dynamic tyre force measurement methods in the literature are discussed. The last few sections of this chapter are dedicated to the four aspects of tyre enveloping, tyre/wheel non-uniformities, wheelbase filtering and friction in the suspension strut, and their influence on the current work.

The haul truck that was used in this research is introduced in chapter 3. The rest of the chapter is devoted to vehicle response measurements and component characterisation. An initial set of online measurements served to introduce the vehicle and its operating environment. This was followed by a refined set of measurements that concentrated on

the front of the vehicle; the methodology proposed in chapter 2 primarily motivated this measurement configuration. The tyres of the haul truck were characterised in terms of their vertical stiffness and the damping and stiffness characteristics of a front suspension strut were determined.

The background that is provided in chapter 2 and the data acquisition that is discussed in chapter 3, lay the foundation for the work presented in chapter 4. This chapter is devoted to truck modelling and defect reconstruction. Computer simulations of the road test section over which the haul truck drove during the refined set of vehicle response measurements are discussed. Hereafter, tyre models that were used in this research are discussed and the rigid body assumption is motivated. This is followed by a comparison between quarter vehicle simulation results and measured response. Limitations of the quarter vehicle simulations lead to a quest for deeper understanding of the dynamics of the vehicle. The bounce and pitch natural frequencies of the vehicle were determined, which also enabled frequency ranges in which rigid body motion dominates, to be established. These aspects are discussed, after which it is verified that suspension strut forces can be calculated accurately when large defects are encountered. The 7DOF vehicle model presented in chapter 2 was utilised for this purpose. This model was also used in simulations, of which results are presented and further interpreted. A discussion on the necessity of including the vertical force in the trailing arm and longitudinal acceleration effects follows since these were neglected in the derivation of the 7DOF model. Finally, defect reconstruction is discussed and results are presented.

In the light of the truck modelling, measurements and analyses presented in chapters 2, 3 and 4, some of the concepts surrounding qualitative road roughness assessment are contextualised in chapter 5. The IRI is introduced as the standard for road roughness measurement. The desire to have an objective evaluation of the roughness of haul roads is expressed, after which the response characteristics of the haul truck that pertains to road roughness measurements is studied. Finally, truck suspension motion is analysed in terms of its usefulness as a measure of road roughness.

Chapter 6 offers conclusions and recommendations for further research.

Chapter 2

Vehicle modelling

2.1 Vehicle excitation sources

Gillespie (1992) identifies several sources of excitation that influence the response of a vehicle. These sources have different origins and can generally be classified into two classes – road roughness and on-board sources. Figure 2.1 gives a schematic picture of a vehicle as a dynamic system. The two classes of excitation sources are shown as inputs to the vehicle. The vehicle alters these inputs according to its response properties and produces outputs in the form of vibrations.

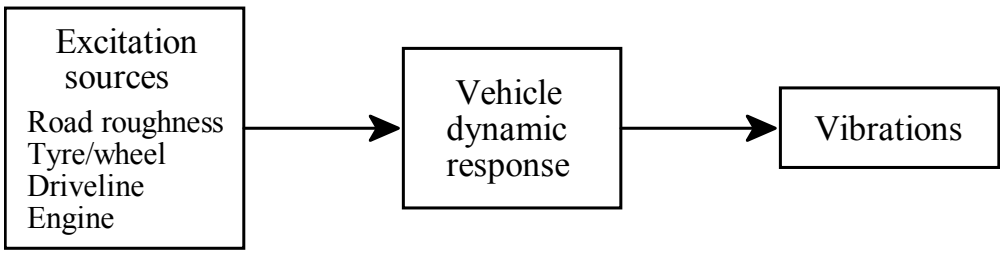

Figure 2.1 The vehicle as dynamic system (adapted from Gillespie, 1992).

2.2 Quarter vehicle modelling

A quarter vehicle model is the most basic used to study vertical vehicle dynamics. Figure 2.2 shows a schematic diagram of such a model with linear properties. Modelling from the equilibrium position, the differential equations that describe this system are

$$M_s\ddot{z}_s = -k_s(z_s - z_u) - c_s(\dot{z}_s - \dot{z}_u) \tag{2.1}$$

$$m_u\ddot{z}_u = k_s(z_s - z_u) + c_s(\dot{z}_s - \dot{z}_u) - k_t(z_u - z_r) \tag{2.2}$$

where the road input displacement z_r, the unsprung mass displacement z_u and the sprung mass displacement z_s are functions of time. This reduced notation is used consistently throughout the dissertation. M_s is the sprung mass, m_u is the unsprung mass, k_s is the suspension stiffness, c_s is the suspension damping and k_t is the vertical tyre stiffness. Appendix B presents the coordinate system that is adopted.

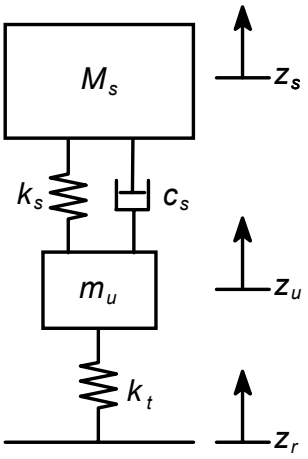

Figure 2.2 Linear quarter vehicle model.

Since this model has linear properties, it is possible to calculate frequency domain transfer functions between various inputs and responses. Appendix C derives amongst others, transfer functions between the road input and the unsprung and sprung mass motions. Frequency domain transfer functions are only valid for steady state response.

The validity of assuming linear vehicle characteristics depends on the application and desired accuracy of results. Johansson and Gustavsson (2000) mention that linear models are often sufficient to model vertical dynamics for road induced vibrations in the concept stage of a new design project.

Figure 2.3 shows a quarter vehicle model with non-linear suspension properties. As with the model in figure 2.2, the tyre is represented as a simple linear spring and damping is neglected. Modelling from the equilibrium position, the differential equations that describe this system are

$$M_s \ddot{z}_s = F_{spring} + F_{damper} \tag{2.3}$$

$$m_u \ddot{z}_u = F_{tyre} - F_{spring} - F_{damper} \tag{2.4}$$

where $F_{spring} = f(z_s, z_u)$, $F_{damper} = f(\dot{z}_s, \dot{z}_u)$ and $F_{tyre} = -k_t(z_u - z_r)$.

Since suspension properties are non-linear and therefore dependent on vehicle motion, it is not possible to derive transfer functions for this model. This causes attention to focus on time domain modelling techniques. When the aim is to use vehicle response to identify road inputs, some sort of inverse problem is under consideration. Through the transfer functions derived in Appendix C, linear system inversion is possible. Once time domain methods are embraced however, inversion becomes a concern.

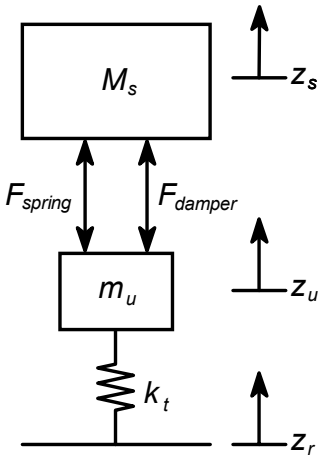

Figure 2.3 Non-linear quarter vehicle model.

All the models presented in this dissertation are described in terms of their static equilibrium positions. For the non-linear models it is therefore important to establish the equilibrium positions on their non-linear suspension spring characteristic curves, from which the dynamic force components can be calculated.

The usefulness and limitations of quarter vehicle models

Bounce and pitch motions are uncoupled if the bounce natural frequencies of quarter vehicle models that respectively represent the front and rear of a vehicle are equal. In that case, the pitch oscillation centre is at the centre of gravity and the bounce oscillation centre is at infinity. Consequently, the quarter vehicle model representative of either the front or rear of the vehicle can be used to simulate vertical motion of the centre of gravity of the sprung mass. If bounce and pitch motions are coupled, the quarter vehicle model that represents the front or rear of a vehicle should still be useful to simulate the vertical motion of the centre of gravity at the predominantly bounce natural frequency. This is true for most vehicles since good ride behaviour requires the front and rear bounce natural frequencies to be close together (Olley, edited by Milliken & Milliken, 2002).

Quarter vehicle models cannot simulate pitch motion, whether it appears at the centre of gravity, the front or rear of the vehicle. The effect of this inability on simulation results depends on the location of the pitch oscillation centre with respect to the part of the vehicle that is being modelled. Quarter vehicle models can also not model roll motion.

2.3 Seven degree of freedom (7DOF) vehicle models

Rigid body models with progressively more degrees of freedom than quarter vehicle models are: pitch-plane, 7DOF and full vehicle models. In some analyses it is required to expand rigid body models and allow deformation of some components.

Figure 2.4 shows a 7DOF rigid body model with two independent front unsprung masses and a solid rear axle. The model allows vertical, pitch and roll motion of the sprung mass, vertical motion of the two independent front unsprung masses and vertical and roll motion of the solid rear axle. Such models often also contain longitudinal and lateral degrees of freedom of the sprung mass. To include these degrees of freedom, without neglecting the degrees of freedom of the unsprung masses, would make the model much more complex. Inclusion of the degrees of freedom of the unsprung masses was considered important in the current research, and therefore the longitudinal and lateral degrees of freedom of the sprung mass were not included in this model. This model is representative of the haul truck that was used in this research, if the vertical force in the trailing arm is neglected.

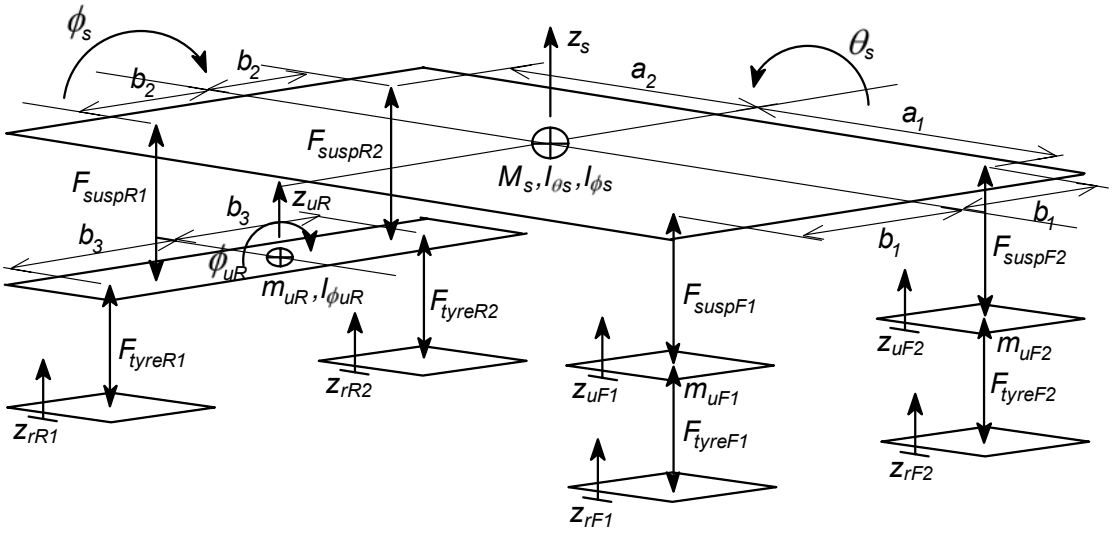

Figure 2.4 Schematic presentation of a seven degree of freedom vehicle model.

The equations of motion that describe this model are, for the sprung mass

$$F_{suspF1} + F_{suspF2} + F_{suspR1} + F_{suspR2} = M_s \ddot{z}_s \tag{2.5}$$

$$(F_{suspF1} + F_{suspF2})a_1 - (F_{suspR1} + F_{suspR2})a_2 = I_{\theta s}\ddot{\theta}_s \tag{2.6}$$

$$(F_{suspF1} - F_{suspF2})b_1 + (F_{suspR1} - F_{suspR2})b_2 = I_{\phi s}\ddot{\phi}_s \tag{2.7}$$

and for the unsprung masses

$$-F_{suspF1} + F_{tyreF1} = m_{uF1}\ddot{z}_{uF1} \tag{2.8}$$

$$-F_{suspF2} + F_{tyreF2} = m_{uF2}\ddot{z}_{uF2} \tag{2.9}$$

$$-(F_{suspR1} + F_{suspR2}) + (F_{tyreR1} + F_{tyreR2}) = m_{uR}\ddot{z}_{uR} \tag{2.10}$$

$$(F_{suspR2} - F_{suspR1})b_2 + (F_{tyreR1} - F_{tyreR2})b_3 = I_{\phi uR}\ddot{\phi}_{uR} \tag{2.11}$$

where M_s is the sprung mass, m_{uF1} and m_{uF2} are the two front unsprung masses and m_{uR} is the rear unsprung mass. z_s, z_{uF1}, z_{rF1}, … are vertical displacements, θ_s and ϕ_s are respectively the sprung mass pitch and roll displacements and ϕ_{uR} is the rear unsprung mass roll displacement. The nomenclature contains a description of all the variables in figure 2.4.

2.4 Modelling and measurement pertaining to road input reconstruction

Methods are available to study the response of a vehicle to excitation from individual sources. The combination of inputs from different sources however produces complex vehicle-weighted responses. The use of vehicle response to identify road inputs therefore requires differentiation between response caused by road inputs and response induced by other sources. To a large extent, this is not an unreasonable objective since responses from road inputs and responses from other sources mainly appear in different frequency ranges. However, measurement locations can be chosen in such a way to minimise influence from unwanted excitation sources.

Figure 2.5 shows the rigid free body diagram of an independent front unsprung mass of the haul truck that was used in this research. If acceleration of the unsprung mass $\ddot{z}_u$ and forces acting between the sprung and unsprung masses $F_{suspension}$ are measured, the road force F_{tyre} can be calculated through a simple algebraic equation

$$F_{tyre} = m_u\ddot{z}_u + F_{suspension} \tag{2.12}$$

The advantage of this measurement configuration is firstly that neither structural vibrations nor vibrations from other on-board sources significantly contaminate measured signals in the frequency range below 10 Hz. This is verified in chapter 4 through analysis of measured data.

The haul truck was equipped with hydro-pneumatic suspension struts that exhibit non-linear spring and damper characteristics. Measuring anywhere on the sprung mass

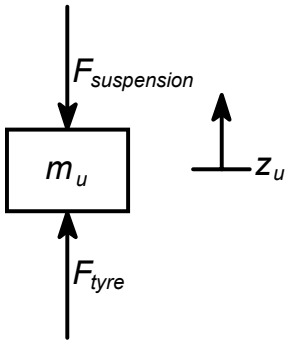

Figure 2.5 Dynamic equilibrium of an independent front unsprung mass of the truck.

therefore requires inversion of a non-linear system in order to accurately calculate road inputs from measured response. An alternative approach is to reconstruct the road profile through optimisation. This entails that the road profile is identified by iteratively changing road elevation provided to a simulation model until the measured response is matched. The measurement configuration of figure 2.5 however, treats the suspension strut force as a known variable. Consequently, this force is not modelled as a non-linear function of relative suspension strut displacement and velocity. Neither is the inversion of a non-linear system required.

Tyre/wheel non-uniformities are the only excitations that cannot be distinguished from the tyre force F_{tyre} through this measurement configuration. All other significant forces that act on the unsprung mass, such as those caused by pitch and roll motion of the sprung mass, are transferred through the suspension. These can therefore be measured separately from the tyre force. Characterisation of the complete vehicle is also not necessary.

The success of this measurement configuration is subject to the accuracy with which forces between the sprung and unsprung masses can be measured. Chapter 3 explains how suspension strut forces are measured.

Once tyre force is available, the unsprung mass displacement and some sort of inverse tyre model are required to calculate the road input that corresponds to the tyre force. Alternatively, the road profile can be reconstructed through optimisation. Newton's second law is applied to the independent front unsprung mass in a way similar to the schematic presentation of figure 2.5. Road inputs are provided to such a simulation model, while $F_{suspension}$ is treated as a known variable. The road profile can be determined by iteratively changing the road input until simulated unsprung mass acceleration matches measured unsprung mass acceleration. Tyre models with different levels of complexity can be used in such a model with the advantage that inversion is not required.

2.5 Dynamic tyre force measurement methods in the literature

Cebon (1999) discusses a few vehicle-based methods to calculate vertical dynamic tyre forces. These methods are explained in this section under the headings: strain-gauged axles, tyre pressure measurements and instrumented hubs.

Strain-gauged axles

The axle housing is strain gauged between the spring mounting and the wheels to measure either bending moments or shear forces. Accelerometers are used to measure vertical acceleration of the axle (figure 2.6a). For the case where shear strain is measured, a pair of strain gauges is mounted on both the front and rear faces of the axle at an angle of 45° to the vertical (figure 2.6b). Measured strain due to axle shear is converted to shear forces S_{R1} and S_{R2}. For the case where bending moment is measured, two strain gauges are mounted on the upper and lower surfaces of the axle (figure 2.6b). These measure bending strain that can be converted to bending moments M_{R1} and M_{R2}.

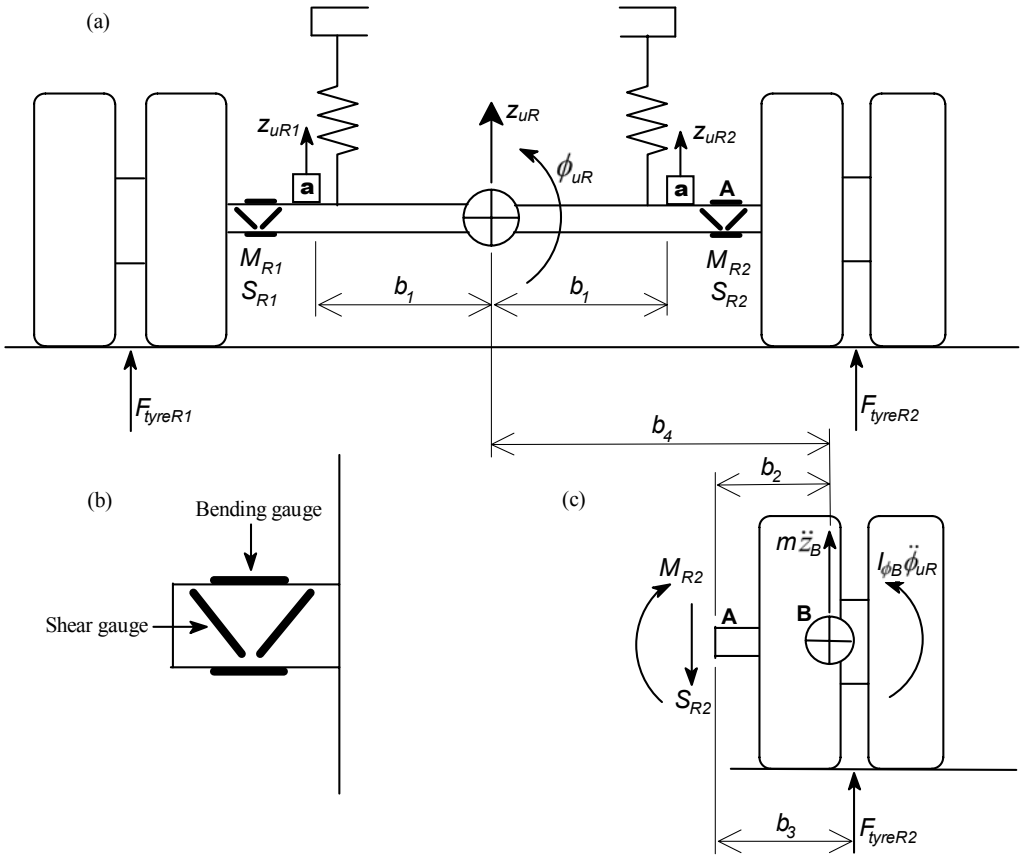

Figure 2.6 Dynamic tyre force measurement configuration using strain-gauged axles. (a) Roll-plane elevation of rear axle. (b) Expanded view of the strain gauges on the axle. (c) Free body diagram of components outboard of point B (adapted from Cebon, 1999).

Accelerations are required to correct the measured bending moments or shear forces for the inertial kinetics of the wheel components outboard of the strain gauges. The vertical acceleration of the centre of gravity of the axle $\ddot{z}_{uR}$ and the roll acceleration $\ddot{\phi}_{uR}$ can be determined from the measured accelerations according to

$$\ddot{z}_{uR} = \frac{\ddot{z}_{uR1} + \ddot{z}_{uR2}}{2} \tag{2.13}$$

$$\ddot{\phi}_{uR} = \frac{\ddot{z}_{uR2} - \ddot{z}_{uR1}}{2b_1} \tag{2.14}$$

Assuming a small roll angle ϕ_{uR}, the vertical acceleration of point B (the centre of gravity of components outboard of A) is given by

$$\ddot{z}_B = \ddot{z}_{uR} + b_4\ddot{\phi}_{uR}$$

Using equations 2.13 and 2.14

$$\ddot{z}_B = \frac{1}{2}[\ddot{z}_{uR2}(1+\frac{b_4}{b_1}) + \ddot{z}_{uR1}(1-\frac{b_4}{b_1})] \tag{2.15}$$

Applying Newton's second law to the outboard components (figure 2.6c), the vertical tyre force F_{tyreR2} is calculated as

$$F_{tyreR2} = S_{R2} + m\ddot{z}_B \tag{2.16}$$

if shear force S_{R2} is measured and

$$F_{tyreR2} = \frac{1}{b_3}[M_{R2} + I_{\phi B}\ddot{\phi}_{uR} + m\ddot{z}_B b_2] \tag{2.17}$$

if bending moment M_{R2} is measured. Similar equations apply for S_{R1} and M_{R1}. m is the mass of components outboard of point A and $I_{\phi B}$ is the roll mass moment of inertia of the outboard components about point B.

Cebon (1999) mentions that the main advantages of measuring moments M_{R1} and M_{R2} instead of the shear forces S_{R1} and S_{R2} is that the bending strains are larger than the shear strains and therefore the measurements are less prone to noise. The main

disadvantage of measuring moments is that roll or sideslip motion can cause errors due to side forces or variation of the moment arm b_3. Also, the outboard mass m can be obtained relatively easily, but not the roll mass moment of inertia $I_{\phi B}$. For these reasons the shear force method is recommended.

Tyre Pressure Measurements

Cebon (1999) mentions that attempts to measure dynamic forces by monitoring tyre pressure variations have not been successful due to the non-linear, frequency-dependent relationship between tyre force and pressure change.

Several systems based on the measurement of tyre deflections have been developed. Cebon (1999) lists them as

- Measurement of vertical tyre deflections using an optical sensor mounted on the axle, or a potentiometer measuring displacement between the wheel rim of a tubeless tyre and the inner liner of the tyre.
- Measurement of the lateral deflections of the side wall of the tyre by a mechanical or electrical pick-up.

He comments that these methods give erroneous results when the tyre is rolling with side-slip.

Instrumented Hubs

In this method, transducers are mounted between the wheel rim and hub. Two orthogonal force components, whose axes rotate with the wheel, are measured. Vector addition of the components yields the resultant force in the wheel plane. Cebon (1999) also mentions that a number of technical difficulties with calibration and data processing exist.

The analogy between equation 2.12 and the method of strain-gauged axles is clear. Both are based on dynamic equilibrium of the unsprung mass. The only difference is the way in which forces between the unsprung and sprung masses are measured. The strain-gauged axles method can also be applied to an independent front unsprung mass of the haul truck, in which case the front spindle will be instrumented instead of an axle. This option is still open. In the current work however, the advantage of working with a hydro-pneumatic suspension strut is utilised.

2.6 Tyre enveloping

A pneumatic tyre engulfs short wavelength irregularities in the road and thereby decreases the force transferred to the wheel spindle. The larger a tyre, the less responsive it is to high frequency excitation, i.e. it acts as a low pass filter.

Defects such as ditches and humps are represented in a wide frequency band. It is therefore expected that some high frequency content will be attenuated. The most important content contributing to the shape of a defect however appears at low frequencies. Therefore, the tyre should respond to the rough shape of a defect and this response will be measured. It is expected that large defects will be identified more accurately than small defects.

2.7 Tyre and wheel non-uniformities

Section 2.4 mentions that with the measurement configuration of figure 2.5 it is not possible to distinguish between tyre/wheel non-uniformity excitations and road inputs. Cebon (1999) states that the forces caused by tyre non-uniformities are usually only significant on relatively smooth roads, when they can be of comparable magnitude to the forces due to road excitation. It should therefore not be a concern in the current work that aims to identify large defects on gravel roads.

2.8 Wheelbase filtering

Wheelbase filtering is a geometric effect. Only bounce motion of the sprung mass occurs at a road wavelength equal to the wheelbase of the vehicle or harmonics thereof. Similarly, only sprung mass pitch motion occurs on roads with a wavelength twice the wheelbase length or harmonics thereof (Gillespie, 1985). The influence of wheelbase filtering on vehicle response is dependent on vehicle speed – just as with any other road input. For further details see Gillespie (1985 & 1992) or Cebon (1999).

Wheelbase filtering does not violate mathematical modelling. Mathematical modelling rather has the inherent ability to simulate wheelbase filtering. Thus, whether measurements are taken on the sprung or unsprung masses, any reconstruction technique based on mathematical modelling should not loose its appropriateness when wheelbase filtering is present.

2.9 Friction in the suspension strut

Sayers and Gillespie (1981) studied the effect of friction in non-linear leaf springs on truck ride. They showed that the entire vehicle effectively vibrates on its tyres when driven on smooth roads with high levels of friction in the suspension. The hydro-pneumatic suspension struts on the haul truck studied in the current research show similar effects. Friction appears between the upper bearing and the barrel, and the lower bearing and the suspension rod.

The first and most obvious indication of static friction in the suspension struts of an operational vehicle is zero relative suspension strut velocity. (Relative motion refers to the motion between the barrel and rod of the suspension strut. This term is frequently used in this dissertation, although sometimes simply referred to as suspension strut motion).

Zero relative velocity alone is not a sufficient indication of static friction in a suspension strut however, since strut velocity can also be zero when the unsprung and sprung masses do not move vertically at all. When it is found that there is indeed unsprung and sprung mass motion and the two motions have the same amplitude and are in phase, static friction is present. Under excitation without static friction in the suspensions struts, unsprung and sprung mass motions will be dissimilar in magnitude and out of phase, except when the excitation frequency approaches zero. This is verified by transfer function magnitude and phase plots.

Figures 2.7a shows a clip of measured unsprung and sprung mass accelerations that were recorded when the haul truck drove over a fairly smooth section of road, encountered a defect and then again drove over a smooth section of road. It is evident that the unsprung and sprung mass motions were of equal magnitude and in phase on the smooth sections. Consequently, the suspension strut had no relative movement and was in a state of static friction. Figure 2.7b verifies that the suspension strut velocity was indeed zero on these smooth sections. When the defect was encountered, motions were no longer of the same magnitude nor in phase, as is seen in figure 2.7a.

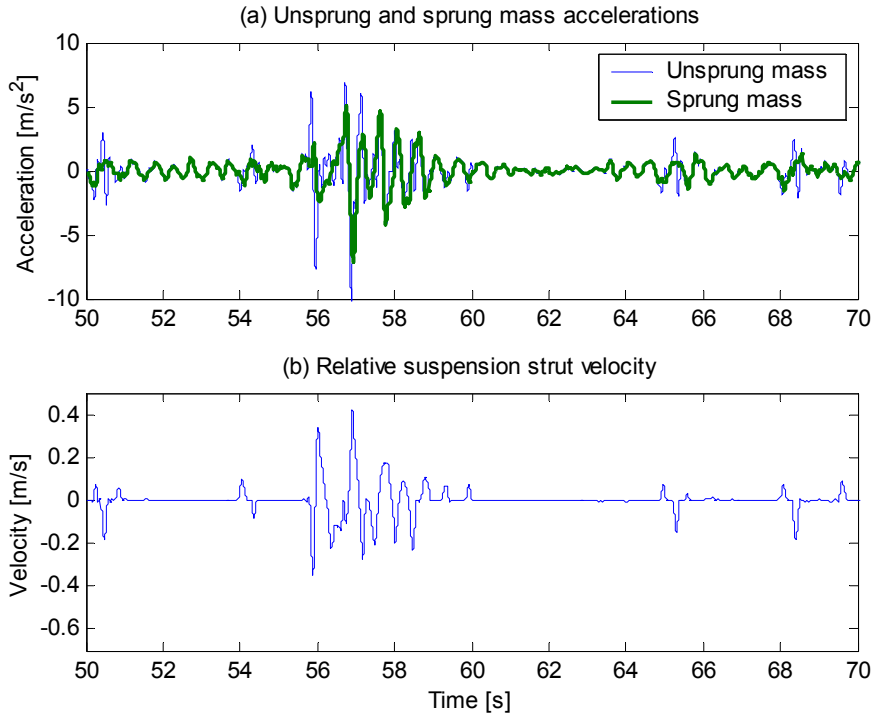

Figure 2.7 The effects of friction in the front suspension struts of the haul truck.

In chapter 3, a front suspension strut is characterised in terms of its stiffness and damping properties. It is shown that the dynamic friction force that is present when the suspension strut is in relative motion can be modelled conveniently as part of the damping force. However, the magnitude of the static friction force that is present when there is no relative motion in the strut is not known, and can therefore not be characterised in terms of suspension motion.

It is consequently possible to model the total dynamic force in the suspension strut with sufficient accuracy when a dynamic friction force is present, which is typical of the case when large defects are encountered. When defects are so small or roughness levels so low that the total dynamic force in the suspension strut consists only of a static friction force, it is not possible to calculate the force between the sprung and unsprung masses accurately. Thus, with the measurement configuration adopted, very small defects or low roughness levels are not identifiable.

Chapter 3

Response measurements and characterisation

This chapter is devoted to the acquisition of data through measurement and characterisation. Four distinct but related activities are discussed. The first is titled Preliminary Dynamic Response Measurements (PDRM). This set of measurements was executed on an operational vehicle. It is called preliminary because its purpose was to get acquainted with the vehicle. The second set of measurements on an operational vehicle had specific requirements and is therefore called Refined Dynamic Response Measurements (RDRM). The other two activities are tyre and suspension strut characterisation. The vertical stiffness of the tyres on the haul truck was determined. The hydro-pneumatic suspension strut was characterised in terms of its damping and stiffness properties.

3.1 The haul truck

Truck 47 in the fleet of the South African coalmine Grootegeluk was used during PDRM, RDRM and the tyre characterisation. This is a Komatsu 730E Haulpack. The front suspension strut that was characterised in a laboratory setup is identical to those mounted on this vehicle.

The truck is powered at the rear wheels by two electric motors that are located in a hollow cylindrical housing. In this dissertation, this housing will simply be referred to as the rear axle. Two hydro-pneumatic struts suspend the sprung mass of the vehicle at the rear. Part of the rear suspension is a trailing arm that pivots on the sprung mass. At the front, the left and right unsprung masses are independent, with the sprung mass suspended through two independent hydro-pneumatic suspension struts. These struts are rigidly fastened to the sprung mass and therefore do not allow wheel camber with respect to the sprung mass. Figure 3.1 shows a photograph of the complete haul truck. Figures 3.2 to 3.4 show sections of the truck and point out the front and rear suspension struts, the hollow rear axle and the trailing arm. The truck shown in these figures is not the one that was used during measurements.

Figure 3.1 The haul truck.

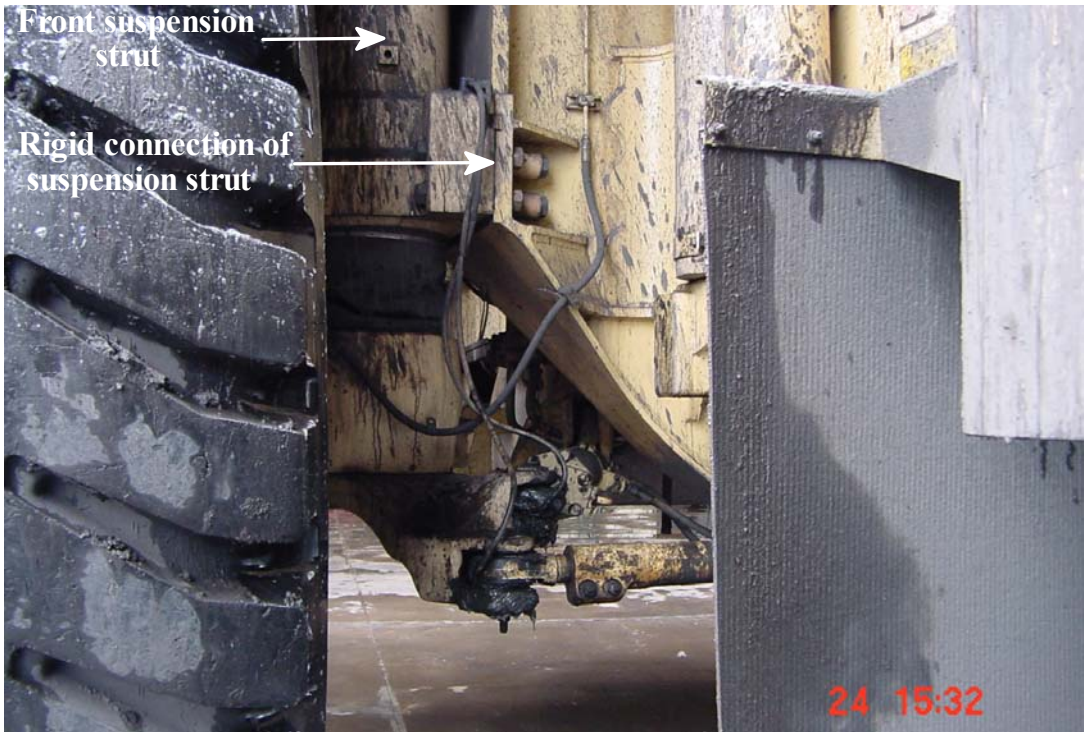

Figure 3.2 The left front wheel and suspension strut.

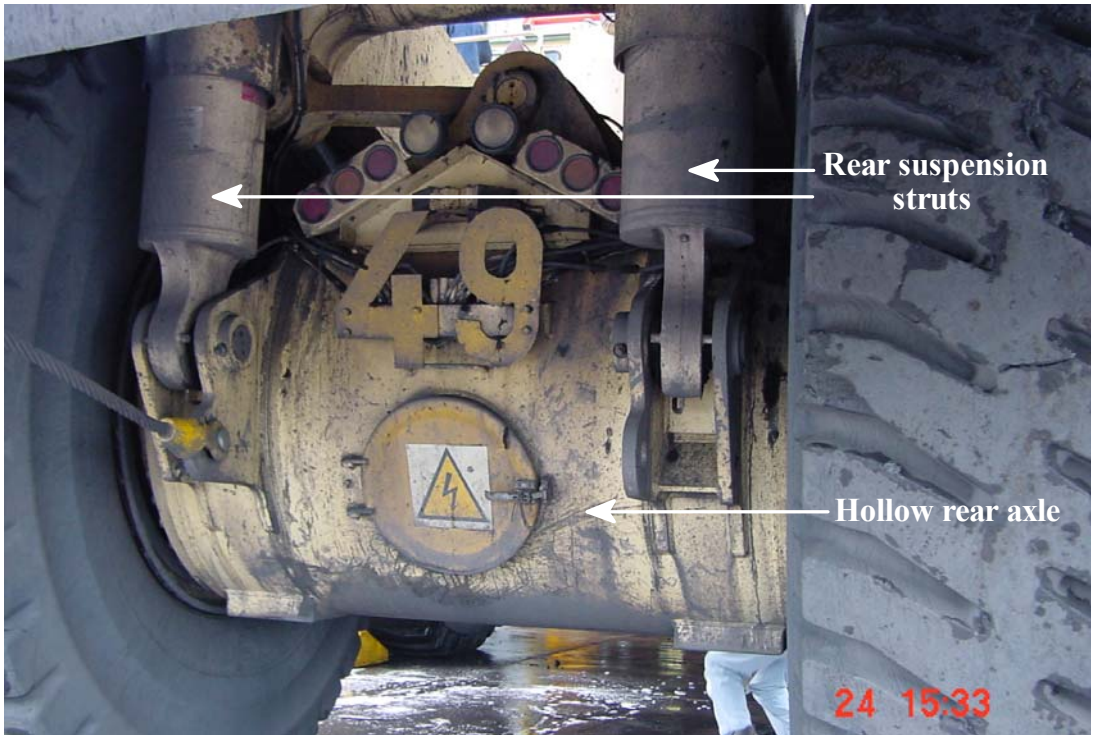

Figure 3.3 The rear axle and suspension struts.

Figure 3.4 The trailing arm.

3.2 Preliminary dynamic response measurements (PDRM)

The primary purpose of this preliminary test was to get acquainted with the haul truck under consideration, the environment in which it operated and the circumstances in which measurements would have to be taken. The vehicle was instrumented in a way that seemed best to capture the essential dynamics during operation. Measured quantities included suspension strut pressures, vertical, longitudinal and lateral accelerations of the unsprung and sprung masses at the four corners of the vehicle; and sprung mass rotational velocities.

The suspension struts were equipped with standard installed pressure transducers. Voltage output signals from these transducers were therefore tapped from the control board of the truck. Translational accelerations were measured with low-frequency capacitive-beam accelerometers that had a range of 0 to 100 Hz, while gyroscopes measured rotational velocities.

A data acquisition system with 24 channels was used. This system operated on 240V AC power that was inverted from the battery power of the truck. The acquisition system was managed by a laptop that eventually had to operate on its internal battery since it did not function properly on inverted 240V AC power. The sensors also received power from the batteries of the truck that was first inverted to 240V AC and then to approximately 12 V DC power.

Apart from severe power supply problems, a very limited period of data could be recorded continuously; both these problems received attention afterwards. In addition to the identification of some problems, these measurements gave initial insight into the response of the vehicle. For example, it was possible to determine typical acceleration peak values.

The confidence gained with the haul truck and related aspects such as the conditions in which the vehicle had to be instrumented were of great value. The measuring environment is very different and in most aspects more harsh than in a typical laboratory. Experience gained from these measurements contributed significantly to the success of those that were to follow.

3.3 Refined dynamic response measurements (RDRM)

Two approaches to the problem of large defect identification were initially considered. The one option was to model the vehicle mathematically, which was the approach eventually selected. The alternative option was to treat the truck as an undefined system

and use artificial intelligence techniques to find relationships between certain response characteristics and defect type and size.

Artificial intelligence does not aim to describe the vehicle in any theoretically based manner. The notion of using artificial intelligence in the form of neural networks would comprise the training and use of a network in an environment with numerous influencing factors. Basic modelling of vehicles on the other hand is well established. This approach allows system versatility in the sense that it is possible to computationally correct for varying loads, speeds, and other parameters that change continuously.

With PDRM, the idea was to capture as much relevant information as possible. At that stage it was not yet completely certain what approach would be followed. Prior to RDRM, it was finally decided to adopt a mathematical modelling approach. Following the methodology of section 2.4, the focus during RDRM was on the front of the vehicle. The goal was to capture a representative set of data pertaining to the problem under consideration, without distracting the focus. It would have been detrimental if measurements were limited to absolutely essential quantities; chapter 4 explains how related measurands were eventually used. Distracting the focus on the other hand would mean to invest so much time in characterising the full vehicle and measuring all over the vehicle that the purpose of road defect reconstruction is neglected. (To completely characterise the vehicle would require characterisation of the rear suspension struts. In a later section of this chapter where front suspension strut characterisation is discussed, it is evidently time consuming and expensive to characterise struts of this size). A balance was sought in the selection of measurands.

Figure 3.5 shows a schematic drawing of the truck with numbers that indicate measuring locations. Table 3.1 describes these locations and lists the quantities that were measured at each. Translational accelerations, suspension strut pressures and rotational accelerations were measured with the same equipment used during PDRM. Relative suspension strut displacements were measured with potentiometers.

With the truck instrumented in this configuration, measurements were taken on two sections of road with artificial built defects that included humps and ditches. The road was GPS surveyed to determine the locations of defects. During testing, the truck was also GPS instrumented to capture its position on the road. Thus, truck position was measured simultaneously with sensor data – accelerations, pressures, etc. Recording the internal system times of both the GPS and the laptop, it was then possible to relate sensor data to truck position. Since defect locations have been recorded previously, it was therefore also possible to quite accurately correlate response of the truck with input from the road in terms of vertical elevation.

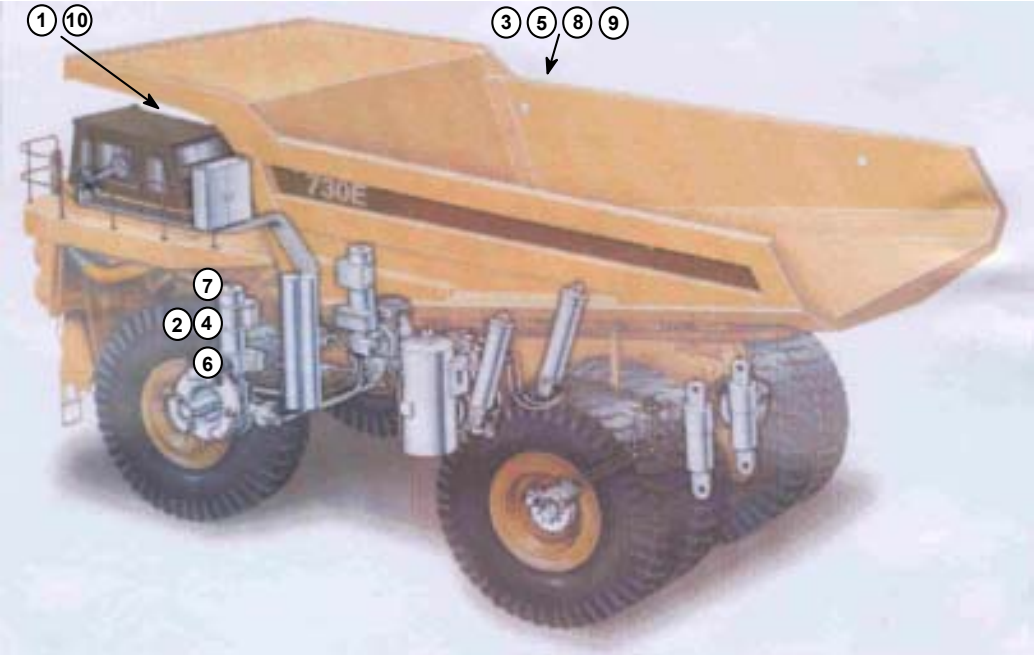

Figure 3.5 Measuring locations on the haul truck during RDRM (drawing adapted from Komatsu 730E Machine & Statex III introduction training, 2003).

Table 3.1 Quantity measured at each location in figure 3.5.

Measuring location	Description of measuring location	Quantity measured
1	Control board of the truck	Truck speed
2	Left front suspension strut	Left front suspension strut pressure
3	Right front suspension strut	Right front suspension strut pressure
4	Left front suspension strut	Left front suspension strut displacement
5	Right front suspension strut	Right front suspension strut displacement
6	Spindle of the left front wheel	Acceleration of the left front unsprung mass in the vertical, longitudinal and lateral directions
7	Top of the left front suspension strut	Acceleration of the left front of the sprung mass in the vertical, longitudinal and lateral directions
8	Spindle of the right front wheel	Acceleration of the right front unsprung mass in the vertical, longitudinal and lateral directions
9	Top of the right front suspension strut	Acceleration of the right front of the sprung mass in the vertical, longitudinal and lateral directions
10	Frame of the truck, next to the cab	Pitch, roll and yaw velocities of the sprung mass

Response data was captured at a frequency of 1200 Hz, while truck position was sampled at 1 Hz. The analyses in chapter 4 show that essential signal content appeared below 10 Hz. Thus, a sample frequency of 200 Hz would have been sufficient to capture the amplitude of data accurately. However, this conclusion is drawn from analysis of data that was captured during these measurements. Since the acquisition system was eventually capable of sampling at a higher frequency for a sufficient period of time, the sampling frequency was set to 1200 Hz, with the advantage that essential data was captured for certain. What essential data comprises would be determined by the analysis required. With such a high cut-off frequency, higher frequency motion could also be analysed, if required for whatever reason, which is obviously subject to for example the use of equipment that can measure in these frequency ranges.

3.4 Tyre characterisation

The mathematical models of chapter 2 represent the tyre as a simple linear spring. No damping is included, as is frequently done. The reason is that tyre damping is more difficult to characterise but much less important in the application of dynamic vehicle modelling than tyre stiffness.

A single linear spring is the most basic element used to model tyres in the vertical direction. One variation is the sector model that represents the tyre as a number of radial springs, equally spaced around the circumference of the tyre. The primary input property required by such models is however still the vertical stiffness of the tyre, which is determined under static loading. This section discusses how the stiffness characteristic of these huge tyres, with a diameter of 3.52 m, was determined.

Due to their size, it was not possible to characterise the haul truck tyres in any laboratory that was available. Subsequently, the spring characteristic was determined in situ. The truck was loaded with different amounts of coal, while the weight on each wheel was each time measured on an open-air weighbridge. Simultaneously, the perpendicular distance between the ground and a certain circumferential line on the wheel rim was measured. Additionally, the distance from the outer radius of an unladen tyre (not mounted on the vehicle) to the same circumferential line on the wheel rim was measured. Tyre deflections were calculated as the difference between this distance, measured on the unladen tyre and the equivalent distance, measured under each load. To have one more data point, tyre deflection under its own weight was also measured. This procedure was repeated for two different inflation pressures. Figure 3.6 shows the resulting front tyre force-deflection curves.

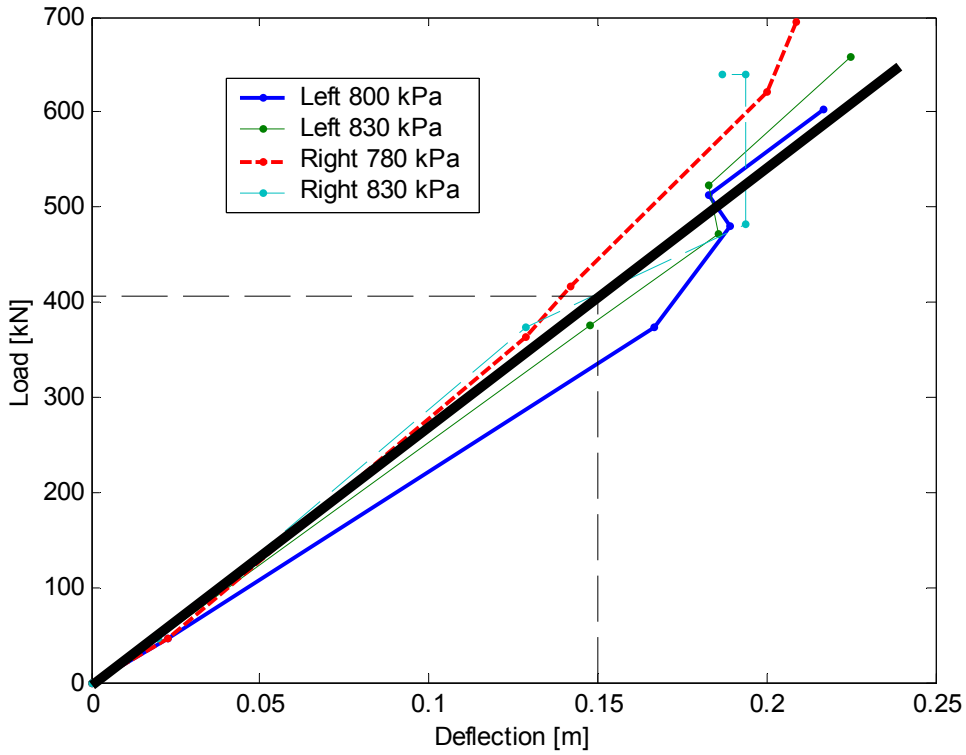

Figure 3.6 The front tyre stiffness characteristic.

Tyre stiffness depends on inflation pressure. This dependency is not clearly visible from figure 3.6. The reason is probably that measurement errors were larger than the differences in stiffness caused by the amounts of tyre pressure variation. Apart from inflation pressure, tyre stiffness is generally also influenced by tyre temperature, tyre structure, certain tyre peculiarities and vehicle speed. Differences in the structure of the tyres and other peculiarities can be responsible for the variance in the characteristics in figure 3.6, while tyre temperature is probably of secondary importance. The purpose however was not to assess the influence of each factor on tyre stiffness, but rather to identify parameters that strongly influence on the stiffness of these haul truck tyres.

Amid pressure variations and the use of tyres from different manufacturers which probably also had specific peculiarities, no large variations in stiffness are visible in figure 3.6. Data was therefore deemed adequate to calculate a vertical tyre stiffness value to serve the current modelling purposes. A reasonably linear relationship is evident in the range of measurement, which is true for most tyres up to a certain load. Hence, a constant slope line that approximates the average of measured data was added to figure 3.6. With the aid of the dashed vertical and horizontal lines, the slope was calculated as

$$\frac{405\ kN}{0.15\ m} = 2713\ kN/m$$

Henceforth, the influence of stiffness variation on modelling results could be assessed.

3.5 Suspension strut characterisation

Hydro-pneumatic suspension struts exhibit non-linear stiffness and damping characteristics. These struts are filled with oil and nitrogen gas. For those mounted on the haul truck, compression of the nitrogen is responsible for the stiffness characteristic and the resistance that the oil experiences to flow through damping ports causes a damping force. The spring and damping forces combine to form the total force (excluding friction) that is exerted by the suspension strut on the vehicle sprung mass at any point in time during motion.

Some of the data from RDRM was useful to characterise the suspension strut in terms of its stiffness characteristic. To obtain the damping characteristics through online measurements however, would have required the pressure difference over the damping ports to be known. This was not measurable without the installation of another pressure transducer, which the owner did not allow. An alternative means to obtain the suspension strut characteristics was therefore sought. Multiple options were explored and eventually the suspension was characterised in a structural test laboratory that consists of a so-called “hard wall”. This wall was ideal to mount the suspension strut in an upright position. Not many other options were as viable since, with the actuator underneath, the suspension strut eventually reached approximately 4 m into the air. Moreover, a structure capable of withstanding 600 kN of load was required. This specification was not that critical however, since the pressure inside the suspension strut could be decreased during damping characterisation tests, which would decrease the total force. Testing over the full range of operating pressures is also not that critical to determine the stiffness characteristic. Since the stiffness characteristic is created by compression of nitrogen gas, extrapolation according to the ideal gas law is accurate enough for current purposes, as will be explained in a section 3.5.2. Moreover, the stiffness characteristic could be determined from online measurements such as RDRM.

Laboratory characterisation is discussed in section 3.5.1 through analysis of measured data. Section 3.5.2 is concerned with the application of these results for the purpose of mathematical modelling. This section addresses underlying characterisation principles and assumptions. Subsequently, the validity of modelling parameters is verified in section 3.5.3 by reconstructing the total suspension strut force in the time domain. Finally, section 3.5.4 presents processed RDRM results. This section includes the stiffness characteristic that was determined from RDRM data and a short discussion on measurement for the purpose of commercial system implementation.

3.5.1 Laboratory measurements

Figure 3.7 shows the configuration in which the suspension strut was mounted against the "hard wall". The 630 kN actuator that was used in this characterisation is underneath the suspension strut. At the left side of the picture is the controller of the actuator, with test personnel attending. At the right side of the picture is a cylinder with nitrogen that was used to charge the strut.

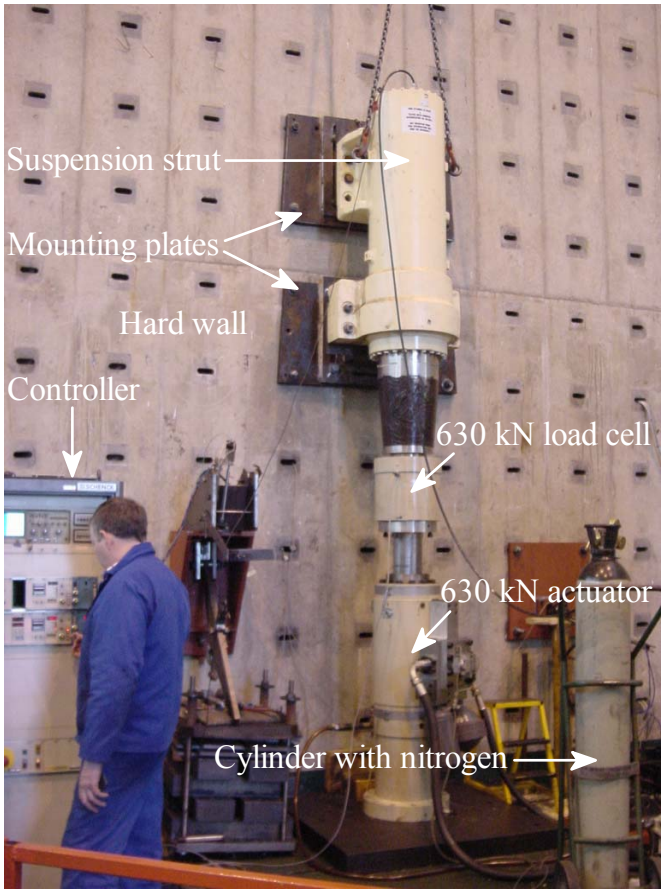

Figure 3.7 Suspension strut test setup.

Within this setup, strut pressure, strut displacement and the force exerted on the strut by the actuator were measured. A transducer with a 1/4" thread was inserted in the standard pressure duct at the top of the strut, to measure pressure. Strut displacement was measured with the linear variable displacement transducer (LVDT) of the actuator, while the 630 kN load cell measured the total force. (Although a 630 kN actuator was used, the design specifications of the wall limited forces to 400 kN). While measuring these quantities, the strut was excited at different frequencies. The data acquisition system and laptop that recorded these measurands are the same as those used during PDRM and RDRM. These are not shown in figure 3.7.

Stiffness characteristic

Figure 3.8 shows three curves that represent calculated suspension strut spring force against measured displacement for a number of excitation cycles at three different frequencies. Spring force was calculated by multiplying the measured suspension strut pressure with the effective area of the strut. A disassembled suspension strut was measured to obtain its inside area.

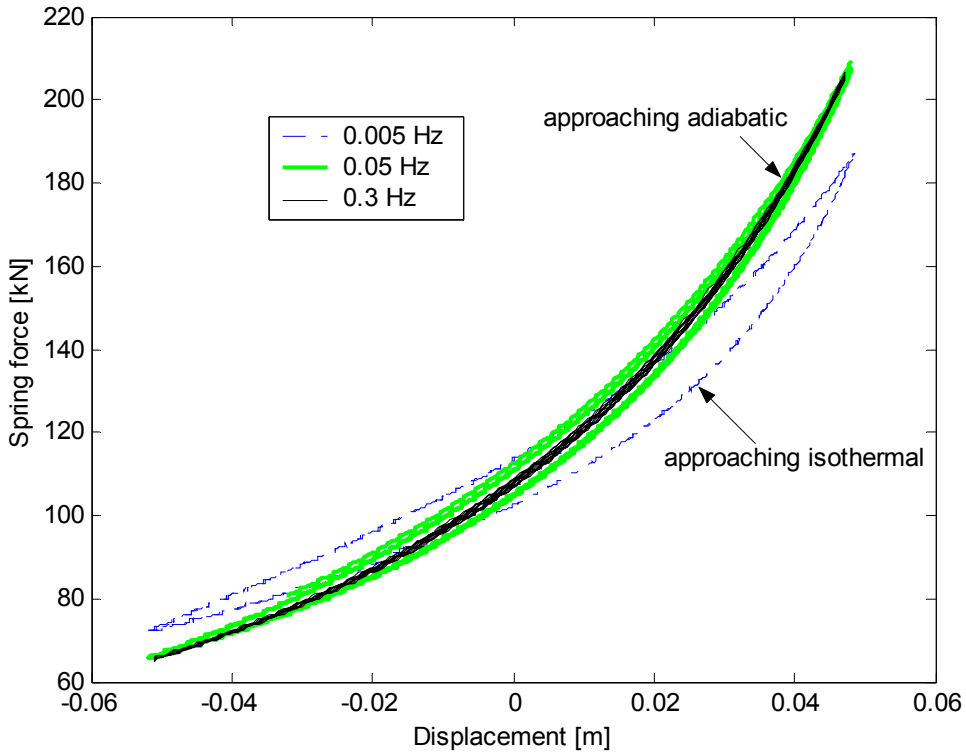

Figure 3.8 Suspension stiffness curves for a number of excitation cycles at three different frequencies.

An isothermal process refers to a process in which temperature equilibrium is maintained. An adiabatic process is one where the temperature can change but no heat is transferred to the environment. The curve labelled *approaching isothermal* in figure 3.8 is the result of excitation at a very low frequency of 0.005 Hz. The purpose of exciting at such a low frequency was to approach a constant temperature process. The hysteretic nature of the graph indicates that energy was not dissipated to the surroundings fast enough to maintain temperature equilibrium. The other curves, labelled *approaching adiabatic* are the results of excitation at much higher frequencies of 0.05 and 0.3 Hz. Excitation at 0.3 Hz is so fast that little flow of heat (or energy transfer) to the surroundings takes place. It was found that excitation above 0.05 Hz resembles this curve quite well, as is evident in figure 3.8. Els (1993) showed that completely isothermal and adiabatic compression

processes exhibit no hysteresis at all. These respectively correspond to excitation at very low and very high frequencies.

Compression is positive and extension negative in the figure 3.8. The approaching adiabatic curves show larger forces in compression and smaller forces in extension than the approaching isothermal curve. The reason is the temperature change during the adiabatic process; a comparatively higher temperature during adiabatic compression causes a higher pressure and thus a larger spring force.

Damping characteristic

Suspension strut damping was characterised by exciting the strut with sawtooth displacement signals with different frequencies. At each excitation frequency, the sawtooth displacement input caused constant strut velocities during compression and extension. Velocity increased with excitation frequency. The damping force was then calculated for each excitation at a different frequency.

Figure 3.9 shows the quantities measured for a number of excitation cycles at a frequency of 0.3 Hz. Figure 3.9a shows the total suspension strut force that was measured by the load cell. The displacement input and its derivative are respectively displayed in figures 3.9b and 3.9c, while figure 3.9d depicts the nitrogen gas pressure. Gas pressure can be converted to suspension strut spring force, as explained previously.

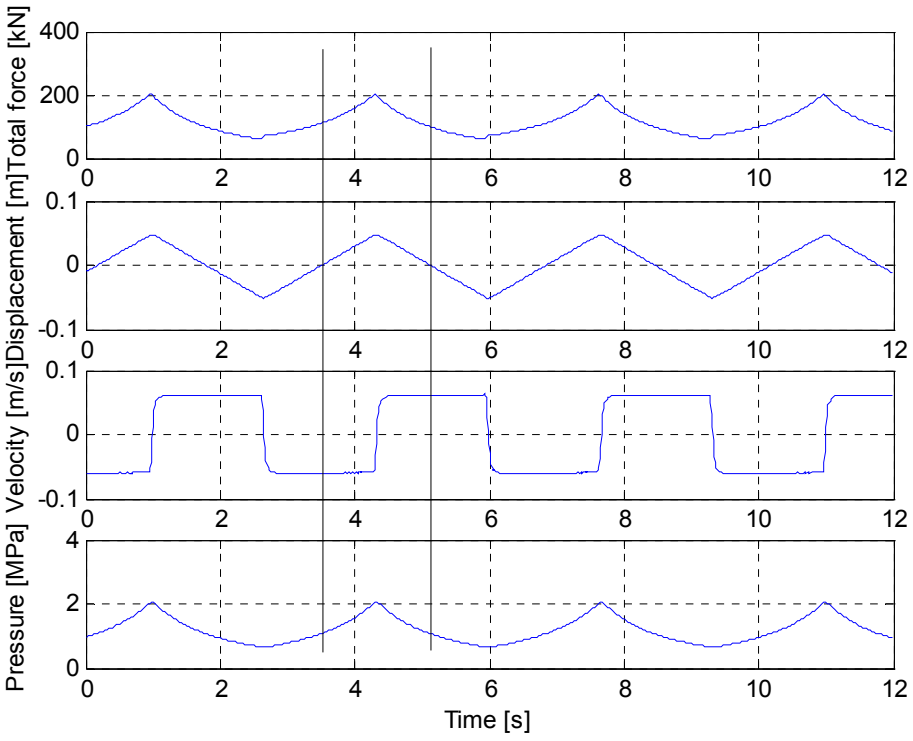

Figure 3.9 Quantities measured during suspension strut excitation at 0.3 Hz.

The damping characteristic was subsequently calculated as follows: The total force, strut velocity and strut pressure were read from figure 3.9 at a certain time instant. This instant was chosen to coincide with a zero displacement position (the static position), which corresponded with the middle of a constant velocity interval where there is least transient effects. Suspension strut pressure (figure 3.9d) was then converted to spring force and subtracted from the total force (figure 3.9a). This gave the damping force at the velocity read from figure 3.9c. The two vertical lines in figure 3.9 mark the total force, strut velocity and strut pressure at two zero displacement instants, which respectively represents compression and extension. Values were read from similar graphs for different excitation frequencies. Calculated damping forces against velocities are displayed in figure 3.10.

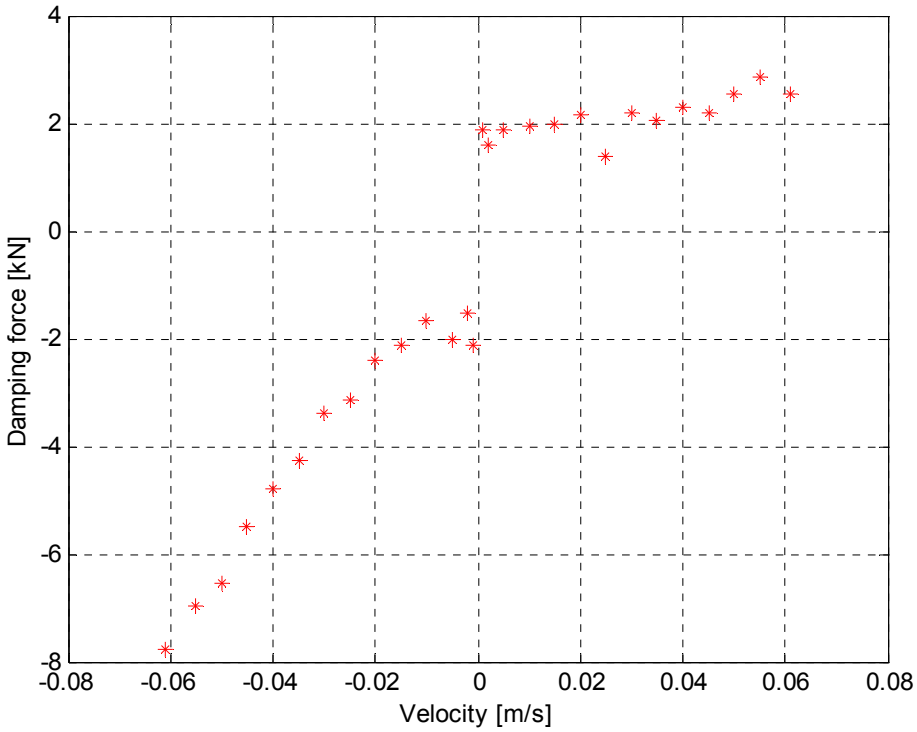

Figure 3.10 Damping force against velocity.

Since the total forces were used in these calculations, the damping forces in figure 3.10 include dynamic friction components. The last part of section 3.5.2 shows that it is convenient to model this friction force as part of the damping force.

3.5.2 Characterising for modelling

The ideal gas law

The simplicity of the ideal gas law makes it attractive to describe thermodynamic processes. For an ideal gas

$$PV = mRT \tag{3.1}$$

where P is the gas pressure, V is the gas volume, m is the gas mass, R is the nitrogen gas constant and T is the absolute gas temperature. The applicability of this law is subject to the temperature and pressure of the gas under consideration. At high temperatures and low pressures, the distances between molecules are large and intermolecular forces are small. Thus, gas density is low, in which case the law applies. The compressibility factor z can be used to compensate for deviation from the ideal gas law, while it is also an indication of the applicability of the law. The severity of errors under the ideal gas law assumption increases as z deviates further from 1.

Els (1993) determined the operating ranges of a number of hydro-pneumatic suspension struts. For the range of struts investigated, he found pressures to vary between 2 and $90\,MPa$ and temperatures to vary between -40 and $250\,°C$. Defining the range described by these limits in terms of reduced pressure and temperature and then on a compressibility chart indicates z values that deviate severely from 1. Els (1993) presented the Benedict-Webb-Rubin equation as an alternative to the ideal gas law. The hydro-pneumatic strut that was characterised in the current work however has a much smaller pressure range. RDRM data showed that pressures typically varied between 1 and $9\,MPa$ when defects were encountered. Using nitrogen's critical pressure P_c of $3.39\,MPa$, the limits of the reduced pressure P_r are then established as

$$\frac{1}{3.39} = 0.29 < P_r < \frac{9}{3.39} = 2.65$$

The absolute temperature that the nitrogen gas in the strut can attain during operation is unknown. However, the extreme values reported by Els (1993) give a good indication of the applicability of the ideal gas. For nitrogen with a critical temperature T_c of $126.2\,K$, the limits of the reduced temperature T_r at these extreme values are

$$\frac{(-40 + 273.15)}{126.2} = 1.85 < T_r < \frac{(250 + 273.15)}{126.2} = 4.15$$

The lower bound value of the reduced pressure $P_r = 0.29\,MPa$ is much lower than the critical pressure of $3.39\,MPa$. The ideal gas law is thus valid in this range, irrespective of temperature (Sonntag, et al., 1998). A generalized compressibility chart verifies this. As the reduced pressure increases, the compressibility factor z deviates from 1. From the characteristic of the generalised compressibility chart it is evident that for the

temperatures identified by Els (1993), extreme compressibility factors will appear at the maximum reduced pressure of $P_r = 2.65\,MPa$. The values are

$z = 0.927$ when $P_r = 2.65$ and $T_r = 1.85$

and

$z = 1.035$ when $P_r = 2.65$ and $T_r = 4.15$

Assuming that the temperature inside the strut can indeed reach a value of $250\,°C$, the upper limit of 1.035 is valid. The lower limit of 0.927, however will not be realised. Gas temperature is proportional to gas pressure, i.e. low temperature corresponds to low pressure and high temperature corresponds to high pressure. Thus, at the maximum reduced pressure, the gas temperature will be significantly higher than $-40\,°C$. For this reason, the lower limit compressibility factor in the region of the maximum pressure is expected to be substantially closer to 1. Consequently, the behaviour of the gas inside the strut is expected to be close to that of an ideal gas. The applicability of the ideal gas law is indeed confirmed below.

The ideal gas law for spring stiffness characterisation

The ideal gas law is applied by developing a relation between different states in which the suspension strut can operate. The ideal gas law at states 1 and 2 gives

$$P_1V_1 = m_1RT_1$$

and

$$P_2V_2 = m_2RT_2$$

The mass of the gas inside the suspension strut remains constant ($m_1 = m_2$). R is also a constant. If compression is isothermal, T_1 equals T_2 and

$$P_1V_1 = P_2V_2 \tag{3.2}$$

A polytropic process is one where PV^n remains constant (Sonntag, et al., 1998). This denotes

$$P_1V_1^{\,n} = P_2V_2^{\,n} = C \tag{3.3}$$

where n is a polytropic exponent and C is a constant that describes the relationship. For an isothermal process $n = 1$. For adiabatic expansion of nitrogen $n = 1.4$. The polytropic

relationship can be written in terms of spring force and gas height inside the suspension strut as

$$P_1 V_1^{\ n} = (F_1 A)(A x_1)^n = C \tag{3.4}$$

where A is the effective inside area of the strut and x_1 is the gas height inside the strut at state 1. At the static position

$$P_{static} V_{static}^{\ n} = (F_{static} A)(A x_{static})^n = C \tag{3.5}$$

Subsequently

$$F_1 x_1^{\ n} = F_{static} x_{static}^{\ n} = CA^{-(n+1)} \tag{3.6}$$

For the sake of modelling, it is desired to write the relationship in terms of the static position. It then follows that

$$F_1 (x_{static} - \Delta z_1)^n = F_{static} x_{static}^{\ n} = CA^{-(n+1)} \tag{3.7}$$

and

$$F_1 (x_{static} - \Delta z_1)^n = F_2 (x_{static} - \Delta z_2)^n = CA^{-(n+1)} \tag{3.8}$$

where Δz_i is the relative suspension strut displacement from the static position at state i, in which compression positive. Finally

$$F_i = CA^{-(n+1)} (x_{static} - \Delta z_i)^{-n} \tag{3.9}$$

x_{static} and C values were determined from the laboratory measured data through manipulation of equation 3.9. Subsequently, this equation was used to model the force-displacement relationship as an adiabatic process. Figure 3.11 compares the calculated force-displacement characteristic to the measured curves in figure 3.8.

Good resemblance with the curves that were measured at the higher excitations frequencies is clear. Although it is also possible to determine a relationship for isothermal excitation, RDRM data indicates that excitation during operation approaches an adiabatic process. This is verified in section 3.5.4 where an adiabatic relationship is fitted to RDRM data.

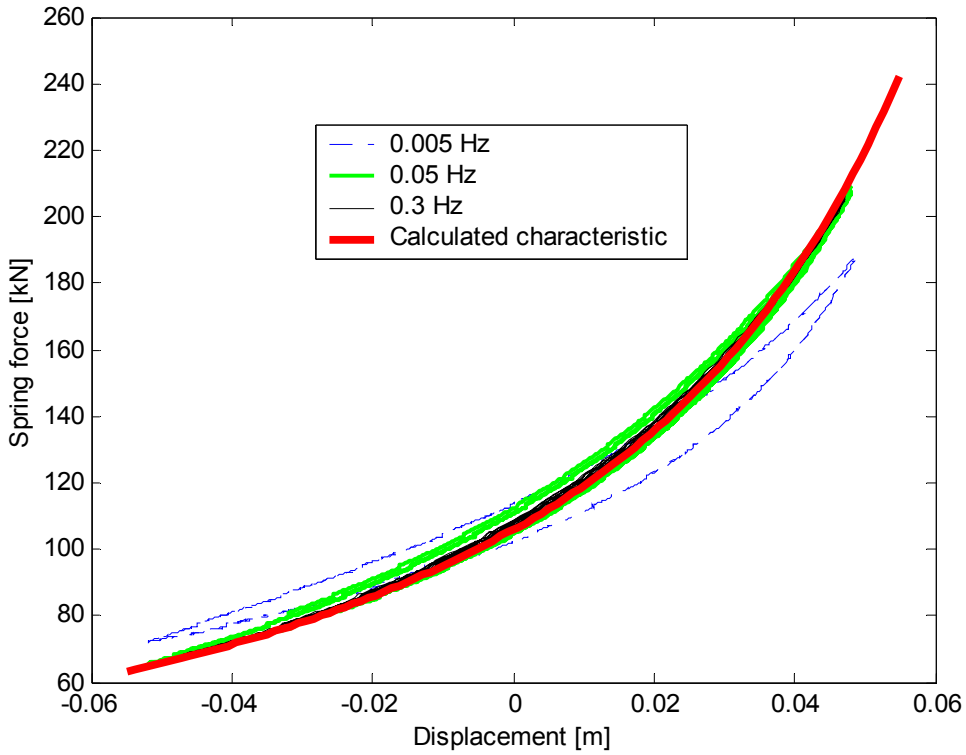

Figure 3.11 Measured and calculated suspension strut stiffness characteristics.

As mentioned previously, heat transfer effects are responsible for the hysteretic nature of measured data. Els (1993) proposes a method to model this phenomenon that is based on the use of a thermal constant. The current work neglects this hysteresis, however. Although the importance of modelling these hysteretic effects was not assessed in particular, a parameter sensitivity analysis showed that a 10% change in the stiffness constant C had a small effect on modelling results. Defect geometry identification, which is discussed in chapter 4, also proved to be insensitive to such small changes in the stiffness characteristic.

Damping characterisation

Figure 3.12 depicts the front suspension strut. Damping is caused by oil flowing through the ports in the side of the suspension rod. During compression, oil flows from space 1 to space 2. During extension, oil flows to the space 2 to space 1, in which case some of the damping ports are closed by valves. Consequently, damping is higher in extension than in compression, which makes sense from a ride perspective. Space 1 also contains the nitrogen gas that is responsible for the spring force in the strut. The nitrogen lies on top of the oil, with the oil level high enough to cover the damping ports.

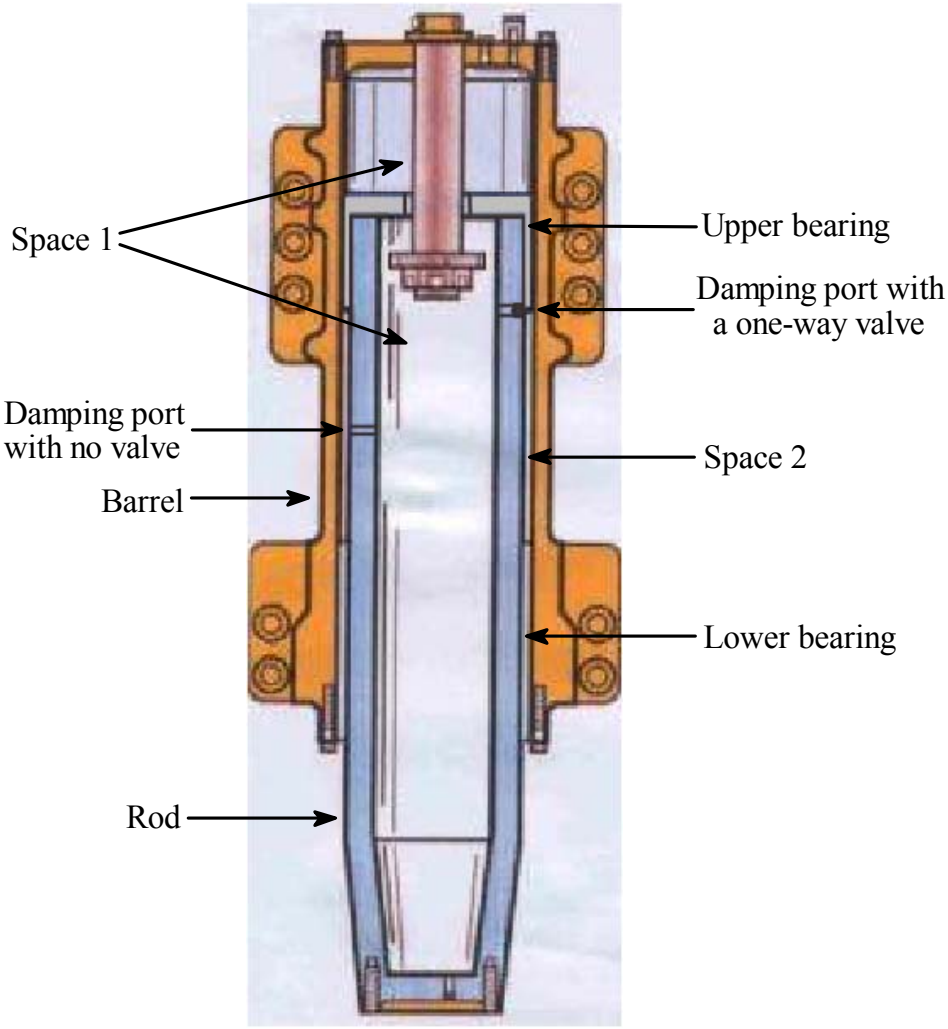

Figure 3.12 The front suspension strut (drawing adapted from Komatsu 730E Machine & Statex III introduction training, 2003).

If a measured relationship between suspension strut velocity and damping force was available over the entire operating range of the strut, it would only have been necessary to interpolate between data points to find the damping force for a given velocity. This was not possible however, since the hydraulic oil flow rate required to create strut velocities above $0.06\,m/s$ was not available to the actuator. Nonetheless, the most important information pertaining to the damping characteristic was obtained.

For many dampers it would be difficult to determine a simple relationship between suspension velocity (oil flow) and damping force. For simple geometries like the damping ports of this suspension strut however, theoretical relationships between fluid flow and pressure difference are generally well established. Assuming incompressible steady state one-dimensional frictionless flow of oil through the ports and that the velocity of bulk fluid in the strut is small compared to the velocity through the ports, the

energy equation gives pressure difference to be directly proportional to the square of fluid velocity

$$\Delta P_{port} = C_{port} V_{port}^2 \tag{3.10}$$

where ΔP_{port} is the pressure difference over the port, V_{port} is the velocity of fluid flowing through the port and C_{port} is a constant that relates pressure drop to the square of the velocity. C_{port} is comprised of theoretically known parameters, which need not be identified for the current argument. Only the relationship between pressure drop and velocity is important.

The damping ports of the strut in figure 3.12 are in parallel, which require the pressure drop over each hole to be the same under the abovementioned assumptions. The pressure difference between spaces 1 and 2 is then expected to be proportional to the square of the velocity of the fluid flowing through each damping port. The combined volume flow through all the ports should equal the volume flow in space 1, from which the velocity of the suspension rod relative to the barrel can be related to the velocity of the fluid flowing through the damping ports. This relationship can then be used to relate the pressure difference between spaces 1 and 2 to the velocity of the rod relative to the barrel. Using the effective area inside the strut over which the pressure difference is created, the damping forces exerted by the strut can finally be related to the relative velocity of the strut. Thus

$$F_{damping} = C_{damping} V_{suspension}^2 \tag{3.11}$$

where $F_{damping}$ is the damping force, $V_{suspension}$ is the suspension strut velocity and $C_{damping}$ is a constant that relates damping force to the square of the strut velocity.

The relationship in equation 3.11 was used to fit curves to the measured data in figure 3.10; results are shown in figure 3.13. Extrapolation over such a large range from a limited data set can be problematic. In the present case however, the basic underlying theory is understood and although the problem is significantly simplified through the assumptions made, good resemblance between measured and calculated data is evident in the velocity range below $0.06\ m/s$ in figure 3.13. Chapter 4 verifies the acceptability of this extrapolation for current purposes through further analysis.

The forces presented in figures 3.10 and 3.13 have an offset from the zero position, which is due to a dynamic friction force that was measured in figure 3.10 and likewise modelled in figure 3.13. For any non-zero velocity, there is a dynamic friction force between the

upper bearing and the barrel, and the lower bearing and the rod of the suspension strut. Els (1993) lists authors who found the magnitude of this friction force to be frequency- and therefore also velocity dependent. It is furthermore expected that the force will increase slightly as the pressure on the bearing seals increases. The influence of these factors is however negligible for the current application, and the dynamic friction force is therefore modelled as a constant value that can conveniently be added to the damping force during simulation.

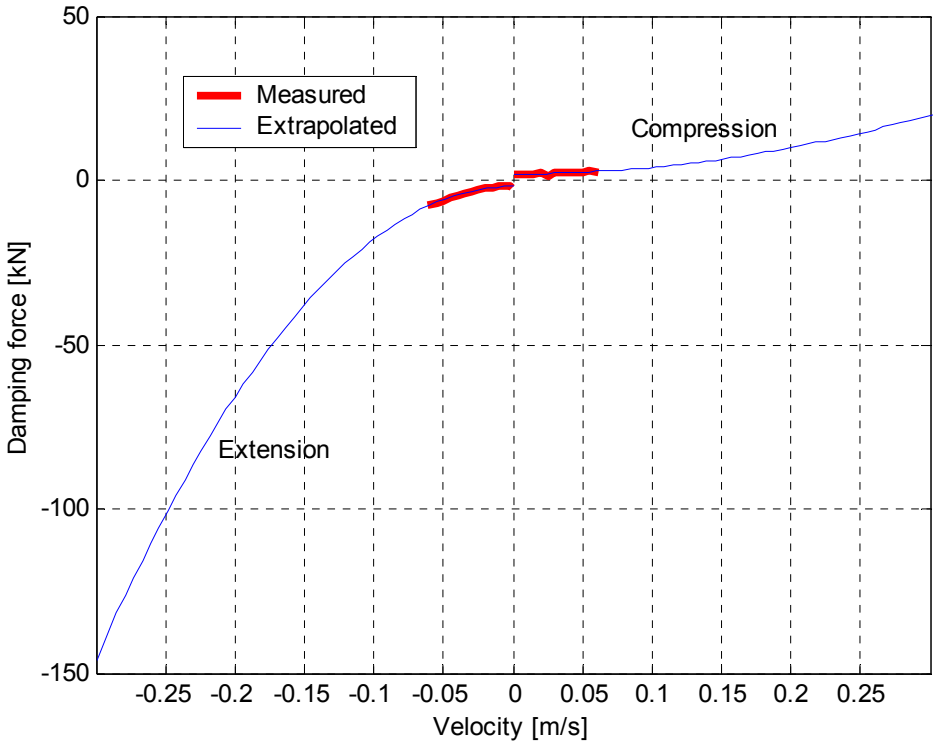

Figure 3.13 Measured and extrapolated damping characteristics.

The resulting equations that describe the calculated characteristics in figure 3.13 are: in compression

$$F_{damping} = 200 \times 10^3 \, V_{suspension}^2 + 1900 \, kN \tag{3.12}$$

and in extension

$$F_{damping} = -1600 \times 10^3 \, V_{suspension}^2 - 1900 \, kN \tag{3.13}$$

where the constant of $1900\,kN$ represents the dynamic friction force. Like figure 3.13, these equations indicate that damping in extension is higher than in compression, which

is consistent with the suspension strut design that closes some of the damping ports during extension.

3.5.3 Verification of characteristics

Figure 3.14 compares the sum of the calculated spring and damping forces to the total suspension strut force that was measured by the load cell. Measured suspension strut displacement and its time derivative were used to calculate the spring and damping forces through the characteristics that were determined in section 3.5.2. Forces are displayed against time.

It is seen that the total suspension strut force (measured by the load cell) is closely approximated. Neither the static friction force nor the inertial force due to relative suspension strut acceleration is included in the combination of calculated forces.

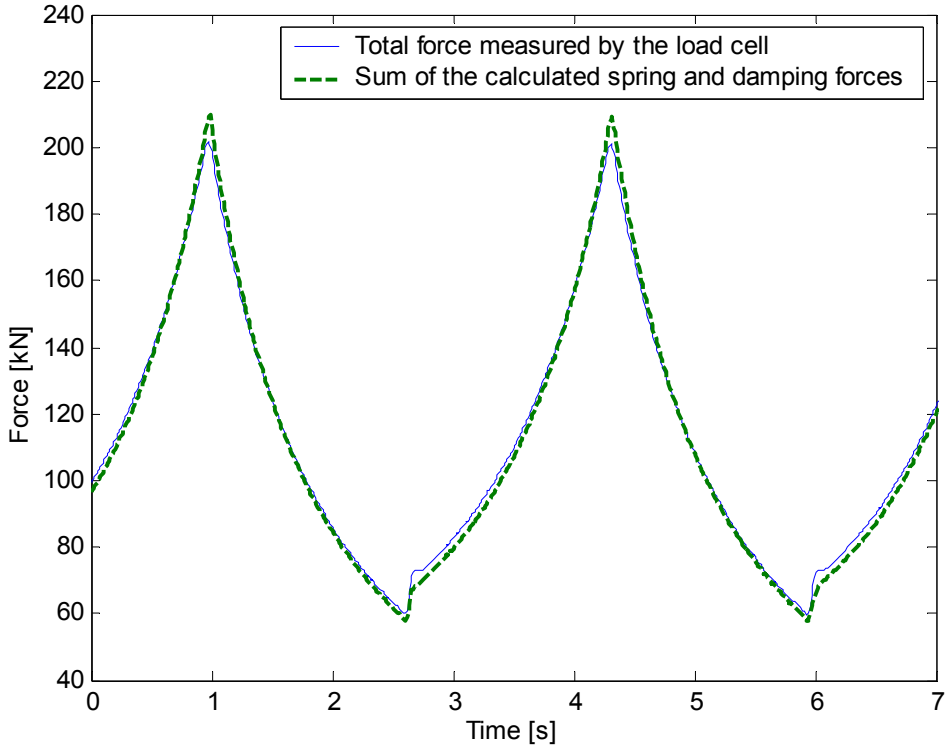

Figure 3.14 Measured and calculated suspension strut forces.

3.5.4 RDRM data and commercial system implementation

Figure 3.15 shows a force-displacement curve that represents measured RDRM data. Added to the figure is a stiffness characteristic, calculated with values of $x_{static} = 0.162$ and $C = 101$. Good resemblance is clear, which verifies that an adiabatic relationship can be used to describe the stiffness characteristic of the hydro-pneumatic suspension struts

on an operational vehicle. x_{static} and C values different from the ones that describe the curve added to the laboratory measurements in figure 3.11 had to be calculated, since the static position and pressure inside the strut differed in the two respective cases.

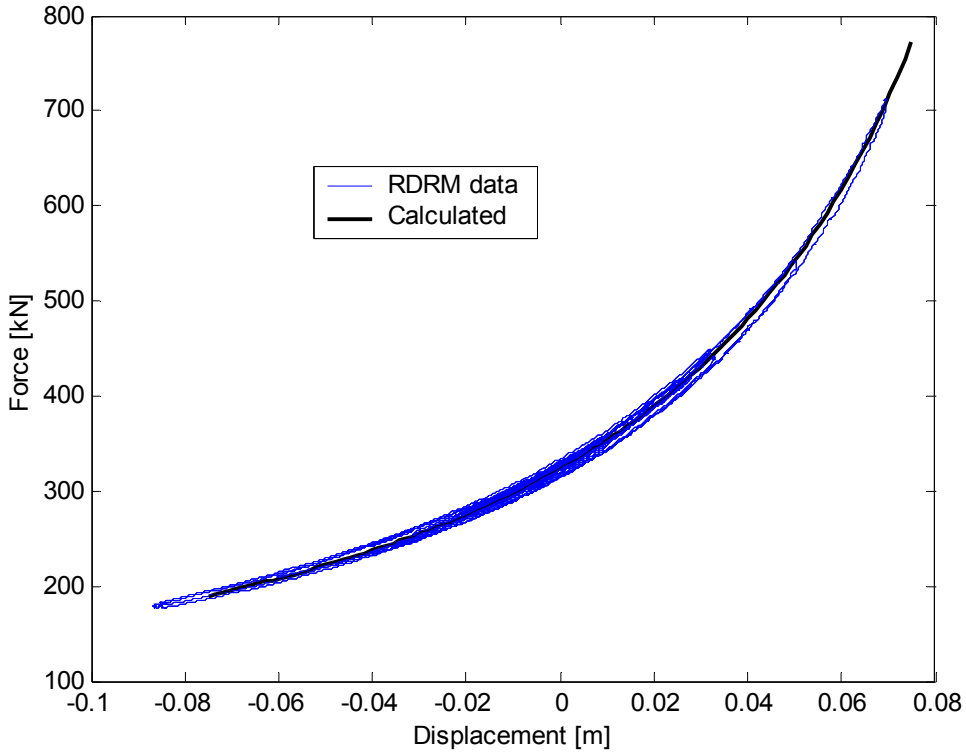

Figure 3.15 A calculated suspension strut stiffness characteristic fitted to data measured on an operational vehicle.

Suspension strut spring force can easily be calculated in a commercial system implementation. These struts are equipped with transducers that can monitor strut pressure during operation. The spring force exerted by the strut can then be calculated if its effective inside area is available.

The damping characteristic of the suspension strut can be used to calculate the damping force if its relative velocity is available. This velocity can be obtained from differentiation of the relative displacement of the strut. (Appendix D elaborates on the accuracy with which these low frequency signals can be differentiated). The relative displacement of the strut in turn can be obtained through the force-displacement characteristic and the spring force that is calculable from the strut pressure measurement. Alternatively, strut motion can be measured directly. Instead of using a potentiometer only once to obtain the stiffness characteristic, the option to install it permanently exists.

Response-type systems measure relative suspension motion or the equivalent to assess the roughness of a section of road. The calculation or measurement of suspension strut

motion in the above-explained ways can therefore be useful for similar purposes. Road roughness measurement is discussed in chapter 5.

Chapter 4

Vehicle modelling and road defect reconstruction

This chapter builds on the basis that was laid in chapter 2 by utilising the calculated characteristics and measured data of chapter 3. Most of the analyses and discussion revolves around the goal of defect reconstruction through the methodology proposed in section 2.4. Although it is theoretically possible at this stage to substitute measured data into equation 2.12 and reconstruct defects, practical implementation is more onerous. Apart from implementation issues such as those surrounding low frequency integration, adoption of this approach without thorough knowledge of influencing factors is ambiguous, and therefore does also not contribute to the body of knowledge as much as a more comprehensive investigation would do. The measurement methodology in section 2.4 was also not readily available at the outset of this project, but was discovered through research. In this process of discovering and investigation, mathematical modelling played a vital role. Subsequently, this chapter is structured in such a way that the modelling and analysis tools that formed the basis for this investigation are presented, while the path to defect reconstruction is clarified.

The first section of this chapter commences by discussing the simulation of the road test section that was used during RDRM. Hereafter, tyre models that were used in this research are discussed. Subsequently, measured signals are analysed in the frequency domain, after which quarter vehicle modelling results are compared to measured data and analysed. The bounce and pitch natural frequencies of the truck are determined and the rigid body assumption is validated. A 7DOF vehicle model proved to be useful in this research; utilising this model, it is possible to draw important conclusions. Finally, it is shown that road defects can be reconstructed with an accuracy sufficient for the purpose of haul road maintenance management.

4.1 The road

Rather than working in the coordinate system of the global positioning system (GPS), a local coordinate system was defined that aligned with the lateral-longitudinal orientation of the road. Figure 4.1 shows defect positions in the original coordinate system of the GPS, called the global coordinate system. Figure 4.2 shows defect positions in the local coordinate system. A number of coordinates were taken along the widths of the smaller defect, while coordinates were taken along the border of the large defects. Also presented

in these figures are the paths the truck followed for a few runs along the east and west sections of the road. Runs are not labelled individually. It is seen that the vehicle did not drive in a straight line with respect to the local coordinate system. Neither did the vehicle follow exactly the same path during each run.

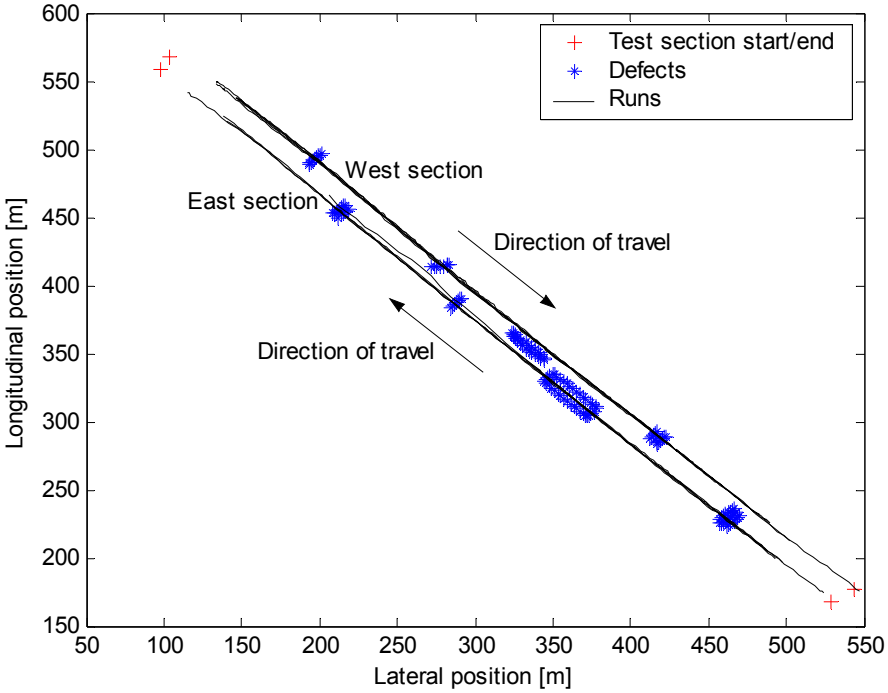

Figure 4.1 Defect and truck positions in the global coordinate system.

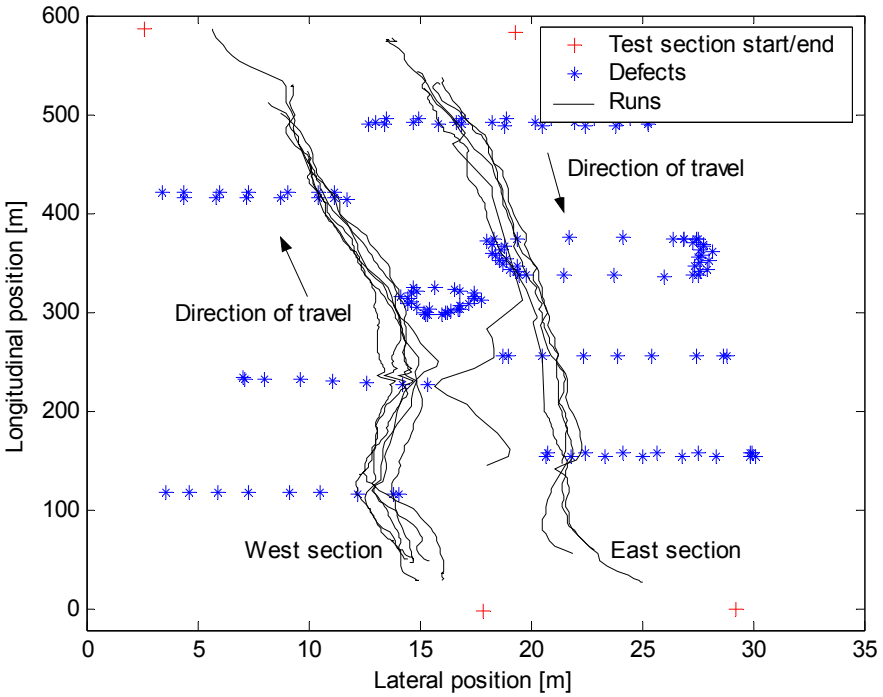

Figure 4.2 Defect and truck positions in the local coordinate system.

A two-dimensional numerical representation of the road with its defects was built by using the measured defect geometries and defect locations. Road elevation at any location along the two-dimensional road was obtained through interpolation. A three-dimensional representation of the road was also built. This allowed more accurate estimation of the road input at any location. Figures 4.3 and 4.4 show the simulated road surface in the global and local coordinate systems respectively. Also included in these figures is one channel of measured truck response. The measured quantity and its units are not important in this illustration. The purpose is only to indicate how measured response correlates with the road profile. Large response magnitudes coincide with defect locations.

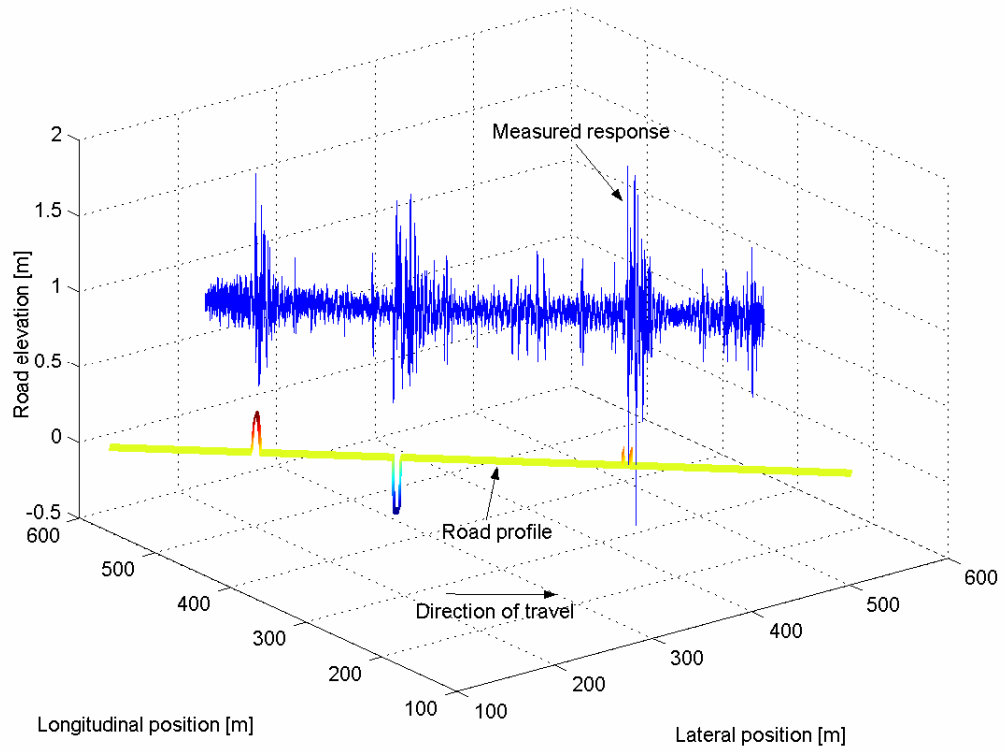

Figure 4.3 Three-dimensional west section road surface in the global coordinate system.

In the local coordinate system of figure 4.2, it seems as if some of the defect coordinate markers are cramped in. It only appears that way because of the large scale difference between the axes. Figure 4.1 verifies that they are not overlaid. For the same reason, the truck drove in a much straighter line than it appears in figure 4.2. Thus, generating a three-dimensional road surface might be considered superfluous. However, vehicle simulation proved to be sensitive to road input and therefore time was invested to generate an accurate numerical presentation of the road by utilising available information and resources to the full.

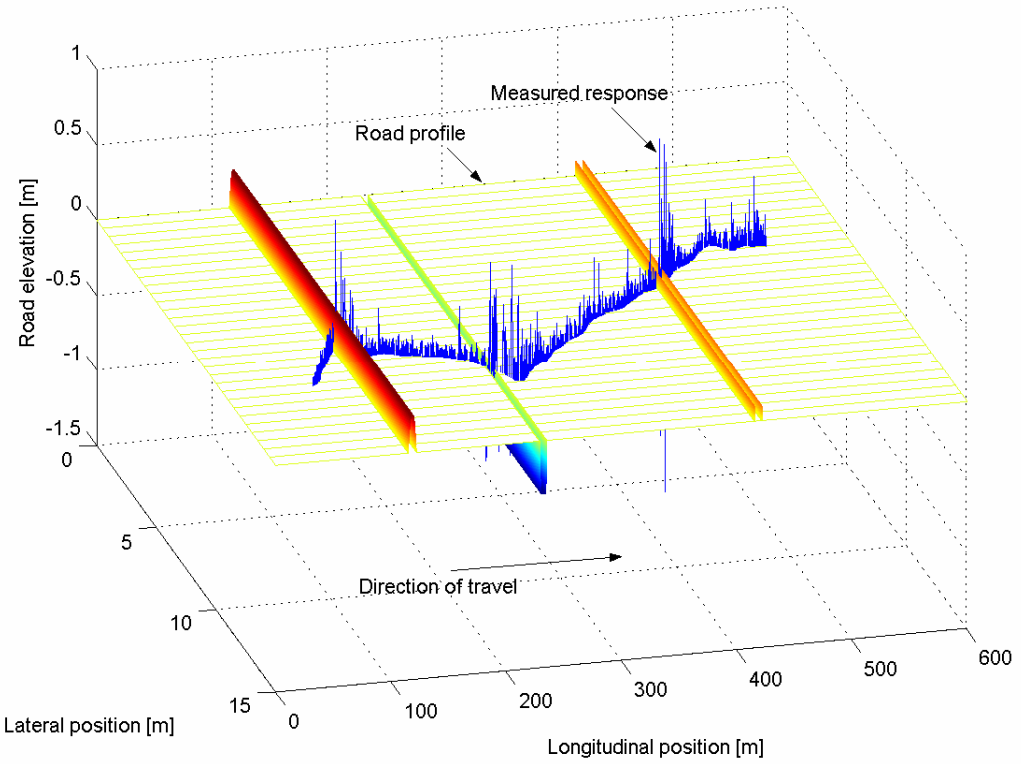

Figure 4.4 Three-dimensional west section road surface in the local coordinate system.

Slight misalignment between road inputs and response measurements was still present upon interpolation for some of the defects. Therefore, small manual adjustments were necessary. It might also have been possible to align defect geometries with response data manually from the outset. However, vehicle response is time dependent and therefore defect geometries that were described in the spatial domain would have to be transformed to the time domain by using the speed at which the vehicle passed a specific defect. Alignment will be difficult and uncertainty will remain – especially if simulation results do not resemble measured data (one more factor of uncertainty would be added to the ones that influence modelling response). This three-dimensional road formed a solid basis for finding the road input at any truck position, after which slight adjustments were reasonable. Misalignments were only fractions of a second in magnitude.

Measurement accuracy is the main factor contributing to these slight misalignments. A limited number of coordinates were used to describe defect locations. Secondly, the GPS was not located at the wheel-road interface. Corrections could be made for the separation distance between the GPS location and wheel-road interface. Still however, the GPS was located on the sprung mass and therefore motion and orientation of the truck possibly introduced small errors in position measurements. Perhaps the greatest contributor is the

sampling frequency of 1 Hz. If the truck drove at a speed of 20 km/h, a position was recorded every 5.6 m.

Figures 4.5 and 4.6 depict actual defects on the test section. Figure 4.5 show two small half-sine humps in succession. Figure 4.6 show the most severe defect on the test section. It is a ditch followed by a hump, i.e. one cycle of a sine wave.

Figure 4.5 Two half-sine humps on the test section.

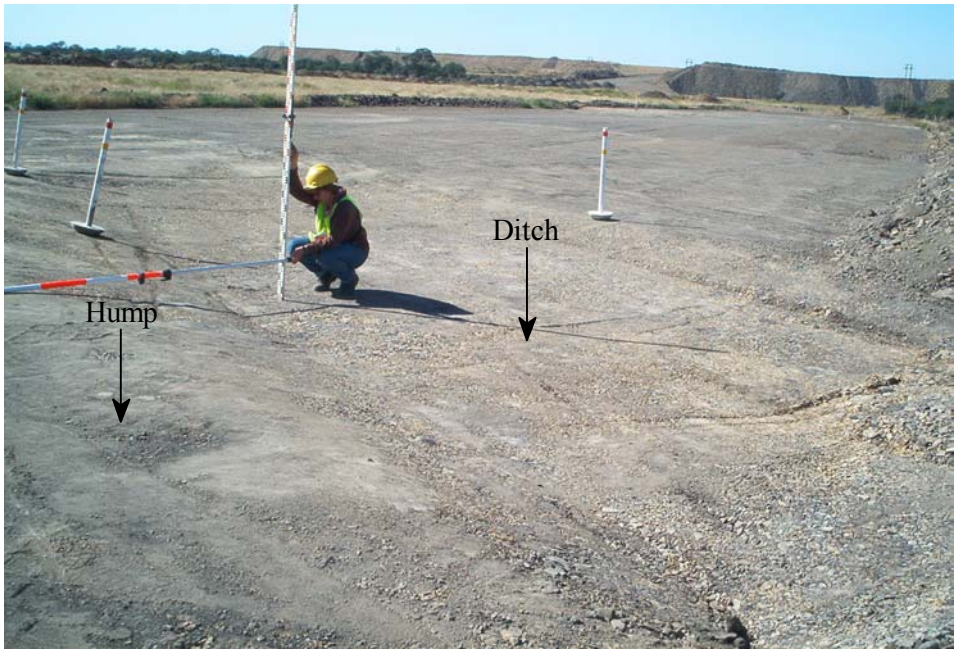

Figure 4.6 A large ditch followed directly by a large hump.

4.2 Tyre models

A point-follower model is one that responds to a single point in the road profile at a given time instant, without taking the adjacent profile of the road into account. These models therefore neglect tyre enveloping completely. To increase modelling accuracy, a tyre model that more closely resembled the truth was required.

Figure 4.7 depicts a circular rigid treadband tyre model (Park et al., 2004). The tyre is represented as a simple spring that is attached to a rigid ring that represents the treadband of the tyre. This model was implemented by filtering the road profile: The tyre was effectively lowered from a vertical elevated position until one point on the treadband made contact with the road, after which the corresponding elevation of the centre of the treadband was determined. A filtered road profile was calculated by repeating this procedure for every tyre position along the length of the road. This profile then formed the input to a vehicle simulation model that represented the tyre as a simple spring.

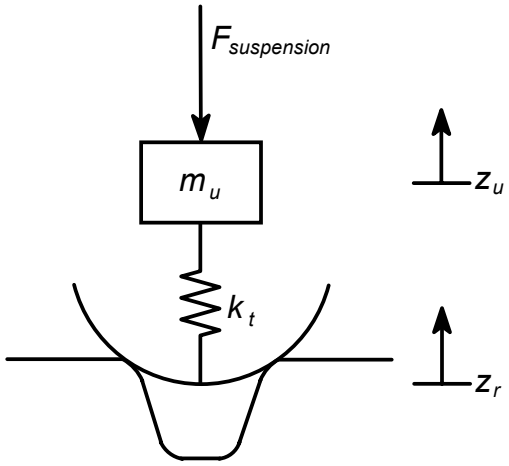

Figure 4.7 Graphical illustration of the circular rigid treadband tyre model.

Figure 4.8a demonstrates how the circular rigid treadband tyre model alters the road input for a vehicle driven over a sinusoidal section of road with a wavelength that is short compared to the size of the tyre. The centre point of the tyre treadband does not follow the exact road profile, but moves along the top of the sinusoid. Figure 4.8b shows the simulated geometry of the two half-sine humps in figure 4.5 (this geometry was obtained through interpolation on the three-dimensional surface of figure 4.4). Also shown is the treadband-filtered version of this section of road.

The circular rigid treadband tyre model was used in conjunction with the quarter vehicle and 7DOF vehicle models. It is not concluded that tyre models more sophisticated than this cannot improve results. Investigation into the use of different models is rather seen as

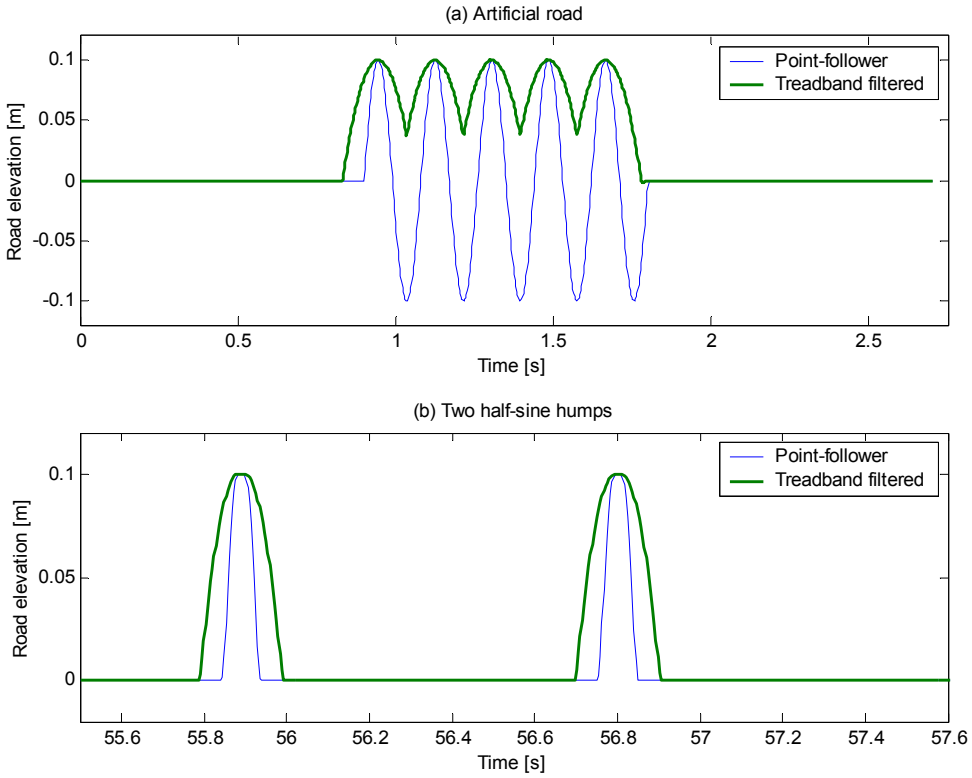

Figure 4.8 Two examples that compare circular rigid treadband-filtered road geometries to the original profiles.

an extension of this work. Several options are open to explore. Mousseau and Hulbert (1996) for example developed a two-dimensional tyre model that predicts the spindle forces produced when a tyre impacts large obstacles. NATC (2004) describes the tyre as a transfer function between the ground and wheel and thereby eliminates the need for a tyre model.

4.3 Frequency analysis of measured signals and the rigid body assumption

The quarter vehicle and 7DOF vehicle models presented in chapter 2 are all rigid body models. The measurement methodology proposed in section 2.4 is also subject to the rigid body assumption. The question is whether the rigid body assumption is valid for this haul truck and application, or whether measured truck response signals can be used under the rigid body assumption, i.e. is measured response free from structural vibrations and noise.

Acceleration measurements taken on the front unsprung masses (the wheel spindle) might contain noise due to improper mounting of the accelerometers, but it is highly unlikely that this stiff component will have any structural (flexural) modes in the low frequency range. On the contrary, the sprung mass (the frame) of trucks frequently exhibits structural vibration modes below 10 Hz (Gillespie, 1985; Ibrahim et al., 1996). Öijer (2000) mentions the importance of a flexible presentation of the frame in truck fatigue analysis.

Figures 4.9 to 4.12 respectively show measured power spectral densities of the vertical motions of the sprung and unsprung masses (respectively measured at locations 9 and 8 in figure 3.5), and pitch and roll motions of the sprung mass (measured at location 10 in figure 3.5).

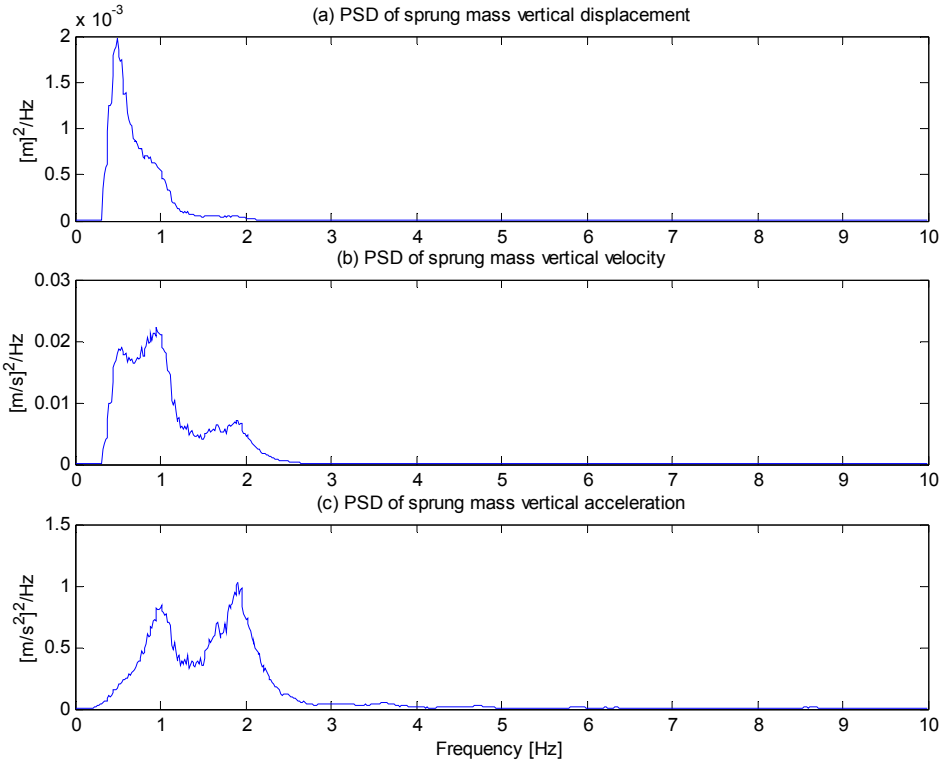

Figure 4.9 Power spectral densities of the vertical motions of the sprung mass.

The three subplots in each of figures 4.9 to 4.12 illustrate the effect of frequency amplification. For a harmonic signal, displacement and acceleration are related by the square of the excitation frequency. If displacement amplitude is kept constant and the excitation frequency is increased, acceleration amplitude increases proportional to the square of the frequency. As a consequence, small high frequency displacements correspond to high frequency accelerations of substantial magnitude. Thus, while high frequency structural displacements might be negligible under the rigid body assumption, chances are that high frequency structural accelerations are not.

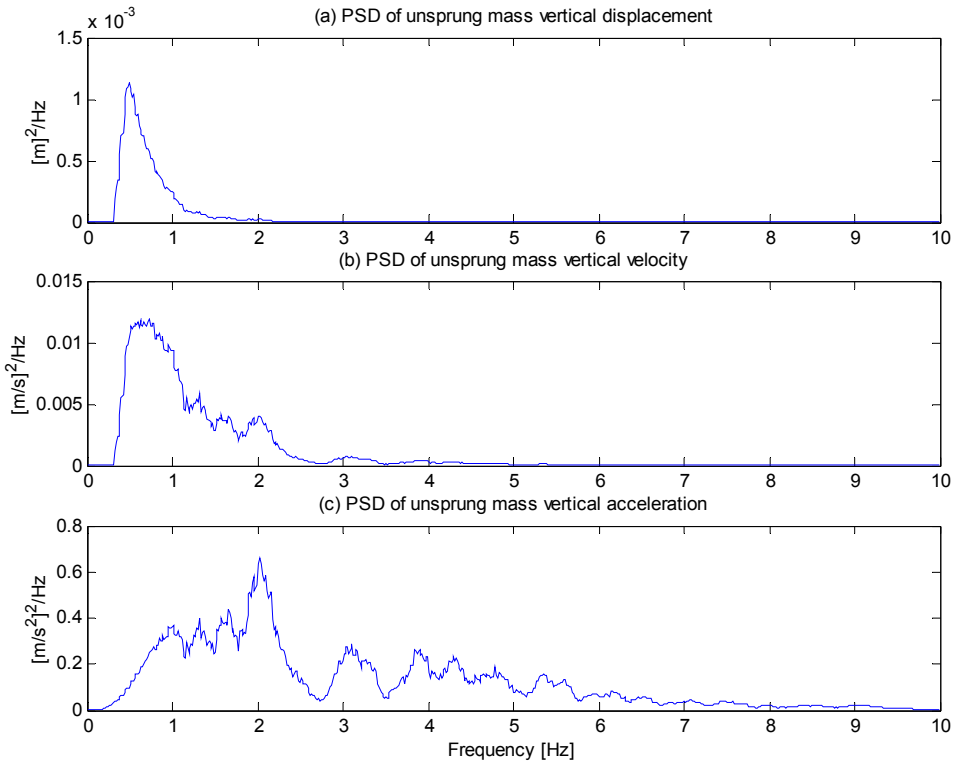

Figure 4.10 Power spectral densities of the vertical motions of the unsprung mass.

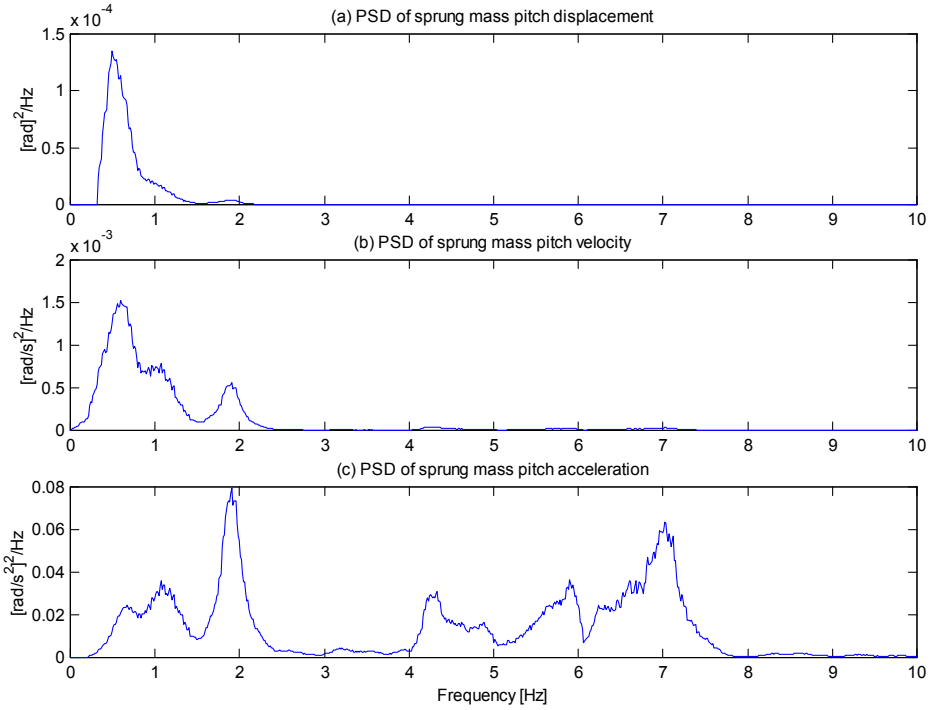

Figure 4.11 Power spectral densities of the pitch motions of the sprung mass.

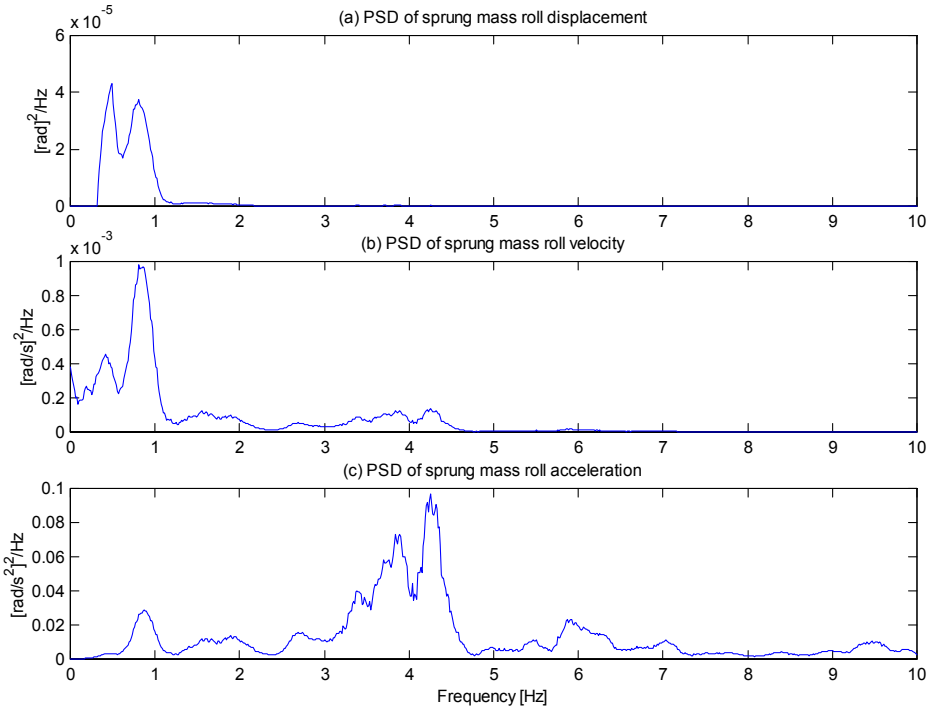

Figure 4.12 Power spectral densities of the roll motions of the sprung mass.

Figures 4.11c and 4.12c contain higher frequency content that is absent from figure 4.9c. While the vertical acceleration of the sprung mass was measured on top of the right front suspension strut, the gyroscopes that measured rotational pitch and roll velocities were mounted on the frame of the truck, near the cab. Several possible causes for the high frequency vibrations in figures 4.11c and 4.12c can be identified

- These might be due to structural motion of the vehicle frame, although they do not appear typical.
- It is possible that the gyroscopes were not mounted adequately for such high frequency measurements.

Whatever the cause may be, the acceleration signal measured on top of the suspension strut is free from such large high frequency vibrations. This indicates that the accelerometer was mounted adequately to measure acceleration below 10 Hz and that this location is favourable for measurements that are to be used under the rigid body assumption. Through further analysis, section 4.6 shows that rigid body motion indeed dominates the measured sprung and unsprung mass accelerations below 10 Hz. The next section compares measured sprung and unsprung mass acceleration signals that were 10 Hz low-pass filtered to quarter vehicle simulation results.

4.4 Quarter vehicle modelling results

Road inputs obtained as explained in section 4.2, were used in quarter vehicle simulations. Models were built in Adams and Matlab. All Adams models started from the undeformed suspension and tyre spring positions, while Matlab simulations started from the equilibrium position. Once gravitational equilibrium is attained, Adams and Matlab simulations should give the same results. This is subject to the use of the same vehicle properties, integration schemes and step sizes.

Figure 4.13 compares Adams and Matlab simulation results to measured data for the truck driven over the two half-sine humps in figure 4.5. The humps were each 100 mm high and 0.6 m wide and were long enough that both front wheels were impacted. The characteristics determined in chapter 3 were used in this simulation

- A linear spring with a stiffness value of $2.7\times10^{6}\ N/m$ represented the tyre.
- The non-linear suspension strut spring force was modelled according to equation 3.9. That is

$$F_i = CA^{-(n+1)}(x_{static} - \Delta z_i)^{-n} - M_q g \qquad (4.1)$$

  where $C = 101$, $A = \frac{\pi}{4}0.357^2 = 0.1001\ m^2$, $x_{static} = 0.162$ and $n = 1.4$. Equation 4.1 presents the suspension strut spring force equation for a Matlab simulation, which started from the equilibrium position.
- Suspension strut damping force was calculated from an interpolation table. Equations 3.12 and 3.13 were used to set up this table. Plotting force against velocity therefore produces the graph in figure 3.13.
- Measured static suspension strut pressure was used to calculate the portion of the sprung mass that rested on the right front suspension strut of the stationary vehicle. The calculated value was 32895 kg.
- The vehicle had a right front unsprung mass of 8578.32 kg.

The sprung and unsprung mass accelerations shown in figures 4.13a and b were measured at locations 9 and 8 in figure 3.5 respectively. Due to the motion of the vehicle, the orientations of the accelerometers that produced these measurements were not exactly vertical at all times. However, these slight disorientations have negligible influence and were neglected consistently in this work.

Figure 4.13 verifies correlation between Adams and Matlab results and shows reasonable correlation with measured data. These humps were small for this size of truck and consequently transient effects were moderate. (The speed of the truck was approximately

20 km/h, which is not slow considering it had a top speed of 50 km/h). Appendix E compares simulation results to measured data for driving over two larger defects. One defect was a half sine hump and the other the defect in figure 4.6. In all these simulations it is seen that the large initial accelerations are modelled accurately. The transient motion just after the defect is passed is not modelled accurately, however. This suggests that factors beyond the simulation capability of the current vehicle model were present. These are revealed in section 4.8.

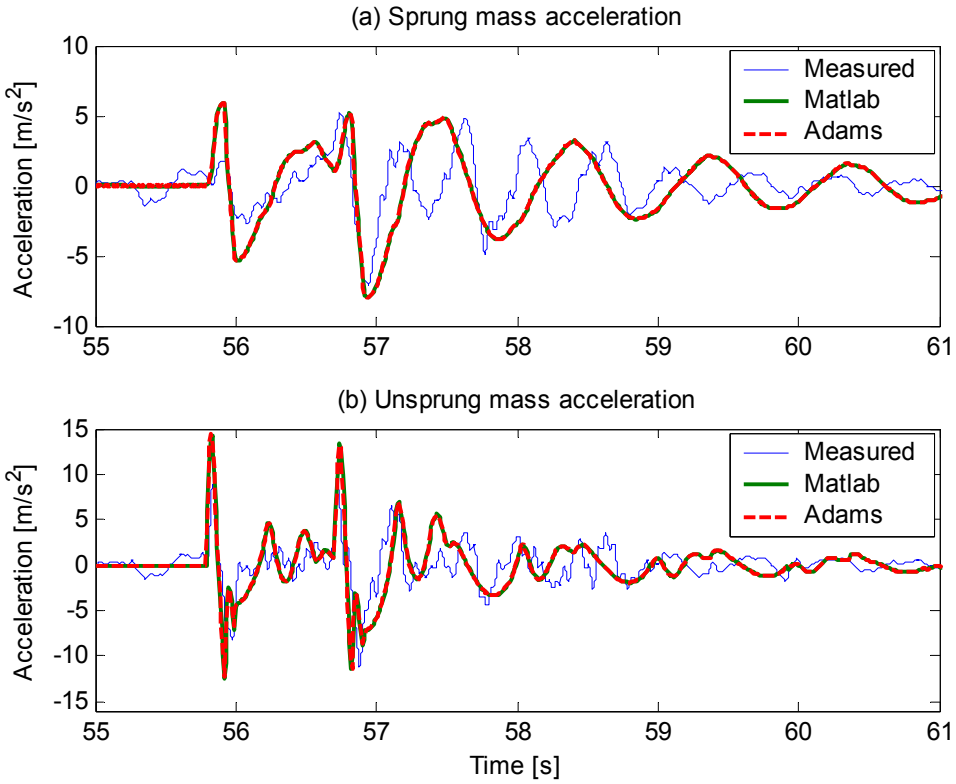

Figure 4.13 Quarter vehicle modelling results compared to measured data for the truck driven over two half-sine humps.

4.5 Bounce and pitch natural frequencies of the truck

The undamped bounce natural frequency of the quarter vehicle model with the parameters listed in section 4.4 is

$$f_{ns} = \frac{1}{2\pi}\sqrt{\frac{(\frac{k_s k_t}{k_s + k_t})}{M_s}} = 1\ Hz \qquad (4.2)$$

where the suspension spring stiffness $k_s = 2.6\times10^6\ N/m$, the tyre stiffness $k_t = 2.7\times10^6\ N/m$ and the sprung mass $M_s = 32895\ kg$. The suspension strut had a

non-linear spring characteristic. Strictly speaking, non-linearity implies that no distinct natural frequencies exist. However, using vehicle properties at static equilibrium, gives a very good indication of frequency regions in which large motions can be expected. Vehicle properties, linearised around the static equilibrium position, were used for the calculation in equation 4.2 and all other natural frequency calculations presented in this dissertation.

The bounce natural frequency of a vehicle, as defined at the centre of gravity, is determined by the front and rear tyre and suspension stiffness and the total mass of the vehicle. The parameters listed in section 4.4 represent one front corner of the haul truck. Subsequently, the bounce natural frequency of the quarter vehicle model that represents one front corner of the truck is calculated in equation 4.2. This value agrees well with the frequency close to 1 Hz at which the first peak in figure 4.9c appears (figure 4.9c presents the measured vertical acceleration power spectral density of the front right corner of the sprung mass of the truck).

Figure 4.9c also shows a peak just below 2 Hz. The measured pitch acceleration power spectral density of the sprung mass in figure 4.11c shows peaks at the same frequencies - near 1 and 2 Hz. Unless the quarter vehicle models that respectively represent the front and rear of a vehicle have equal bounce natural frequencies, pitch motion will be produced when the centre of gravity of the vehicle is excited in bounce. The converse is also true, in which case bounce motion will occur when the vehicle is excited in pitch. Pitch and bounce motions are therefore coupled.

Figure 4.14 shows a pitch-plane model that neglects suspension damping and the influence of the unsprung masses for simplicity. The equations of motion that describe this model are

$$M_s \ddot{z}_s + (k_{fRR} + k_{rRR}) z_s + (k_{fRR} b - k_{rRR} c)\theta_s = 0 \tag{4.3}$$

$$I_{\theta s} \ddot{\theta}_s + (k_{fRR} b - k_{rRR} c) z_s + (k_{fRR} b^2 + k_{rRR} c^2)\theta_s = 0 \tag{4.4}$$

Assuming harmonic motion, $z_s = Z_s \sin(\omega t)$ and $\theta_s = \theta_s \sin(\omega t)$, in which case

$$\frac{Z_s}{\theta_s} = \frac{-(k_{fRR} b - k_{rRR} c)}{(k_{fRR} + k_{rRR}) - \omega^2 M_s} \tag{4.5}$$

$$\frac{Z_s}{\theta_s} = \frac{-(k_{fRR} b^2 + k_{rRR} c^2) + \omega^2 I_{\theta s}}{(k_{fRR} b - k_{rRR} c)} \tag{4.6}$$

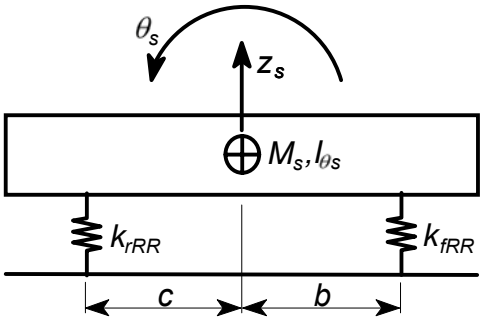

Figure 4.14 Vehicle pitch-plane model.

By setting the amplitude ratios in equations 4.5 and 4.6 equal to each other, the bounce and pitch natural frequencies can be calculated. Olley (edited by Milliken & Milliken, 2002) and Gillespie (1992) continue to do this. To calculate natural frequencies in this way, the rear suspension stiffness is required, which was not available. However, it is known that Z_s/θ_s will be positive at one of the natural frequencies. The associated oscillation centre will be behind the centre of gravity. Z_s/θ_s will be negative at the other natural frequency, and the oscillation centre ahead of the centre of gravity. One oscillation centre will also lie outside the wheelbase, and the other inside the wheelbase. Each oscillation centre will be a distance $x = Z_s/\theta_s$ from the centre of gravity (Gillespie, 1992).

Filtering measured vertical and pitch acceleration signals produces the graphs in figures 4.15a and b. The measured signals were each low-pass filtered with a cut-off frequency of 1.5 Hz (figure 4.15a) and band-pass filtered with a lower cut-off frequency of 1.5 Hz and an upper cut-off frequency of 3 Hz (figure 4.15b). Filtering was done in the frequency domain, which can be referred to as an "ideal filter" because of its exact cut-off properties and zero phase distortion.

The signals in figure 4.15a are 180° out of phase, while those in figure 4.15b are in phase. According to the sign convention in figure 4.14, Z_s/θ_s is therefore negative for motion at 1 Hz and positive for motion at 2 Hz. Taking the measuring locations and the Z_s/θ_s ratios determined from figure 4.15 into account, it is determined that

- The bounce oscillation centre is ahead of the front wheels
- The pitch oscillation centre is behind the centre of gravity, inside the wheelbase. (In fact, a pitch oscillation centre analysis involving the rear trailing arm suspension and the front suspension struts (that are rigidly fastened to the sprung mass) shows that the pitch oscillation centre is at the interface of the rear wheels with the ground. This however is not important for the present discussion and will not be further elaborated).

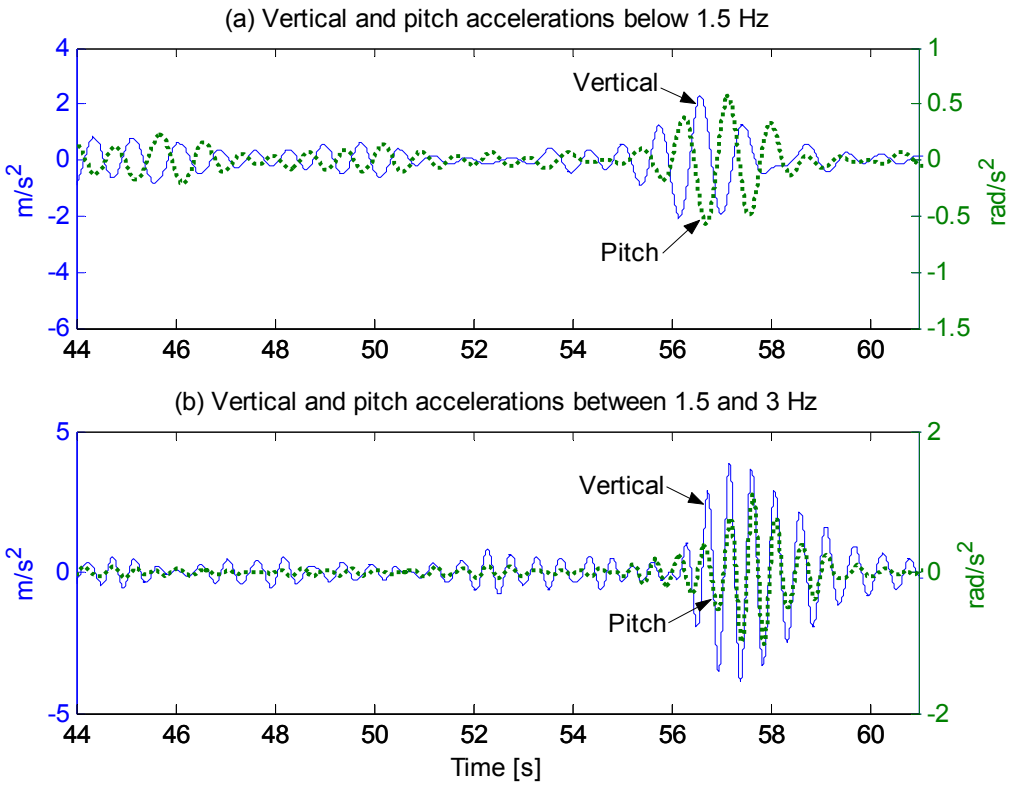

Figure 4.15 Comparison between sprung mass vertical and pitch accelerations in different frequency ranges.

What is important is that it has been verified that the peaks at 2 Hz in figures 4.9c and 4.11c involve pitch motion. This explains the inability of the quarter vehicle model to simulate the 2 Hz oscillatory motion of the measured sprung mass acceleration in figure 4.13a.

Interference kicks

It is interesting that the bounce and pitch natural frequencies are separated by almost 1 Hz. One of Olley's requirements for good ride is to have the bounce and pitch frequencies close together. The pitch frequency should not be more than 1.2 times the bounce frequency (Olley, edited by Milliken & Milliken, 2002). The frequencies of this truck differ significantly more. Olley also mentions that interference kicks resulting from superposition of motion are likely to happen if this constraint is violated. These are actually experienced by a passenger in the cab of the haul truck. This superposition manifests in the form of accelerations rather than displacements – the comparatively small displacements at the second natural frequency produces accelerations of the same magnitude as those at the first natural frequency.

4.6 Rigid body motion frequency ranges

Having determined the bounce and pitch natural frequencies, it becomes possible to specify frequency ranges in which rigid body motion dominates.

The only significant response in the sprung mass acceleration power spectral density in figure 4.9c appears in the regions of these two rigid body natural frequencies. It is therefore verified that acceleration below 10 Hz, measured on top of the suspension strut are dominated by rigid body motion and can be used under the rigid body assumption.

The unsprung mass acceleration power spectral density in figure 4.10c shows appreciable acceleration in a wider range. This is expected since the wheel hop frequency is commonly known to be higher than the sprung mass bounce natural frequency. For an independent front unsprung mass of the truck, the wheel hop frequency is estimated as

$$f_{nu} = \frac{1}{2\pi}\sqrt{\frac{k_s + k_t}{m_u}} = 3.96\ Hz \qquad (4.7)$$

where the unsprung mass $m_u = 8578.32\ kg$. Moreover, if the rigid body assumption applies to acceleration measurements on top of the suspension strut, it should be valid for measurements on top of the wheel spindle, since both components and the connection between them are stiff. It is therefore also concluded that accelerations below 10 Hz, measured on top the wheel spindle are dominated by rigid body motion and can be used under the rigid body assumption.

Vehicle response to road inputs is time dependant, and therefore dependent on the speed at which the road is traversed. A truck speed of 20 km/h and an upper cut-off frequency of 10 Hz for measured signals correspond to a road spatial wavelength of 0.56 m (or a ditch width of 0.28 m). However, whether the vehicle responds to such high frequency excitations at measurement locations is subject to tyre enveloping as explained in section 2.6. Figures 4.9 and 4.10 suggest that a cut-off frequency of 10 Hz is sufficient to capture essential road induced response data.

The pitch acceleration power spectral density in figure 4.11c contains large acceleration amplitudes at frequencies beyond the region of the dominant pitch natural frequency at 2 Hz. Although the cause for these large amplitudes is unsure, the bounce and pitch natural frequencies have been established. It should therefore be reasonable to discard measured pitch acceleration above 3 Hz under the rigid body assumption.

The roll natural frequency of the truck is calculated (Bastow, 1980) as

$$f_{nroll} = \frac{1}{2\pi}\sqrt{\frac{k_{fRR}L_f^2 + k_{rRR}L_r^2}{4I_{\phi s}}} = 0.98\ Hz \qquad (4.8)$$

where $k_{fRR} = 2\left(\frac{k_{sf}k_{tf}}{k_{sf}+k_{tf}}\right)$, $k_{rRR} = 2\left(\frac{k_{sr}k_{tr}}{k_{sr}+k_{tr}}\right)$, the spring stiffness of a single front suspension strut $k_{sf} = 2.6\times10^6\ N/m$, the spring stiffness of a single rear suspension strut at the equilibrium position is roughly estimated as $k_{sr} = 3\times10^6\ N/m$, the stiffness of a front tyre $k_{tf} = 2.7\times10^6\ N/m$ and the stiffness of the dual rear tyres on one side of the vehicle $k_{tr} = 5.4\times10^6\ N/m$. $I_{\phi s} = M_s k_{roll}^{\ 2}$, where a sprung mass value of $M_s = 1.44\times10^5\ kg$ and an estimated roll radius of gyration of $k_{roll} = 1.5m$ were used. The separation distance between the front suspension struts was approximated as $L_f = 3.7m$, while the separation distance between the rear suspension struts was approximated as $L_r = 1.8m$.

The roll natural frequency calculated in equation 4.8 corresponds well with the peaks just below 1 Hz in figure 4.12a to c. Gillespie (1985) mentions that the roll natural frequency of a highway truck lies between 0.5 and 1 Hz. Although the haul truck under consideration differs from a typical highway truck in design, the value calculated in equation 4.8 corresponds well with this range. Subsequently, a cut-off limit of 1.5 Hz was specified for measured roll motion. If a vehicle has equal mass and stiffness properties on the left and right sides, the roll natural frequency is expected to be decoupled from the bounce and pitch natural frequencies.

The cut-off frequencies determined in this section were used for all measured signals that are presented in this dissertation.

4.7 RDRM data in a seven degree of freedom (7DOF) vehicle model

Section 3.5.3 shows that the combined spring and damping forces calculated in the laboratory setup closely resembles the total force in the suspension strut. However, strut velocities are much higher when an operational vehicle encounters a large defect. Therefore, it was necessary to extrapolate the measured damping characteristic over a significant range. It would therefore be valuable to assess the accuracy with which suspension strut forces of an operational vehicle are calculated. The current section uses a 7DOF model in such an assessment.

The 7DOF vehicle model in chapter 2 is repeated in figure 4.16. An additional motion z_{sF1} is defined. The location of this motion corresponds to measuring locations 9 in figure 3.5.

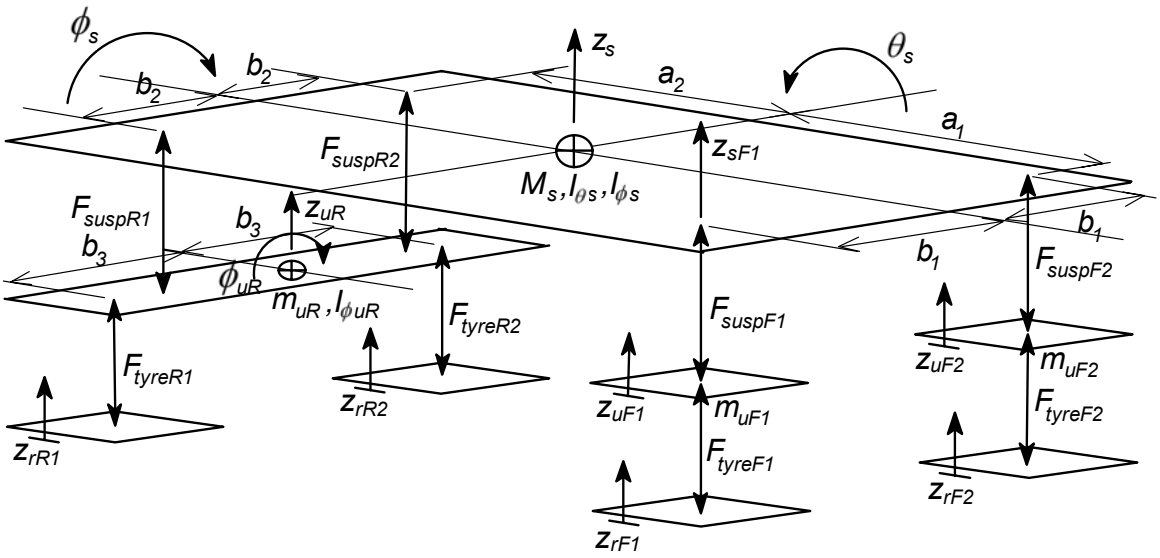

Figure 4.16 Schematic presentation of the 7DOF vehicle model with an additional measuring location $sF1$.

Rearranging equation 2.6

$$F_{suspR1} + F_{suspR2} = \frac{[(F_{suspF1} + F_{suspF2})a_1 - I_{\theta s}\ddot{\theta}_s]}{a_2}$$

and substituting into 2.5

$$F_{suspF1} + F_{suspF2} + \frac{[(F_{suspF1} + F_{suspF2})a_1 - I_{\theta s}\ddot{\theta}_s]}{a_2} = M_s\ddot{z}_s$$

$$F_{suspF1}(1+\frac{a_1}{a_2}) + F_{suspF2}(1+\frac{a_1}{a_2}) - \frac{I_{\theta s}\ddot{\theta}_s}{a_2} = M_s\ddot{z}_s \qquad (4.9)$$

by which F_{suspR1} and F_{suspR2} are eliminated. A kinematic relationship exists between $\ddot{z}_s$ and $\ddot{z}_{sF1}$. Assuming a small pitch angle θ_s and roll angle ϕ_s

$$\ddot{z}_s = \ddot{z}_{sF1} - \ddot{\theta}_s a_1 - \ddot{\phi}_s b_1$$

Using this relationship in 4.9 leads to

$$F_{suspF1}(1+\frac{a_1}{a_2})+F_{suspF2}(1+\frac{a_1}{a_2})-\frac{I_{\theta s}\ddot{\theta}_s}{a_2}=M_s(\ddot{z}_{sF1}-\ddot{\theta}_s a_1-\ddot{\phi}_s b_1)$$

Upon rearrangement

$$F_{suspF1}=-F_{suspF2}+\frac{[M_s\ddot{z}_{sF1}+(\frac{I_{\theta s}}{a_2}-M_s a_1)\ddot{\theta}_s-M_s b_1\ddot{\phi}_s]}{(1+\frac{a_1}{a_2})} \tag{4.10}$$

and

$$M_s\ddot{z}_{sF1}=F_{suspF1}(1+\frac{a_1}{a_2})+F_{suspF2}(1+\frac{a_1}{a_2})-(\frac{I_{\theta s}}{a_2}-M_s a_1)\ddot{\theta}_s+M_s b_1\ddot{\phi}_s \tag{4.11}$$

The equation of motion of unsprung mass m_{uF1} is

$$-F_{suspF1}+F_{tyreF1}=m_{uF1}\ddot{z}_{uF1} \tag{4.12}$$

A positive F_{tyreF1} will exert an upward force on m_{uF1}. Thus, for the case where the tyre is represented as a simple spring

$$F_{tyreF1}=-k_t(z_{uF1}-z_{rF1}) \tag{4.13}$$

For further reference 4.12 is rearranged as

$$F_{tyreF1}=F_{suspF1}+m_{uF1}\ddot{z}_{uF1} \tag{4.14}$$

Substituting 4.10 into 4.14 gives

$$F_{tyreF1}=m_{uF1}\ddot{z}_{uF1}-F_{suspF2}+\frac{[M_s\ddot{z}_{sF1}+(\frac{I_{\theta s}}{a_2}-M_s a_1)\ddot{\theta}_s-M_s b_1\ddot{\phi}_s]}{(1+\frac{a_1}{a_2})} \tag{4.15}$$

Equation 4.11 is the first by which the accuracy of suspension strut force calculations is determined. The measured sprung mass acceleration on the left hand side of this equation

is compared to the right hand side that contains the quantities of left and right suspension strut forces, pitch acceleration and roll acceleration. Figure 4.17 displays the results (both sides of equation 4.11 are divided by M_s to have units of acceleration in the comparison).

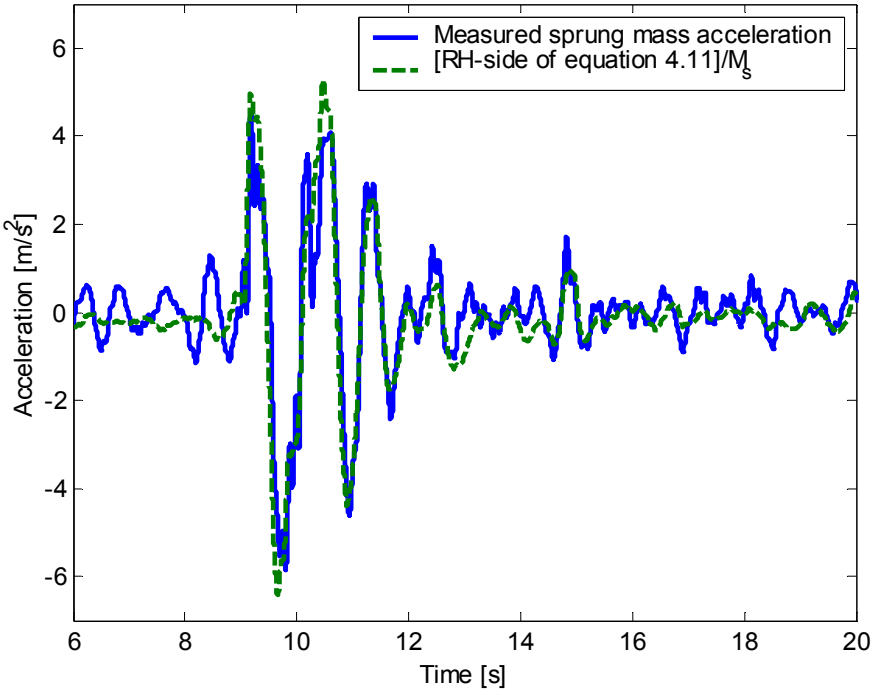

Figure 4.17 Measured sprung mass acceleration compared to the right hand side of equation 4.11.

The measured sprung mass acceleration is resembled accurately. The calculated damping characteristic was used to obtain the left and right front suspension strut damping forces that are required by the right hand side of equation 4.11. The equation also contains the pitch mass moment of inertia of the sprung mass $I_{\theta s}$. $I_{\theta s} = M_s k_{pitch}^{\ 2}$, where a sprung mass value of $M_s = 1.44 \times 10^5\, kg$ and pitch radius of gyration of $k_{pitch} = 2\, m$ were used. As established in section 4.6, pitch acceleration above 3 Hz, roll acceleration above 1.5 Hz and vertical acceleration above 10 Hz were discarded.

The suspension strut force that was calculated directly from strut pressure and the damping characteristic is also compared to the suspension strut force that was calculated through equation 4.10. The difference between equations 4.10 and 4.11 is that the latter groups all direct suspension strut force calculation terms on the one side, while equation 4.10 necessitates suspension strut force calculations in a direct way on both sides of the equation. Nonetheless, the comparison is made and presented in figure 4.18.

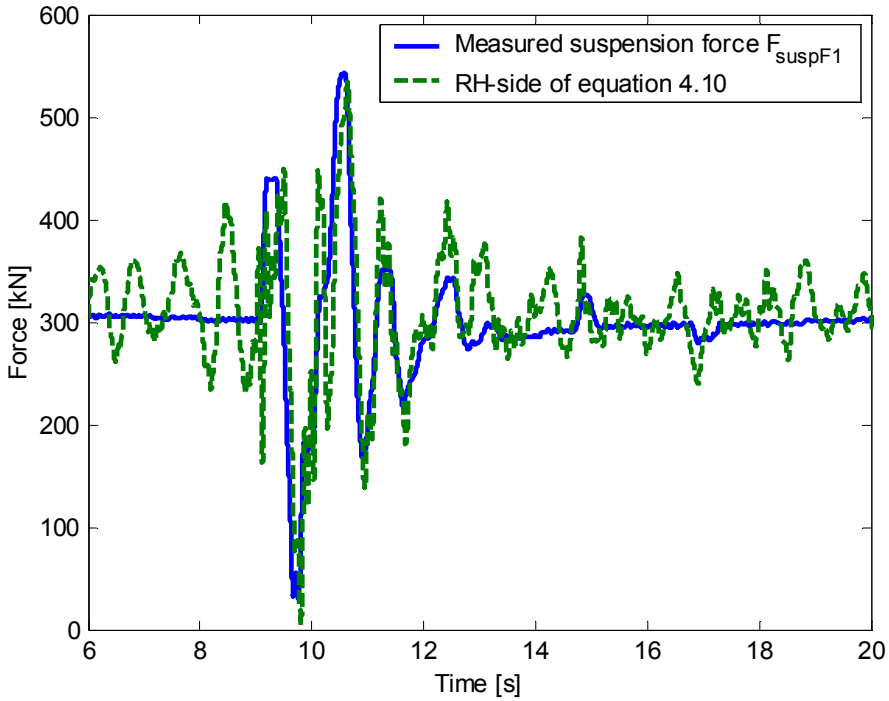

Figure 4.18 The right front suspension strut force calculated through the stiffness and damping characteristics compared to the right hand side of equation 4.10.

Finally, the tyre force was calculated through equation 4.14, in which the suspension strut force is calculated through the characteristics (also referred to as the direct way of suspension strut force calculation in this section). This is compared to the tyre force calculated through equation 4.15, in which the right suspension strut force is eliminated (the force in the left front suspension strut is not eliminated). The comparison is presented in figure 4.19. Gravitational acceleration is not included in figure 4.17, while static forces are included in figures 4.18 and 4.19.

The extrapolated damping characteristic in section 3.4 can only be verified through experimental data or a detailed analysis. Nonetheless, figures 4.17 to 4.19 prove suspension strut force calculation with the stiffness and damping characteristics accurate. It is even possible that forces calculated with these characteristics are more accurate than those calculated using pitch acceleration, roll acceleration, etc., which are also possible sources of error. This is especially true, since all rigid body motions that might have been present at frequencies higher than the cut-off limits defined for these signals, were discarded in an attempt to differentiate between rigid body and non-rigid body motion. Moreover, the pitch radius of gyration k_{pitch} was estimated and not measured.

Section 4.8 uses the 7DOF model in simulations. A sensitivity analysis in which the damping characteristic is changed by 10% shows that the vehicle is insensitive to

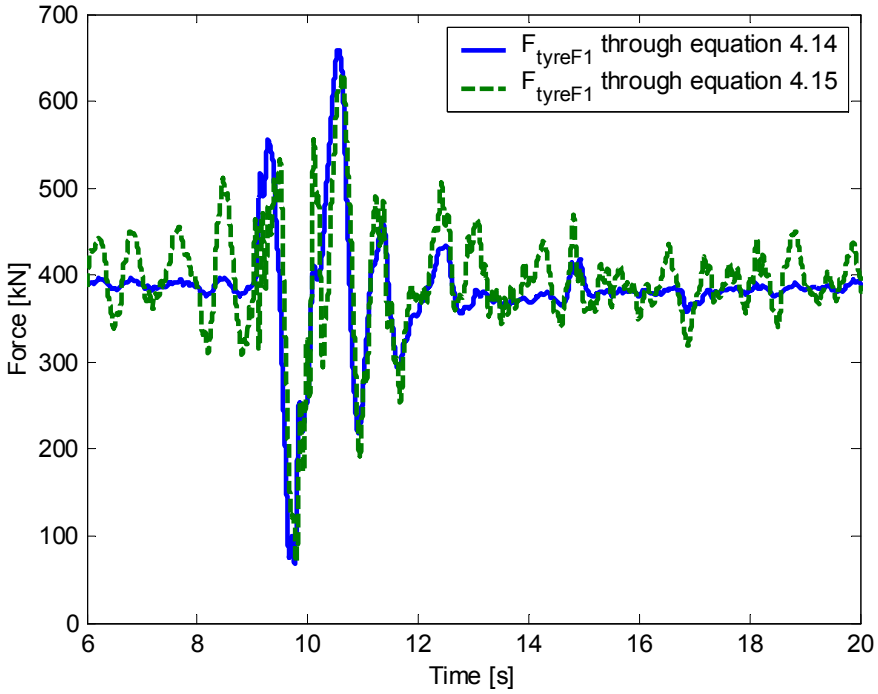

Figure 4.19 The tyre force calculated using the right front suspension strut force compared to the tyre force calculated by eliminated the right front suspension strut force.

variations of this order. Even larger variations have insignificant consequences on both modelling and defect reconstruction results.

4.8 Seven degree of freedom (7DOF) vehicle modelling results

The 7DOF vehicle model in section 4.7 can also be used in simulations. Similar to the quarter vehicle simulations, the road displacement is provided as input, upon which unsprung and sprung mass motions are calculated. The aim of this section is to enhance modelling accuracy by including sprung mass pitch and roll degrees of freedom. Equations 4.11, 4.12 and 4.13 can be combined in matrix form

$$\begin{bmatrix} M_s & 0 \\ 0 & m_{uF1} \end{bmatrix}\begin{bmatrix} \ddot{z}_{sF1} \\ \ddot{z}_{uF1} \end{bmatrix} = \begin{bmatrix} 0 & 0 \\ 0 & -k_t \end{bmatrix}\begin{bmatrix} z_{sF1} \\ z_{uF1} \end{bmatrix} + \begin{bmatrix} 0 \\ k_t \end{bmatrix} z_{rF1}$$
$$+ \begin{bmatrix} (1+\frac{a_1}{a_2}) \\ -1 \end{bmatrix} F_{suspF1}(z_{sF1}, \dot{z}_{sF1}, z_{uF1}, \dot{z}_{uF1}) + \begin{bmatrix} (1+\frac{a_1}{a_2}) \\ 0 \end{bmatrix} F_{suspF2} + \begin{bmatrix} M_s a_1 - \frac{I_{\theta s}}{a_2} \\ 0 \end{bmatrix} \ddot{\theta}_s + \begin{bmatrix} M_s b_1 \\ 0 \end{bmatrix} \ddot{\phi}_s \quad (4.16)$$

Similar to the quarter vehicle simulations, this set of differential equations was solved with the Runge-Kutta integration scheme. Although Runge-Kutta requires an n-th order equation to be written as n first order equations, it is not a concern in the present case since the system is small. The two second order equations of equation 4.16 change to four first order equations. Subsequently

$$\begin{bmatrix} 1 & 0 & 0 & 0 \\ 0 & 1 & 0 & 0 \\ 0 & 0 & \mathrm{M_s} & 0 \\ 0 & 0 & 0 & m_{uF1} \end{bmatrix} \begin{bmatrix} \dot{z}_{sF1} \\ \dot{z}_{uF1} \\ \ddot{z}_{sF1} \\ \ddot{z}_{uF1} \end{bmatrix} = \begin{bmatrix} 0 & 0 & 1 & 0 \\ 0 & 0 & 0 & 1 \\ 0 & 0 & 0 & 0 \\ 0 & -k_t & 0 & 0 \end{bmatrix} \begin{bmatrix} z_{sF1} \\ z_{uF1} \\ \dot{z}_{sF1} \\ \dot{z}_{uF1} \end{bmatrix} + \begin{bmatrix} 0 \\ 0 \\ 0 \\ k_t \end{bmatrix} z_{rF1}$$
$$+ \begin{bmatrix} 0 \\ 0 \\ (1+\frac{a_1}{a_2}) \\ -1 \end{bmatrix} F_{suspF1}(z_{sF1}, \dot{z}_{sF1}, z_{uF1}, \dot{z}_{uF1}) + \begin{bmatrix} 0 \\ 0 \\ (1+\frac{a_1}{a_2}) \\ 0 \end{bmatrix} F_{suspF2} + \begin{bmatrix} 0 \\ 0 \\ M_s a_1 - \frac{I_{\theta s}}{a_2} \\ 0 \end{bmatrix} \ddot{\theta}_s + \begin{bmatrix} 0 \\ 0 \\ M_s b_1 \\ 0 \end{bmatrix} \ddot{\phi}_s \qquad (4.17)$$

Treating F_{suspF2}, $\ddot{\theta}_s$ and $\ddot{\phi}_s$ as known variables (F_{suspF2} can be calculated from measured suspension strut data, while $\ddot{\theta}_s$ and $\ddot{\phi}_s$ were measured during RDRM), together with the road input z_{rF1}, it is possible to solve the set of differential equations in equation 4.17, and calculate the vertical motions of unsprung mass m_{uF1} and the sprung mass at location $sF1$. Like before, sprung mass motion at location sF_1 is of interest since this is where one of the accelerometers was mounted during RDRM. Through kinematic relationships, motions at any other point on the rigid body sprung mass can be calculated, if required.

Figure 4.20 compares simulation results to measured accelerations for the haul truck driven over the two half-sine humps. The same unsprung mass, stiffness and damping parameters as for the quarter vehicle model that produced the results in section 4.4 were used. As in section 4.7, values of $M_s = 1.44 \times 10^5\ kg$ and $k_{pitch} = 2\,m$ were used.

It is clear that the latter parts of the measured accelerations in figure 4.20 are simulated much more accurately than with the quarter vehicle model. Thus, it has been verified that pitch dominates the oscillatory motion at 2 Hz. Hence, it is also confirmed that static friction inside the suspension strut is not responsible for this effect, and therefore suspension strut force calculations through the stiffness and damping characteristics are accurate enough for defect response reconstruction of this kind. Section 4.10 presents defect reconstruction results in which the suspension strut stiffness and damping characteristics were used to calculate the strut forces. Appendix F compares 7DOF vehicle simulation results to measured data for the truck driven over the two larger defects, while Appendix G presents a sensitivity analysis in which this 7DOF vehicle simulation model was used. The next section discusses the forces in the trailing arm and

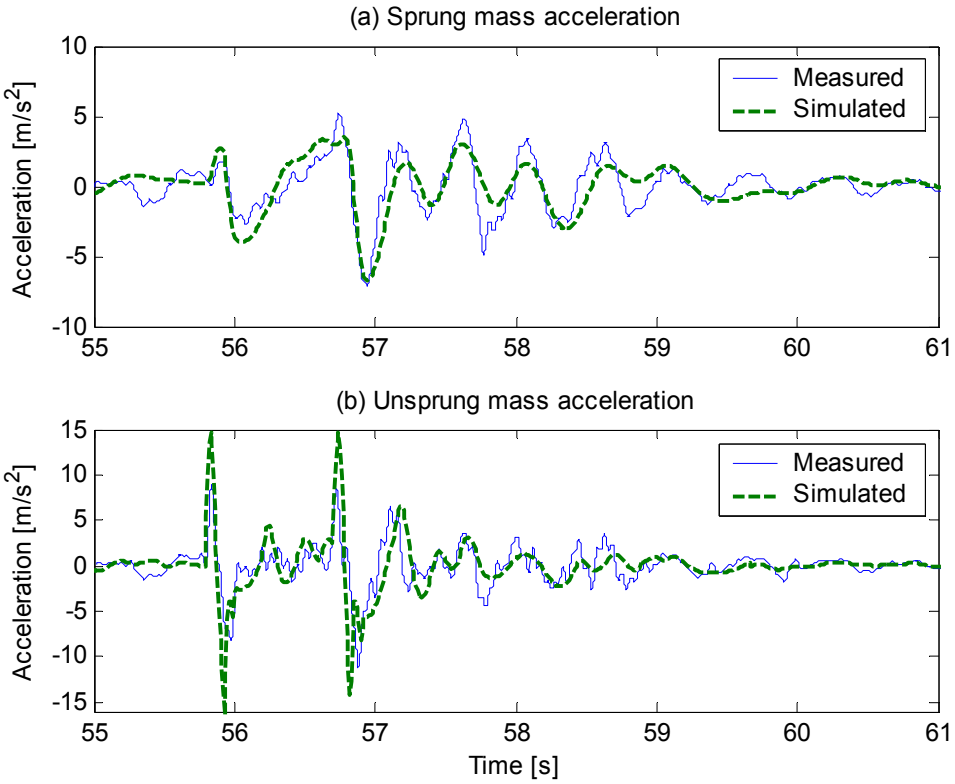

Figure 4.20 7DOF vehicle modelling results compared to measured data for the truck driven over two half-sine humps.

longitudinal acceleration of the vehicle that were neglected in the derivation of the 7DOF vehicle model.

4.9 Trailing arm forces and longitudinal acceleration

One function of the trailing arm is to counter squat (rearward pitch) during longitudinal acceleration and dive (forward pitch) during longitudinal deceleration (braking). It does not change the steady load transfer between the front and rear wheels. The trailing arm rather carries a portion of the load and therefore alters the load working through the rear suspensions struts. Consequently, vehicle pitch is altered.

The amount of pitch alteration is determined by the location of the instantaneous centre of zero velocity on the sprung mass. This location is the pivot point of the trailing arm of this haul truck. Figure 4.21 shows a free-body diagram of the rear drive axle of the truck during acceleration. Following Gillespie (1992) and Olley (edited by Milliken & Milliken, 2002), the weight of the unsprung mass is neglected.

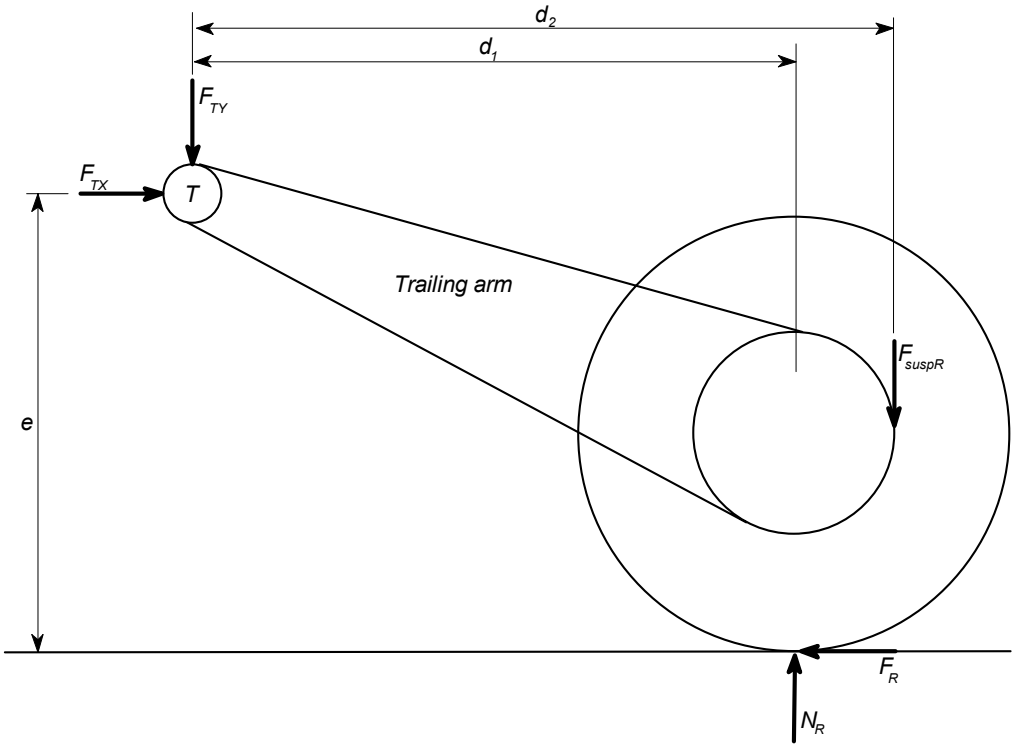

Figure 4.21 Free-body diagram of the rear drive axle of the truck during acceleration.

Writing equations of equilibrium for the vertical direction and for moments around point T yields

$$N_R - F_{suspR} - F_{TY} = 0 \tag{4.18}$$

$$N_R d_1 - F_{suspR} d_2 - F_R e = 0 \tag{4.19}$$

Rewriting and substituting 4.19 into 4.18

$$F_{TY} = F_{suspR}(\frac{d_2}{d_1} - 1) + F_R \frac{e}{d_1} \tag{4.20}$$

During acceleration $F_R = ma_x$ for this solid rear drive axle vehicle, in which case

$$F_{TY} = F_{suspR}(\frac{d_2}{d_1} - 1) + ma_x \frac{e}{d_1} \tag{4.21}$$

where m is the vehicle mass and a_x is the vehicle longitudinal acceleration. All resistance forces acting on the vehicle such as aerodynamic forces are neglected in this equation.

In the absence of longitudinal acceleration, the second term on the right hand side of equation 4.20 disappears. Since d_1 does not equal d_2, the first term on the right hand side of this equation however remains. Consequently, there is a vertical force in the trailing arm even if the truck drives at a constant speed or is stationary. The magnitude of this force is determined by the difference between d_1 and d_2. The relationship between F_{TY} and F_{suspR} in equation 4.20 can be used in a 7DOF model that takes this vertical trailing arm force into account, by which all vertical forces acting on the sprung mass, other than front suspension strut forces can then be eliminated. The 7DOF model in section 4.7 can be extended for such purposes.

Apart from vertical trailing arm forces, the 7DOF model in section 4.7 also neglects longitudinal load transfer between the front and rear of the vehicle during acceleration. A more complex model is required if this effect is to be included without neglecting the inertial effects of the unsprung masses. Regarding such a model, the following is noted: Some portion of the load transferred between the front and rear of the vehicle acts through the rear suspension struts and the rest through the trailing arm. During simulation, it will therefore be required to determine these portions; the second term on the right hand side of equation 4.20 represents the portion that acts through the trailing arm due to vehicle longitudinal acceleration (or deceleration, in which case F_R will be negative).

Equation 4.21 represents the case where this solid rear drive axle vehicle is accelerated by the torque of the wheel motors and all traction forces act at the contact patches of the rear wheels. This equation shows that in this case it is possible to represent F_{TY} in a 7DOF vehicle model through the longitudinal acceleration of the vehicle, which can be measured. For the case where the vehicle brakes however, it is necessary to know the brake proportioning between the front and rear wheels to calculate F_R and do a similar analysis. Longitudinal load transfer between the front and rear of the vehicle during impact with large obstacles is really of interest in the present case. Similar to the above cases, F_R will be required to calculate the portions of the transferred load that act though the rear suspension struts and the trailing arm respectively. This will be difficult to determine.

The mass of the rear axle is neglected from the outset in the above derivation. This assumption is possibly inaccurate since the rear axle that contains the wheel motors has a substantial weight. Moreover, if large obstacles are encountered, large accelerations are present, which result in substantial inertial forces. This can violate equation 4.20.

Correlation is still good in sections 4.7 and 4.8 even though the vertical trailing arm force and longitudinal acceleration of the vehicle were neglected. This indicates that these aspects are of secondary importance.

4.10 Defect reconstruction

The preceding sections of this chapter study the dynamics of the truck and assess the accuracy with which suspension strut forces can be calculated. The topic of this section is defect reconstruction.

Section 2.4 mentions two methods by which the road profile can be reconstructed. The one is by using the calculated tyre force, the unsprung mass displacement and an inverse tyre model. The second is through a simulation model in which the road input is changed until simulated response matches measured response.

Treating the tyre as a simple linear spring allows inversion by simply rewriting the algebraic expression in equation 4.13

$$z_{rF1} = z_{uF1} + \frac{F_{tyreF1}}{k_t} \tag{4.22}$$

F_{tyreF1} in equation 4.22 can be calculated through equation 4.14 by using the measured unsprung mass acceleration directly and calculating F_{suspF1} through the suspension strut pressure, strut velocity and the calculated strut characteristics. The only unknown that then remains in equation 4.22 is the unsprung mass displacement. Absolute measurement of displacement is difficult. The obvious alternative is to integrate the unsprung mass acceleration twice. This however also has some difficulties associated (See Appendix D).

Nonetheless, measured unsprung mass acceleration was integrated twice in the frequency domain with no lower cut-off frequency. This was used in equation 4.22 to calculate the road profile over which the truck drove during one run on the west section, as explained above. The resulting profile is displayed in figure 4.22. The unsprung mass displacement was also calculated through integration of the unsprung mass acceleration with a lower cut-off frequency of 0.45 Hz. The resulting profile is displayed in figure 4.23.

A vast amount of drift is present in figure 4.22, while the profile in figure 4.23 omits important frequency content. (A double-sided exponential window was used for these signals and others presented in this dissertation that were analysed in the frequency domain, e.g. the power spectral densities in figures 4.9 to 4.12). Defect geometries are

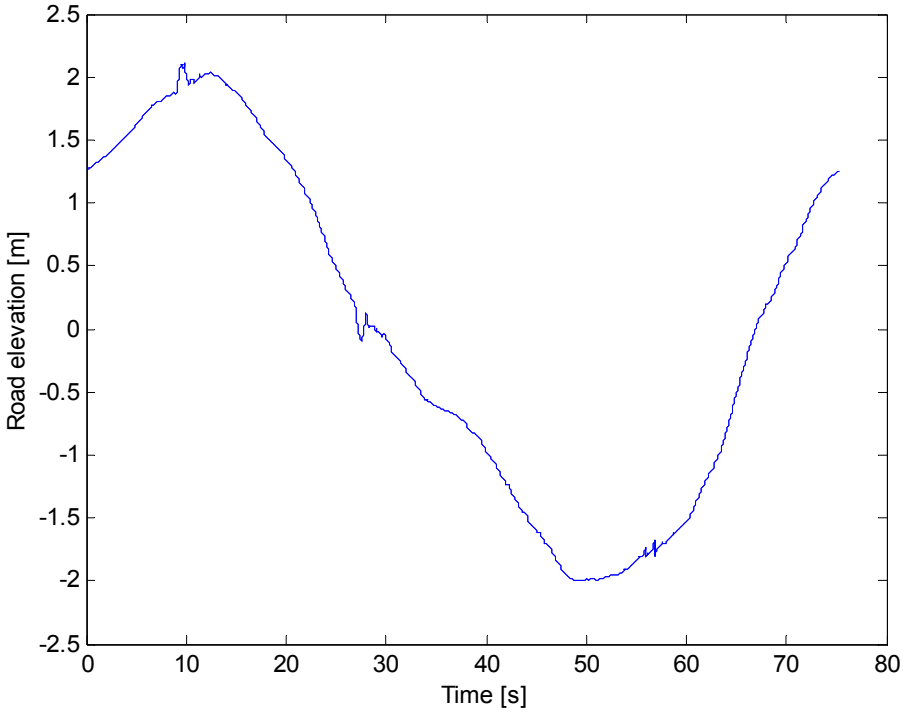

Figure 4.22 Reconstructed west section road profile using no lower cut-off frequency and a 10 Hz upper cut-off frequency.

identifiable in figure 4.22 despite the low frequency drift. This is not possible from the profile in figure 4.23 that discards low frequency content.

Using the speed of the vehicle, the profile in figure 4.22 was transformed to the spatial domain and is presented in figure 4.24. Figure 4.25a to c zooms in on the three defects in the profile of figure 4.24. The low frequency drift was removed from these plots by fitting third order polynomials to subsections of the profile that contained defects and subtracting these trends. The sections chosen for fitting these polynomials were substantially larger than the defects to ensure that only the trend was removed and not part of the defect geometry. The figure compares reconstructed defect geometries to the simulated geometries of the actual defects. Figure 4.26 compares the reconstructed defect geometries to the simulated geometries of the three defects on the east section.

Simply using the integrated unsprung mass displacement is also useful to identify defects. Figure 4.27 compares the calculated west section road profile to the unsprung mass displacement.

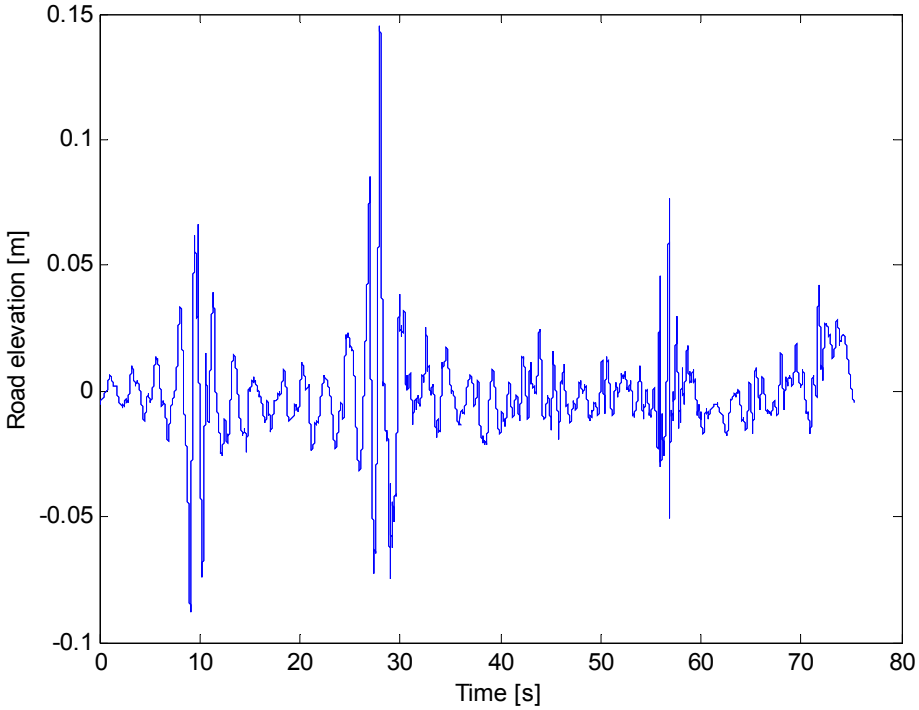

Figure 4.23 Reconstructed west section road profile using a 0.45 Hz lower cut-off frequency and a 10 Hz upper cut-off frequency.

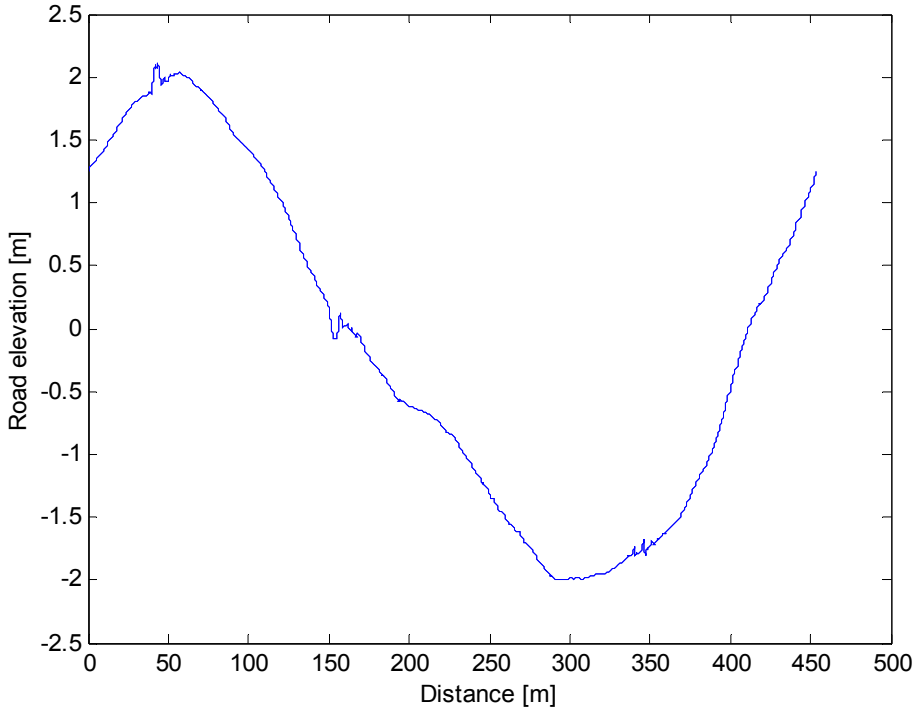

Figure 4.24 Reconstructed west section road profile in the spatial domain.

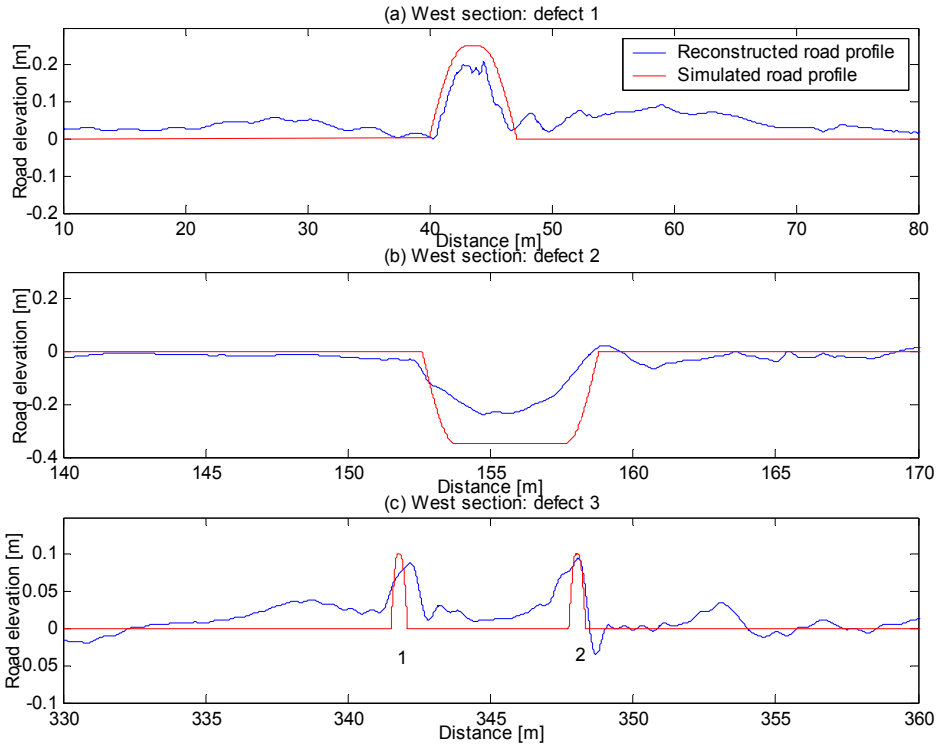

Figure 4.25 Comparison between the simulated and reconstructed west section defects.

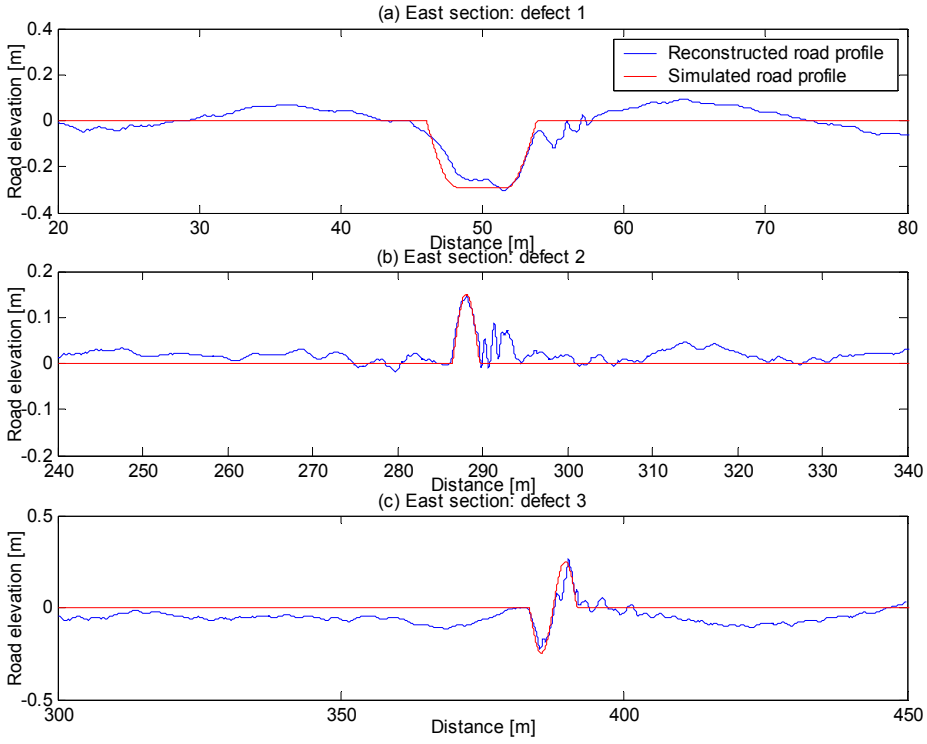

Figure 4.26 Comparison between the simulated and reconstructed east section defects.

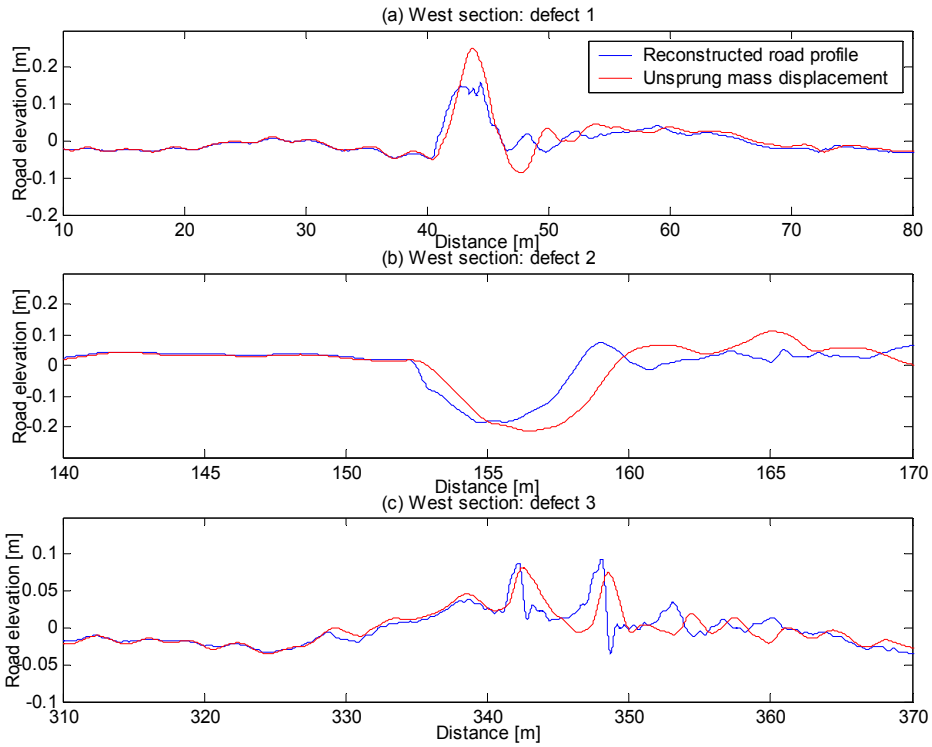

Figure 4.27 Comparison between the reconstructed west section road defect geometries and the unsprung mass displacement.

All the defects presented in this section were reconstructed using the measured vertical tyre stiffness as discussed in section 3.4. Appendix H presents results in which the same defects were reconstructed using a tyre stiffness value of $k_t = 5 \times 10^6 \, N/m$. In this Appendix, the shapes of most of the defects are evidently better reconstructed, while the dimensions of the defects presented in the current section compares better with measured defect dimensions (these are presented below). The suggestion is not that the measured tyre stiffness characteristic is wrong (sections 4.4 and 4.8 prove this with accurate simulations with the rigid treadband tyre model in which the measured tyre stiffness was used), but rather that the point-follower method as used for defect reconstruction is lacking. For this reason, investigation into more sophisticated tyre models is one of the primary recommendations flowing from this research.

The accuracy of defect reconstruction

Figures 4.25 and 4.26 show the accuracy with which defect shapes are reconstructed. Subsequently, dimensions of reconstructed and measured defects are compared. Table 4.1 lists the measured, treadband-filtered and reconstructed widths of the defects in figures 4.25 and 4.26. W_m is the measured width, W_f is the treadband-filtered width and W_r is

the reconstructed width. The important comparison in this table is between measured (actual) defect width and reconstructed width.

Table 4.1 Measured, treadband-filtered and reconstructed defect widths.

Figure	Defect type	$W_m[m]$	$W_f[m]$	$W_r[m]$
4.25a	Hump	7.2	7.43	6.32
4.25b	Ditch (Oblique)	6.2	6.2	6.52
4.25c 1	Hump	0.6	1.36	1.60
4.25c 2	Hump	0.6	1.36	1.52
4.26a	Ditch	7.8	7.8	9.07
4.26b	Hump	3.2	3.46	3.56
4.26c	Ditch & hump	8.4	8.57	9.15

Table 4.2 lists the measured and reconstructed defect heights. H_m is the measured height (or depth) and H_r is the reconstructed height (or depth). Measured and treadband-filtered defect heights are the same.

Table 4.2 Measured and reconstructed defect heights.

Figure	Defect type	$H_m[m]$	$H_r[m]$
4.25a	Hump	0.25	0.190
4.25b	Ditch (Oblique)	0.35	0.224
4.25c 1	Hump	0.1	0.070
4.25c 2	Hump	0.1	0.082
4.26a	Ditch	0.29	0.267
4.26b	Hump	0.15	0.151
4.26c	Ditch & hump	0.5	0.489

Table 4.3 presents reconstructed defect widths as percentages of respectively measured and treadband-filtered widths. From this table it is evident that the reconstructed widths W_r are much larger than the measured widths W_m for the two small humps in figure 4.25c. This gives some illustration of the effect of tyre enveloping on small defect reconstruction. Although the circular rigid treadband tyre model does not consider enveloping, it does approximate the trajection of the tyre over the road profile and thereby filters some high frequency content. Figure 4.8b visually illustrates how this model alters the section of profile that contains these two defects. Table 4.3 also indicates that the treadband-filtered widths W_f compare much more favourable to the reconstructed widths W_r. It is believed that tyre response over many defects is determined by a combination of these two effects: Firstly, the tyre can simply not follow

the profile of the road exactly. Secondly, some high frequency content is filtered due to enveloping.

Table 4.3 Reconstructed defect widths as percentages of respectively measured and treadband-filtered defect widths.

Figure	Defect type	$\frac{W_r}{W_m}(\%)$	$\frac{W_r}{W_f}(\%)$
4.25a	Hump	88	85
4.25b	Ditch(Oblique)	105	105
4.25c 1	Hump	267	118
4.25c 2	Hump	253	112
4.26a	Ditch	116	116
4.26b	Hump	111	103
4.26c	Ditch & hump	109	107

Table 4.4 presents reconstructed defect heights as percentages of measured heights.

Table 4.4 Reconstructed defect heights as percentages of measured defect heights.

Figure	Defect type	$\frac{H_r}{H_m}(\%)$
4.25a	Hump	76
4.25b	Ditch(Oblique)	64
4.25c 1	Hump	70
4.25c 2	Hump	82
4.26a	Ditch	92
4.26b	Hump	101
4.26c	Ditch & hump	98

Reconstruction results are good in general. Firstly, the locations of defects are identified reliably. Secondly, different defect types are distinguished, i.e. humps and ditches. Finally, a simple comparison of defect width and height shows that it is possible to reconstruct geometries with an accuracy sufficient to fulfil the requirements of defect recognition for road maintenance purposes.

Chapter 5

Qualitative road condition assessment

Chapter 1 mentions that road roughness evaluations are used in the management of both paved and unpaved roads. The difference however, is that measured information is used for paved road maintenance management, while unpaved road maintenance management systems are limited to predictive models, due to a number of reasons that are mentioned. While chapter 4 completes the discussion on large defect reconstruction, this chapter expands some of the concepts and analyses that have been developed in the preceding chapters to study the feasibility of haul truck response as a measure of road roughness.

Firstly, the IRI standard for road roughness measurements and in particular its relation to response-type systems are discussed. The importance of haul road roughness evaluations and the limitations of currently used scoring methods that are based on subjective or predictive evaluations are elaborated. The inherent response characteristics of the haul truck that pertains to the measurement of road roughness is studied, after which processed data is presented and discussed.

5.1 Road roughness measurement and the IRI standard

Perhaps the most important reason the profile of a road is measured, is to obtain an indication of its roughness. Sayers & Karamihas (1998) mentions several definitions that may be used to describe road roughness. Among them is the definition of the American Society of Testing and Materials (ASTM) that describes road roughness as

“The deviation of pavement surface from a true planar surface with characteristic dimensions that affect vehicle dynamics, ride quality, dynamic loads, and drainage, for example, longitudinal profile, transverse profile and cross slope”.

Key to this definition is the connection it makes between the characteristics of a profile and the very purposes for which an objective measure is sought. Class 3 profilers measure vehicle motion that directly relates to the characteristics of the road that influence vehicle dynamics and should therefore be suitable for road roughness assessment according to ASTM’s definition.

Since not all profilers measure the actual road profile, comparison between measurements with different instrumentation was problematic in the past. It was also not possible to compare measurements with different response-type systems or the same response-type

system over time due to differing and time changing vehicle parameters (Gillespie et al., 1980). A standard was sought that would enable comparison of measurements made with profilers from different classes and also provide a calibration reference for response-type systems.

The International Roughness Index (IRI) was developed to address these requirements. This index is based on the same principle as response-type systems and is therefore a worthy measure of road roughness. The IRI is calculated from the simulated suspension motion of a quarter vehicle model with standardised parameters (figure 5.1). These parameters do have standard units of N/m, etc. and therefore the factors that relate each parameter to M_s have units of $1/s^2$, etc. A road profile measured with a class 1 or 2 device forms input to this model. IRI is then calculated as

$$IRI = \frac{1}{L}\int_0^{L/S} \left|\dot{z}_s - \dot{z}_u\right| dt \qquad (5.1)$$

where L is the length of the profile in km and S is the standard simulation speed of 80 km/h. IRI has units of m/km.

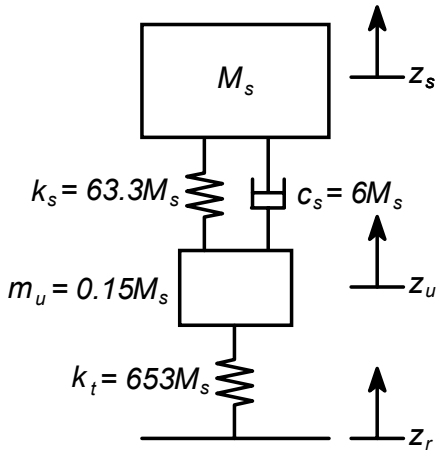

Figure 5.1 The standard quarter vehicle model (Gillespie, et al., 1980; Sayers & Karamihas, 1998).

Since the characteristics of this standard simulation vehicle and real vehicles differ, IRI values calculated with the simulation vehicle and the equivalent of IRI measured with a real vehicle (response-type system) differ. However, a correlation can be found between actual IRI (calculated with the standard simulation vehicle) and the equivalent of IRI (measured with a real vehicle) over a range of road roughness. This correlation can be used to convert response-type system measurements to IRI.

The IRI therefore enables correlation between measurements with different systems through

- The calculation of IRI from actual profiles measured with class 1 and 2 profilers.
- Correlation between response-type system measurements and IRI.

As a result, different response-type systems can be used and calibrated.

5.2 Road roughness evaluation in perspective

5.2.1 Applications of road roughness evaluations

Gillespie et al. (1980) identify some functions of objective road roughness measurements

- As a means of monitoring the overall condition of a road network.
- As information needed for decision on allocation of maintenance funds.
- As a measure of the quality of new construction.
- As a historical measure of pavement performance that can be used in evaluation of alternative construction designs.

Several authors confirm the importance of road roughness information in unpaved road maintenance management systems. Archondo-Callao (1999a) states that road agencies need a measure of the roughness of roads as an input to pavement management systems, and whenever the economic feasibility of proposed expenditures on maintenance or upgrading is to be determined. Dierks (1992) finds road roughness to be the principal measure of pavement condition that can be related to vehicle operating costs. Thompson and Visser (2003) confirm by realising the importance of rolling resistance progression with time as a measure of pavement condition in a mine haul road maintenance management system.

5.2.2 Current unpaved road roughness evaluation methods

Predictive road roughness models find application in unpaved road maintenance management systems (Thompson & Visser, 2003; Dierks, 1992). However, road roughness at a particular point in time is, amongst others a function of the interaction between traffic and the road surface. In cases where variables such as traffic volume are difficult to predict, sub-optimal maintenance strategies are likely to be applied (Thompson, et al., 2003).

Besides measuring (as with class 1, 2 or 3 profilers) and predicting unpaved road roughness, subjective ratings can be used. These are class 4 profiling methods. Such methods are used in some cases (Thompson & Visser, 2000; Dierks, 1992; Archondo-Callao, 1999b) but Archondo-Callao (1999b) makes it clear that subjective estimations

should not be used when measurements are feasible. Correlation models exist to relate subjective ride quality ratings to objective road roughness measurements (Dierks, 1992; Archonda-Callao, 1999a).

Relating the above to mine haul roads specifically, the following points are important

- Knowledge of the roughness of a haul road is desired and used in haul road maintenance management systems such as developed by Thompson and Visser (2003).
- Predictive models and subjective evaluations are currently in use. These methods are inferior to physical measurements.

The rest of this chapter discusses the possibility of using haul truck response as a measure of haul road roughness. Generally, operational vehicles are not used as profilers. However, there are large benefits to such a concept in the present case (Chapter 1). The intention around which this discussion evolves is that of using the haul truck in a way similar to a response-type system that measures suspension motion or the equivalent.

5.3 Response characteristics of the haul truck

The frequency response characteristics of response-type systems differ. During the time of investigation into a possible standard for calibration, different response-type systems were investigated (Gillespie et al., 1980). A standard was sought that resemble general response-type characteristics well. The standard quarter vehicle was established with a little more suspension damping than most real response-type vehicles to avoid “tuning” to certain frequencies and thus have good correlation with a range of vehicles with slightly differing frequency response characteristics.

However, frequency response characteristics of response-type systems can differ quite severely from that of the standard quarter vehicle. Some systems were found to have good low frequency response characteristics, while others were found to be responsive to high frequency features.

Despite differences in their frequency response characteristics, correlation between measurements with different response-type systems and IRI are generally possible. Gillespie et al. (1980) mentions an interesting point. They refer to the similarities between the spectral densities of different roads. Models exist that characterise roads according to frequency characteristics that are common. (The international standard on reporting of measured road profiles (ISO8608, 1995) for example makes use of such models). These models are possible since road amplitudes at different wavelengths generally correlate, i.e. a road with high roughness levels at short wavelengths will also

have high roughness levels at long wavelengths. The implication is that different instruments that measure a variable that is related to roughness in some way will correlate with other systems to some extent. This is probably why different response-type systems with different frequency response characteristics correlate with IRI. It was found that the amount of correlation between two systems is a function of the amount of overlap in their frequency response characteristics.

Subsequently, the frequency response characteristics of the haul truck are compared to that of the standard quarter vehicle. Measured data and the characteristics determined in chapter 3 are useful for this purpose. Figure 5.2 shows the transfer function between the suspension response of the standard IRI quarter vehicle and the road input. Figure 5.3 shows the transfer function between the suspension strut response of the haul truck and the road input. The quarter vehicle transfer functions derived in Appendix C were used for these calculations and linear properties were assumed for the haul truck.

Two aspects are evident from figures 5.2 and 5.3. Firstly, the transfer function of the standard quarter vehicle shows good response up to about 14 Hz, while the transfer function that represents the haul truck shows good response up to about 5.5 Hz. Secondly, the transfer function of the haul truck has a large peak at 1 Hz, which would imply severe "tuning" to this frequency. However, the non-linear properties of the truck should prevent tuning to a certain frequency, since they are motion dependent. Effectively, the natural frequencies of the vehicle change as motion amplitudes change. The transfer function in figure 5.3 does also not include vehicle pitch.

Gillespie (1992) demonstrates that the acceleration spectrum of a vehicle provides some idea of the response gain of the system. Figure 5.4 shows the frequency spectrum of relative suspension strut acceleration that was calculated as the difference between acceleration measured on top of the barrel and acceleration measured on the wheel spindle. Measured data does not indicate severe tuning to any specific frequency, which is a desirable attribute for a road roughness measuring device.

Figure 5.4 indicates good response between about 0.5 and 7 Hz. Thus, although the response of the vehicle depends on the properties of the road and vehicle speed, it seems that the haul truck is responsive in a narrower frequency range than the standard quarter vehicle, which might have unfavourable consequences on calibration. However, there seems to be more correlation between the response characteristics of the haul truck and the standard quarter vehicle than between those of some recognised profilers and the standard quarter vehicle.

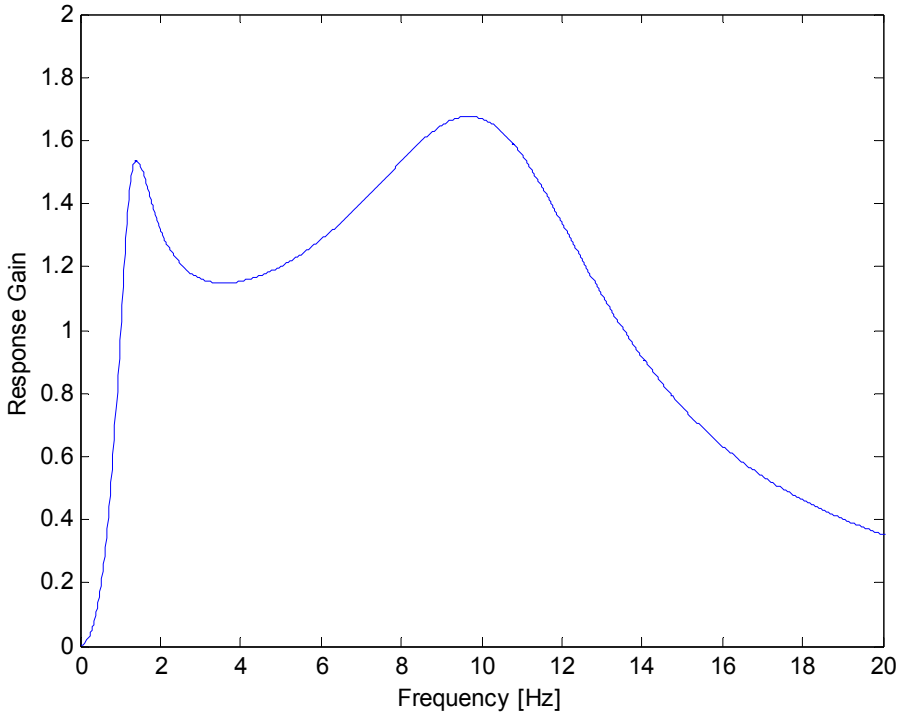

Figure 5.2 Standard quarter vehicle transfer function.

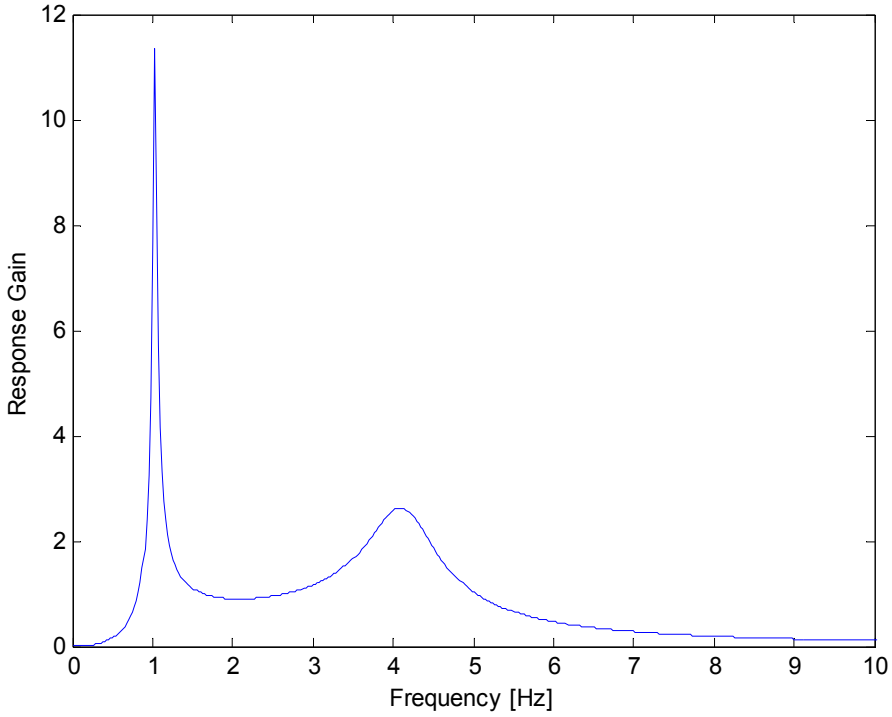

Figure 5.3 The approximated quarter vehicle transfer function of the haul truck.

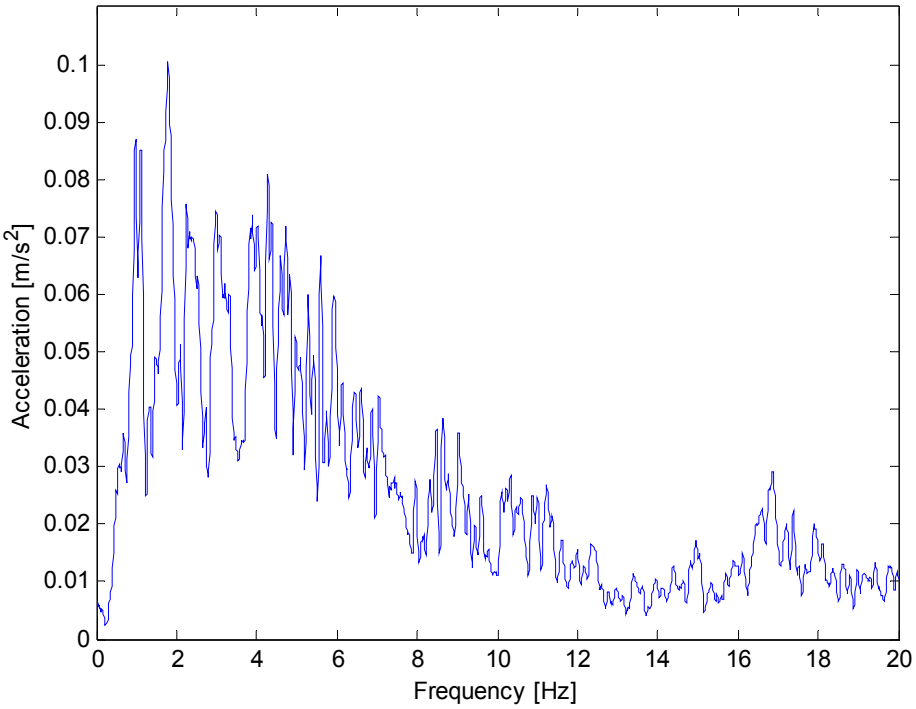

Figure 5.4 Haul truck suspension strut acceleration spectrum.

With regard to response characteristics, the success of the haul truck as a calibrated road roughness measuring device ultimately depends on the variation in the characteristics of the roads to be analysed.

5.4 Road roughness calculations

At this stage it is clear that the relative motion between the sprung and unsprung masses of the vehicle is the standard measurand of response-type profilers. Section 3.5.4 indicate how the relative motion of a haul truck suspension strut can be measured without requiring extensive modification to the vehicle, either through the use of its dynamic characteristics or possibly with a potentiometer.

This section analyses suspension strut motion that was measured during RDRM. Since data acquisition was centred around the primary purpose of this research, i.e. defect reconstruction, data was very limited for this kind of analysis. Nonetheless, rather than excluding this preliminary study from this dissertation, results are presented while deficiencies of data are outlined.

Calibration of a response-type system comprises the surveillance of a number of test sections with a class 1 or 2 device and the device that needs to be calibrated. IRI is

calculated from the class 1 or 2 measured profiles, after which a correlation between response-type system measurements and IRI is found. The calibration section should cover the range of roughness levels over which a correlation is sought. Bennett (2004) outlines the characteristics these sections should have. Some requirements are

- The section should be 200-300m long with adequate geometry before and after the section to ensure that they can be travelled at constant speed.
- The roughness should be fairly uniform along the length of the road. There should be no subsections with high roughness levels interspersed with subsections containing lower roughness.
- The surface should not be broken (i.e. potholes or bad depressions) so that the profiling survey can get the true profile.

These requirements for a calibration section were violated during RDRM. Firstly, the sections did not have a constant roughness since large defects were built into the road. Secondly, although it was attempted to pass defects at a constant speed, the speed at the start and end of the test sections were not constant. Finally, two sections of road with more or less the same properties are not enough. In an attempt to increase the range of roughness, the two sections were divided into smaller sections. The result was that sections with artificial defects had much higher roughness levels than the rest.

Despite these deficiencies, figure 5.7 compares road roughness calculated through haul truck suspension strut motion, measured at different speeds, to IRI, measured with a HSP. The road was divided into 10 m sections to have a sufficient range of roughness. Although the IRI equation was applied to measured data, the figure simply indicates units of m/km, since measurements were uncalibrated. Moreover, when the actual profile of the road was compared to HSP results it was evident that this device was not able to identify the large defects accurately. Therefore, it is unsure how accurate HSP readings were in rough sections of the road. Nonetheless, the figure indicates some correlation between HSP measurements and processed haul truck suspension strut motion.

5.5 Roughness levels measurable and speed effects

Section 2.9 shows that the suspension strut does not respond to low amplitude disturbances due to friction between the upper bearing and the barrel, and the lower bearing and the rod. Roads with low roughness levels should therefore not be assessable.

Since the response of a vehicle to road inputs is speed dependent, and haul trucks do operate at varying speeds, measurements will be influenced. However, Bennett (2004) mentions that since recently profilers also survey roads at varying speeds. Correlations between profiler response at different speeds and IRI are established, after which the

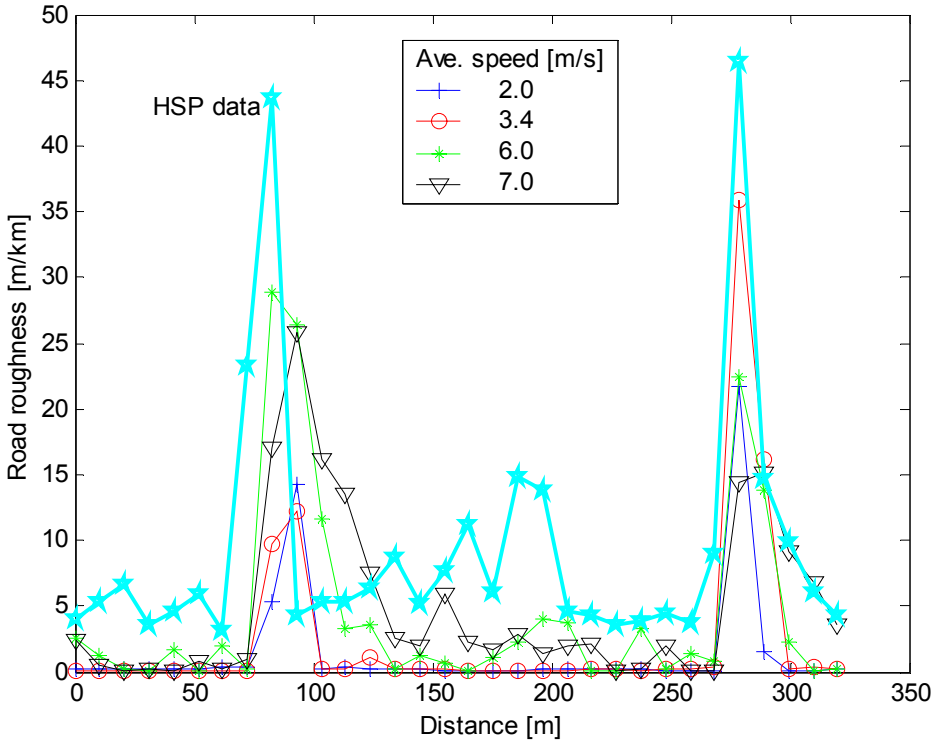

Figure 5.7 A comparison between HSP measured road roughness and processed haul truck suspension strut motion.

average speed over a test section is used to estimate IRI from these speed dependent correlations.

These aspects and others, such as the influence of the variance in load on the truck, and the possibility of correlation in spite of such rapidly changing properties need to be assessed through further experimental investigation.

Finally, accurate control over important properties might be difficult to establish in a mining environment where the primary purpose is not road profiling, as opposed to a specialised application where regular attendance to sensitive aspects is customary.

Chapter 6

Conclusions and recommendations

6.1 Conclusions

This dissertation identifies two possible ways of using haul truck response to aid haul road maintenance management. The first is by identifying the geometry of isolated defects. Typical defects are humps and ditches. The second is assessment of the condition of a section of road on a qualitative basis.

The problem of defect geometry reconstruction is approached from a mathematical modelling point of view. A modelling methodology that is based on dynamic equilibrium of an independent front unsprung mass of a haul truck is proposed. The truck used in this study was characterised in terms of its dynamic response properties. This included tyre stiffness, suspension stiffness and suspension damping characteristics. Subsequently, simulation models with two different levels of complexity were developed. These models established a basis in the understanding of truck behaviour pertaining to the problem of road defect reconstruction.

By utilising the simulation models it was specifically possible to

- Relate certain vehicle response features to specific vehicle characteristics, e.g. it is shown that vehicle pitch is responsible for the dominant motion at a frequency of 2 Hz when large defects are passed.
- Verify the accuracy of suspension strut force measurement as required by the modelling methodology.

Having verified these models against measured data, it is henceforth possible to

- Model different vehicle states, e.g. laden/unladen.
- Use these models in different analyses, e.g. tyre model studies.
- Adjust these models to describe other similar types of trucks. The ease of adjustment will depend on the amount of generic similarity between the vehicles.
- Conduct sensitivity analyses quickly and inexpensively.

Finally, the proposed modelling methodology is proven by reconstructing road defect geometries with an accuracy sufficient for the purpose of haul road maintenance management. To the author's knowledge, no such practically viable method previously existed. Moreover, the simplicity of this method and the fact that it requires basically no

alteration to the vehicle that can influence its primary purposes are advantageous for real-time implementation.

The importance of haul road roughness evaluations and the superiority of measurement over subjective evaluation or prediction is presented. A preliminary investigation into the viability of haul truck suspension strut motion as such a measure is conducted. Although the study primarily serves to introduce the concept, some points of reference are appropriate at this stage

- Accurate suspension motion measurement should be possible without disrupting the primary functions of the vehicle.
- Commonality between road characteristics is one reason correlation between measurements with different response-type systems is possible. This feature favours the concept of using the haul truck as a profiler. However, since road characteristics do differ to some extent, the amount of correlation between measurements with different systems is a function of the similarity between their frequency response characteristics. The haul truck seems to be responsive in a narrower frequency band than the standard quarter vehicle, which is unfavourable for good correlation. However, the accuracy of correlation ultimately depends on the variance in the characteristics of the roads under consideration.
- Processed haul truck suspension strut motion shows some correlation with high speed profilometer measurements.

6.2 Recommendations

From the primary goal of the work, although it was possible to reconstruct defects, some further work and refinement is recommended

- Investigation into the possible use of more sophisticated tyre models in both the inverse and the optimisation defect reconstruction approaches.
- Tyre forces in the longitudinal direction are substantial when large defects are encountered. Research into the possibilities of combining vertical and longitudinal tyre forces in a defect reconstruction method is suggested.
- Simulation and defect reconstruction results need to be verified for different states in which the vehicle can operate. For example, laden/unladen, accelerating or braking. Alternatively, an operating window should be defined, within which results can be validated.
- Investigation into the viability of alternative tyre force measurement methods might prove beneficial once the method is well established. Factors to consider at that stage should include the accuracy of measurement, financial viability and long-term implementation. Although expensive, instrumented hubs for example

have the advantage of measuring forces in the vertical and longitudinal directions of the tyre plane.

With regard to the second goal, that of qualitative road condition assessment, extensive experimental investigation is henceforth required. Further work is indicated to

- Investigate the feasibility of using haul trucks for profiling purposes by measuring suspension strut motion on various sections that adhere to the standards and comparing to class 1 or 2 measurements.
- Investigate the influence of rapidly changing factors on measurements, such as vehicle speed and load.
- During further investigation, the feasibility of practical implementation should be assessed continually as insight grows. For example, the sensitivity of measurements to changing vehicle properties, such as tyre pressure might reveal future difficulty in establishing adequate levels of control for calibrated profiling purposes in the mining environment.

Taken as a whole, this work recognises and establishes a foundation in the use of haul truck response as a tool in haul road maintenance management. This includes the successful reconstruction of road defects in terms of location, type and size that should aid haul road maintenance management and eventually lead to a decrease in the total operating cost of an opencast mine when implemented. Furthermore, the concept of haul truck response as a measure of road roughness is introduced through a preliminary investigation. Finally, the potential of using haul trucks revealed through this work can lead to the transformation of haul road maintenance management.

References

American Society of Testing and Materials (ASTM). *Terminology relating to vehicle-pavement systems*. (Definition E867).

Archondo-Callao, R.S. (1999a). Typical unpaved roads roughness predicted by the HDM-III model. *Infrastructure notes. Transport, Water and Urban Development. The World Bank: Transport No. RT-1,Washington, D.C.*

Archondo-Callao, R.S. (1999b). Unpaved roads' roughness estimation by subjective evaluation. *Infrastructure notes. Transport, Water and Urban Development. The World Bank: Transport No. RT-2,Washington, D.C.*

Bastow, D. (1980). *Car suspension and handling.* Devon: Pentech.

Bennett, C.R. (2004). Calibrating road roughness meters to IRI. Available from http://www.romdas.com/technical/tec-ciri.htm (Accessed 22 November 2004).

Cebon, D. (1999). *Handbook of vehicle road interaction.* Lisse: Swets & Zeitlinger.

Dierks, K. (1992). Technical aspects for appropriate low-volume roads in Namibia. *Doctoral thesis. Berlin: Technischen Universität Berlin.*

Els, P.S. (1993). *Die hitteprobleem op hidropneumatiese veer-en-demperstelsels* [The heat problem on hydro-pneumatic spring and damper systems]. Master's dissertation. Pretoria: University of Pretoria.

Gillespie, T.D., Sayers, M.W. & Segel, L. (1980). *Calibration of response-type road roughness measuring systems.* National Cooperative Highway Research Program Report 228. Transportation Research Board. National Research Council. Washington, D.C.

Gillespie, T.D. (1985). *Heavy truck ride.* Warrendale: Society of Automotive Engineers.

Gillespie, T.D. (1992). *Fundamentals of vehicle dynamics.* Warrendale: Society of Automotive Engineers.

Ibrahim, I.M., Crolla, D.A., Barton, D.C. (1996). Effect of frame flexibility on the ride vibration of trucks. *Computers & Structures*, Vol.58, No.4:709-713.

International Standard (ISO) 8608. (First Edition, 1995). *Mechanical vibration – road surface profiles – reporting of measured data.*

Johansson, I. & Gustavsson, M. (2000). *FE-based vehicle analysis of heavy trucks; Part I: methods and models.* Proceedings of the 2nd MSC Worldwide Automotive Conference, Michigan.

Komatsu 730E Machine & Statex III introduction training. Electric dump truck FST. (2003).

Mousseau, C.W. & Hulbert, G.M. (1996). The dynamic response of spindle forces produced by a tire impacting large obstacles in a plane. *Journal of Sound and Vibration*, 195(5):775-796.

Nevada Automotive Test Centre (NATC). (2004). http://www.natc-ht.com/Terrain_Profiling.htm (Accessed 22 November 2004).

Öijer, F. (2000). *FE-based vehicle analysis of heavy trucks; Part II: prediction of force histories for fatigue life analysis.* Proceedings of the 2nd MSC Worldwide Automotive Conference, Michigan.

Olley, M. (Edited by Milliken & Milliken, 2002). *Chassis design: principles and analysis.* Warrendale: Society of Automotive Engineers.

Park, S., Popov, A.A., Cole, D.J. (2004). Influence of soil deformation on off-road heavy vehicle suspension vibration. *Journal of Terramechanics,* 41(2004):41-68.

Sayers, M. & Gillespie, T.D. (1981). *The effect of suspension system nonlinearities on heavy truck vibration.* The dynamics of vehicles on roads and on tracks: Proceedings of the 7th IAVSD Symposium held at Cambridge University, Cambridge.

Sayers, M.W., Gillespie, T.D., Paterson, W.D.O. (1986). Guidelines for the conduct and calibration of road roughness measurements. *World Bank Technical Paper No. 46, The World Bank, Washington, D.C.*

Sayers, M.W. & Karamihas, S.M. (1998). *The little book of road profiling.* Available from http://www.umtri.umich.edu/erd/roughness/lit_book.pdf (Accessed 22 November 2004).

Sonntag, R.E., Borgnakke, C., Van Wylen, G.J. (1998). *Fundamentals of thermodynamics* (fifth edition). New York: John Wiley & Sons, Inc.

Thompson, R.J. & Visser, A.T. (2000). The functional design of surface mine haul roads. *The Journal of The South African Institute of Mining and Metallurgy*, May/June:169-180.

Thompson, R.J. & Visser, A.T. (2003). Mine haul road maintenance management systems. *The Journal of The South African Institute of Mining and Metallurgy*, June:303-312.

Thompson, R.J., Visser, A.T., Miller, R.E. & Lowe, T. (2003). *The development of a real-time mine road maintenance management system using haul truck and road vibration signature analysis.* 8th International Conference on Low Volume Roads, Nevada.

Appendix A

Classes of road profilers

Four classes of road profilers are presented in this section. The first two classes measure the actual profile of the road. The third class measures vehicle motion and is therefore a measure of the roughness of the road and not the actual profile. The fourth class comprises subjective evaluation methods and uncalibrated roughness measuring equipment. The classifications used in this dissertation are adapted from Bennett (2004) who cites Sayers et al. (1986). Slight modifications are made in this presentation.

Class 1 Precision profilers

These equipment produces the highest standard of accuracy for calculating the International Roughness Index (IRI) with a series of accurately measured elevation points closely spaced along the section. The elevations are measured at sampling intervals below 250 mm with a precision of less than 0.5 mm on smooth pavements. Examples of class 1 profilers are the rod-and-level survey, the TRL Beam and the DIPSTICK.

Class 2 Other profiling methods that produce a direct measure

A class 2 profiler is an instrument not capable of meeting the class 1 requirements for precision or sampling interval. The sampling intervals for these are a maximum of 500 mm with a precision on smooth roads of below 1 mm. Class 2 profilers are instruments such as high speed profilometers (HSP).

Class 3 IRI estimates from response-type measurements or simple profilers

This class includes instruments that measure the relative displacement between the vehicle body and the axle. In addition to response-type systems, instruments such as the MERLIN or rolling straightedge are also class 3 devices.

Class 4 Subjective ratings

This comprises subjective evaluation of road roughness based on driving along the road or a visual survey. This can be assisted through the use of an uncalibrated roughness meter.

Appendix B

Vehicle coordinate system

The coordinate system shown in figure B.1 is used consistently in this dissertation. Equations of motion are mostly derived with these directions of motions defined at the centre of gravity of components.

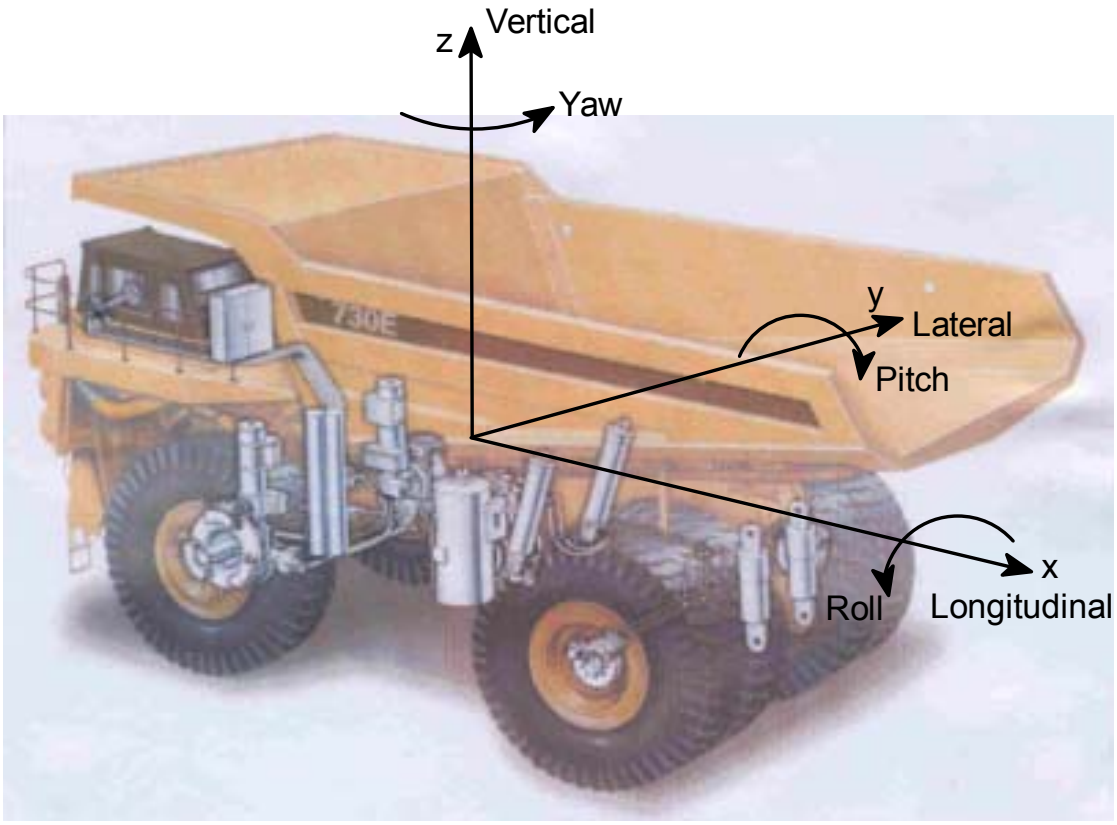

Figure B.1 Vehicle body coordinate system (drawing adapted from Komatsu 730E Machine & Statex III introduction training, 2003).

Appendix C

Quarter vehicle transfer functions

The Laplace transform of a function $x(t)$ exists if the transformation integral

$$X(s) = \int_{0^-}^{\infty} x(t)e^{-st}dt \tag{C.1}$$

converges. Closed form transformation solutions have been derived and are frequently in use. With regard to linear differential equations

$$L\{\dot{x}(t)\} = sX(s) - x(0^-) \tag{C.2}$$

$$L\{\ddot{x}(t)\} = s^2X(s) - sx(0^-) - \dot{x}(0^-) \tag{C.3}$$

For transfer functions all initial conditions are zero. Therefore

$$x(0^-) = \dot{x}(0^-) = 0$$

Figure C.1 represents the quarter vehicle model in figure 2.2. Forces acting on the unsprung mass F_u (these may arise from tyre/wheel non-uniformities) and forces acting on the sprung mass F_s (these may result from on-board sources) are added. The three inputs then become the vertical road displacement z_r, F_u and F_s. The outputs are the displacement of the unsprung mass z_u and the displacement of the sprung mass z_s.

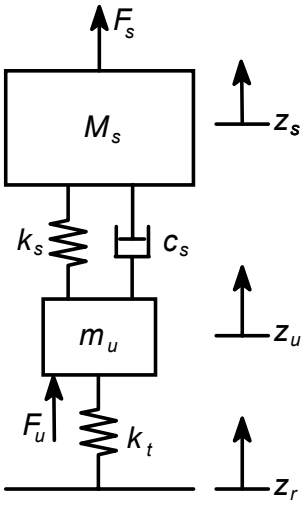

Figure C.1 Quarter vehicle model.

The equations of motion describing this system are

$$M_s\ddot{z}_s = -k_s(z_s - z_u) - c_s(\dot{z}_s - \dot{z}_u) + F_s \tag{C.4}$$

$$m_u\ddot{z}_u = k_s(z_s - z_u) + c_s(\dot{z}_s - \dot{z}_u) - k_t(z_u - z_r) + F_u \tag{C.5}$$

Through equations C.2 and C.3, with all initial condition zero, equations C.4 and C.5 are transformed to the Laplace domain

$$(M_s s^2 + c_s s + k_s)Z_s(s) = (c_s s + k_s)Z_u(s) + F_s(s) \tag{C.6}$$

$$(m_u s^2 + c_s s + [k_s + k_t])Z_u(s) = (c_s s + k_s)Z_s(s) + k_t Z_r(s) + F_u(s) \tag{C.7}$$

One advantage of using the Laplace transform is that differential equations transform to complex algebraic equations. This is seen in equations C.6 and C.7. These equations will be used to derive transfer functions between each respective input and output. Henceforth, $Z_u(s)$ will be presented by Z_u and $Z_s(s)$ by Z_s.

Firstly, the transfer functions between Z_s and respectively Z_r, F_u and F_s are derived. Z_u is eliminated by rearranging C.7 and substituting into C.6

$$Z_u = \frac{(c_s s + k_s)Z_s + k_t Z_r + F_u}{m_u s^2 + c_s s + [k_s + k_t]}$$

$$(M_s s^2 + c_s s + k_s)Z_s = (c_s s + k_s)\left[\frac{(c_s s + k_s)Z_s + k_t Z_r + F_u}{m_u s^2 + c_s s + [k_s + k_t]}\right] + F_s \tag{C.8}$$

Rearranging C.8

$$\begin{aligned}&\{M_s s^2 + c_s s + k_s)(m_u s^2 + c_s s + [k_s + k_t]) - (c_s s + k_s)^2\}Z_s = \\ &\{(c_s s + k_s)k_t\}Z_r + \{c_s s + k_s\}F_u + \{m_u s^2 + c_s s + [k_s + k_t]\}F_s\end{aligned} \tag{C.9}$$

Multiplying parenthesis and grouping terms

$$\begin{aligned}&\{M_s m_u s^4 + (M_s c_s + m_u c_s)s^3 + (M_s[k_s + k_t] + m_u k_s)s^2 + k_t c_s s + k_s k_t\}Z_s = \\ &\{k_t c_s s + k_s k_t\}Z_r + \{M_s(c_s s + k_s)\}F_u/M_s + \{M_s(m_u s^2 + c_s s + [k_s + k_t])\}F_s/M_s\end{aligned} \tag{C.10}$$

Then the transfer functions are

$$\frac{Z_s}{Z_r} = \frac{k_t c_s s + k_s k_t}{M_s m_u s^4 + (M_s c_s + m_u c_s)s^3 + (M_s[k_s + k_t] + m_u k_s)s^2 + k_t c_s s + k_s k_t} \tag{C.11}$$

$$\frac{Z_s}{F_u/M_s} = \frac{M_s(c_s s + k_s)}{M_s m_u s^4 + (M_s c_s + m_u c_s)s^3 + (M_s[k_s + k_t] + m_u k_s)s^2 + k_t c_s s + k_s k_t} \quad \text{(C.12)}$$

$$\frac{Z_s}{F_s/M_s} = \frac{M_s(m_u s^2 + c_s s + [k_s + k_t])}{M_s m_u s^4 + (M_s c_s + m_u c_s)s^3 + (M_s[k_s + k_t] + m_u k_s)s^2 + k_t c_s s + k_s k_t} \quad \text{(C.13)}$$

Eliminate Z_s by rearranging C.6 and substituting into C.7

$$Z_s = \frac{(c_s s + k_s)Z_u + F_s}{(M_s s^2 + c_s s + k_s)}$$

$$(m_u s^2 + c_s s + [k_s + k_t])Z_u = (c_s s + k_s)[\frac{(c_s s + k_s)Z_u + F_s}{(M_s s^2 + c_s s + k_s)}] + k_t Z_r + F_u \quad \text{(C.14)}$$

Rearranging C.14

$$\{(m_u s^2 + c_s s + [k_s + k_t])(M_s s^2 + c_s s + k_s) - (c_s s + k_s)^2\}Z_u = \{(M_s s^2 + c_s s + k_s)k_t\}Z_r + \{M_s s^2 + c_s s + k_s\}F_u + \{c_s s + k_s\}F_s \quad \text{(C.15)}$$

Multiplying parenthesis and grouping terms

$$\{M_s m_u s^4 + (M_s c_s + m_u c_s)s^3 + (M_s[k_s + k_t] + m_u k_s)s^2 + k_t c_s s + k_s k_t\}Z_u = \{(M_s s^2 + c_s s + k_s)k_t\}Z_r + \{M_s(M_s s^2 + c_s s + k_s)\}F_u/M_s + \{M_s(c_s s + k_s)\}F_s/M_s \quad \text{(C.16)}$$

Then the transfer functions are

$$\frac{Z_u}{Z_r} = \frac{(M_s s^2 + c_s s + k_s)k_t}{M_s m_u s^4 + (M_s c_s + m_u c_s)s^3 + (M_s[k_s + k_t] + m_u k_s)s^2 + k_t c_s s + k_s k_t} \quad \text{(C.17)}$$

$$\frac{Z_u}{F_u/M_s} = \frac{M_s(M_s s^2 + c_s s + k_s)}{M_s m_u s^4 + (M_s c_s + m_u c_s)s^3 + (M_s[k_s + k_t] + m_u k_s)s^2 + k_t c_s s + k_s k_t} \quad \text{(C.18)}$$

$$\frac{Z_u}{F_s/M_s} = \frac{M_s(c_s s + k_s)}{M_s m_u s^4 + (M_s c_s + m_u c_s)s^3 + (M_s[k_s + k_t] + m_u k_s)s^2 + k_t c_s s + k_s k_t} \quad \text{(C.19)}$$

If inputs are harmonic, $s = i\omega$ and equations C.11, C.12, C.13, C.17, C.18 and C.19 change to equations C.20, C.21, C.22, C.23, C.24 and C.25. These transfer function are only valid for steady state response.

$$\frac{Z_s(i\omega)}{Z_r(i\omega)} = \frac{ik_t c_s \omega + k_s k_t}{M_s m_u \omega^4 - i(M_s c_s + m_u c_s)\omega^3 - (M_s[k_s + k_t] + m_u k_s)\omega^2 + ik_t c_s \omega + k_s k_t} \quad \text{(C.20)}$$

$$\frac{Z_s(i\omega)}{F_u(i\omega)/M_s} = \frac{M_s(ic_s\omega + k_s)}{M_s m_u\omega^4 - i(M_s c_s + m_u c_s)\omega^3 - (M_s[k_s + k_t] + m_u k_s)\omega^2 + ik_t c_s\omega + k_s k_t} \tag{C.21}$$

$$\frac{Z_s(i\omega)}{F_s(i\omega)/M_s} = \frac{M_s(-m_u\omega^2 + ic_s\omega + [k_s + k_t])}{M_s m_u\omega^4 - i(M_s c_s + m_u c_s)\omega^3 - (M_s[k_s + k_t] + m_u k_s)\omega^2 + ik_t c_s\omega + k_s k_t} \tag{C.22}$$

$$\frac{Z_u(i\omega)}{Z_r(i\omega)} = \frac{(-M_s\omega^2 + ic_s\omega + k_s)k_t}{M_s m_u\omega^4 - i(M_s c_s + m_u c_s)\omega^3 - (M_s[k_s + k_t] + m_u k_s)\omega^2 + ik_t c_s\omega + k_s k_t} \tag{C.23}$$

$$\frac{Z_u(i\omega)}{F_u(i\omega)/M_s} = \frac{M_s(-M_s\omega^2 + ic_s\omega + k_s)}{M_s m_u\omega^4 - i(M_s c_s + m_u c_s)\omega^3 - (M_s[k_s + k_t] + m_u k_s)\omega^2 + ik_t c_s\omega + k_s k_t} \tag{C.24}$$

$$\frac{Z_u(i\omega)}{F_s(i\omega)/M_s} = \frac{M_s(ic_s\omega + k_s)}{M_s m_u\omega^4 - i(M_s c_s + m_u c_s)\omega^3 - (M_s[k_s + k_t] + m_u k_s)\omega^2 + ik_t c_s\omega + k_s k_t} \tag{C.25}$$

In terms of acceleration

$$\frac{\ddot{Z}_s(i\omega)}{\ddot{Z}_r(i\omega)} = \frac{-\omega^2 Z_s(i\omega)}{-\omega^2 Z_r(i\omega)} = \frac{Z_s(i\omega)}{Z_r(i\omega)} \tag{C.26}$$

$$\frac{\ddot{Z}_s(i\omega)}{F_u(i\omega)/M_s} = \frac{-\omega^2 Z_s(i\omega)}{F_u(i\omega)/M_s} = \frac{-M_s(ic_s\omega + k_s)\omega^2}{M_s m_u\omega^4 - i(M_s c_s + m_u c_s)\omega^3 - (M_s[k_s + k_t] + m_u k_s)\omega^2 + ik_t c_s\omega + k_s k_t} \tag{C.27}$$

$$\frac{\ddot{Z}_s(i\omega)}{F_s(i\omega)/M_s} = \frac{-\omega^2 Z_s(i\omega)}{F_s(i\omega)/M_s} = \frac{-M_s(-m_u\omega^2 + ic_s\omega + [k_s + k_t])\omega^2}{M_s m_u\omega^4 - i(M_s c_s + m_u c_s)\omega^3 - (M_s[k_s + k_t] + m_u k_s)\omega^2 + ik_t c_s\omega + k_s k_t} \tag{C.28}$$

$$\frac{\ddot{Z}_u(i\omega)}{\ddot{Z}_r(i\omega)} = \frac{-\omega^2 Z_u(i\omega)}{-\omega^2 Z_r(i\omega)} = \frac{Z_u(i\omega)}{Z_r(i\omega)} \tag{C.29}$$

$$\frac{\ddot{Z}_u(i\omega)}{F_u(i\omega)/M_s} = \frac{-\omega^2 Z_u(i\omega)}{F_u(i\omega)/M_s} = \frac{-M_s(-M_s\omega^2 + ic_s\omega + k_s)\omega^2}{M_s m_u\omega^4 - i(M_s c_s + m_u c_s)\omega^3 - (M_s[k_s + k_t] + m_u k_s)\omega^2 + ik_t c_s\omega + k_s k_t} \tag{C.30}$$

$$\frac{\ddot{Z}_u(i\omega)}{F_s(i\omega)/M_s} = \frac{-\omega^2 Z_u(i\omega)}{F_s(i\omega)/M_s} = \frac{-M_s(ic_s\omega + k_s)\omega^2}{M_s m_u\omega^4 - i(M_s c_s + m_u c_s)\omega^3 - (M_s[k_s + k_t] + m_u k_s)\omega^2 + ik_t c_s\omega + k_s k_t} \tag{C.31}$$

Appendix D

Signal integration and differentiation

This section discusses integration and differentiation of low-frequency signals such as those that were measured on the haul truck during this research. Suspension strut motion is very useful for this purpose since both relative acceleration and displacement were measured. Hence, it is possible to assess the accuracy of integration and differentiation through mutual comparison.

Figure D.1a shows the relative displacement of the suspension strut that was measured with a potentiometer. This signal was differentiated twice to obtain acceleration. Figure D.1b compares the differentiated signal to relative suspension strut acceleration (measured as explained below). Very good resemblance is clear.

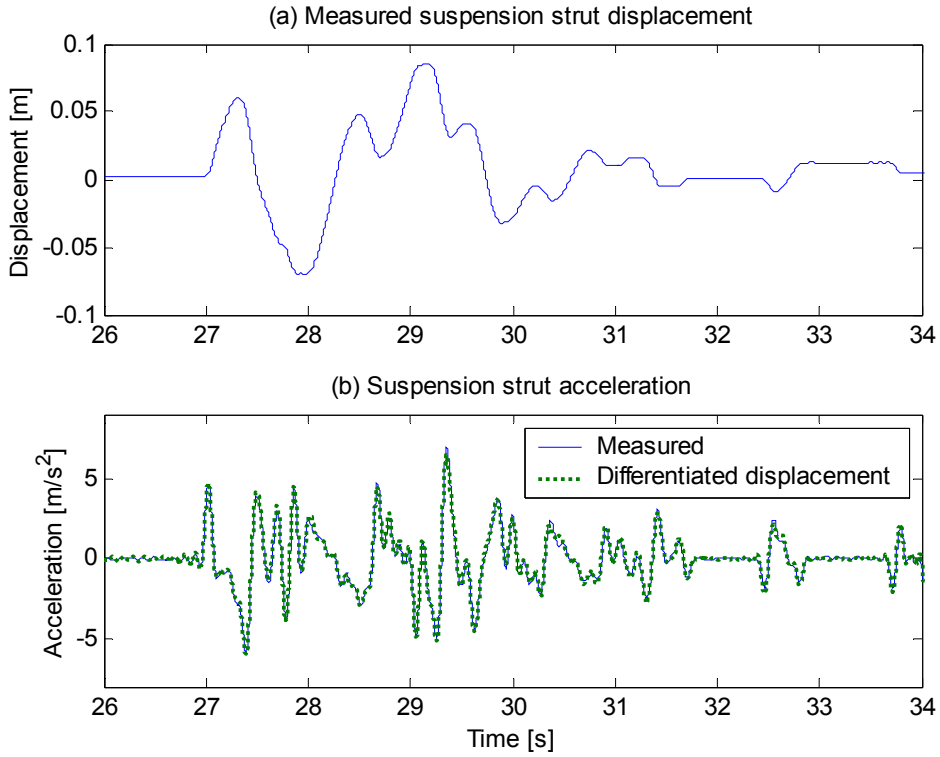

Figure D.1 Signal differentiation.

Figure D.2a shows the difference between vertical acceleration that was measured on top of the suspension barrel and acceleration that was measured on the unsprung mass, i.e. the relative acceleration of the suspension strut. This signal was integrated twice, without

any high-pass filtering. Figure D.2b compares the integrated signal to the relative displacement that was measured with the potentiometer. Low frequency drift is present and correlation is not good at all.

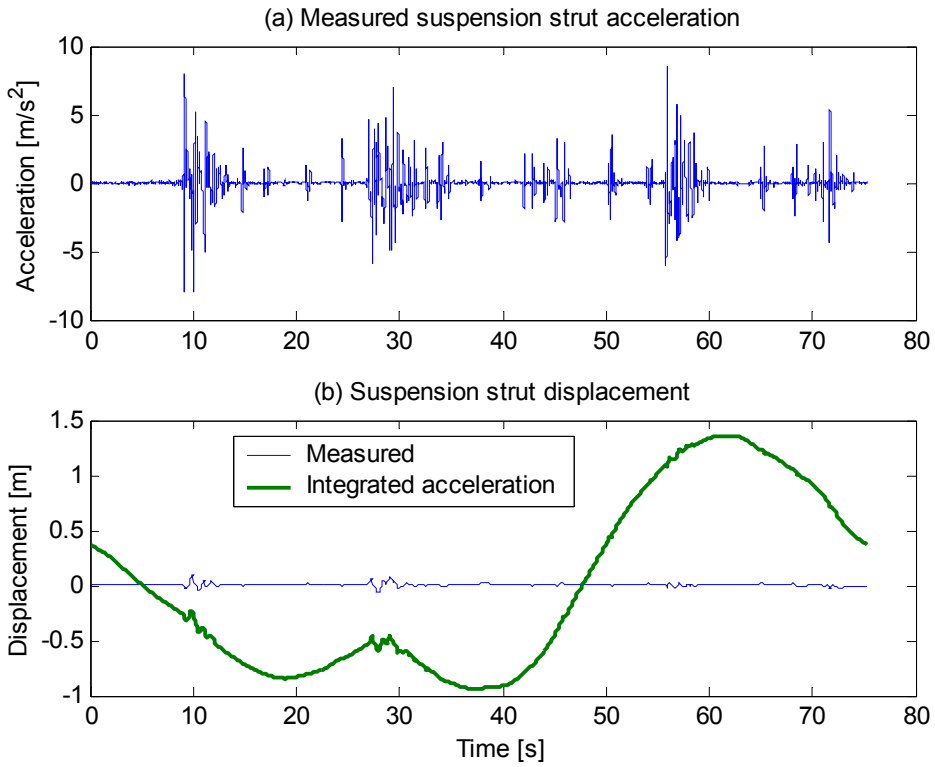

Figure D.2 Signal integration with no lower cut-off frequency.

Figure D.3a again shows the measured relative suspension strut acceleration, while figure D.3b compares integrated acceleration to measured displacement, in which case a lower cut-off frequency of 0.45 Hz was used. Correlation is better than in figure D.2b. The lower cut-off frequency of 0.45 Hz was generally found best to eliminate low frequency content that caused severe drift, without distorting characteristic features severely.

Different periods of the signals were each time used for the purpose of illustration. It is evident that the truck response signals can be differentiated accurately, while integration is problematic. It is further worth noting that for each of the signals, frequency content above 10 Hz was discarded. Neglecting to do this does not influence integration severely. However, differentiation is sensitive to high frequency noise and it was therefore important to set an appropriate higher cut-off limit. A cut-off frequency of 10 Hz is probably not the highest possible to ensure accurate differentiation, although clearly sufficient in the present case.

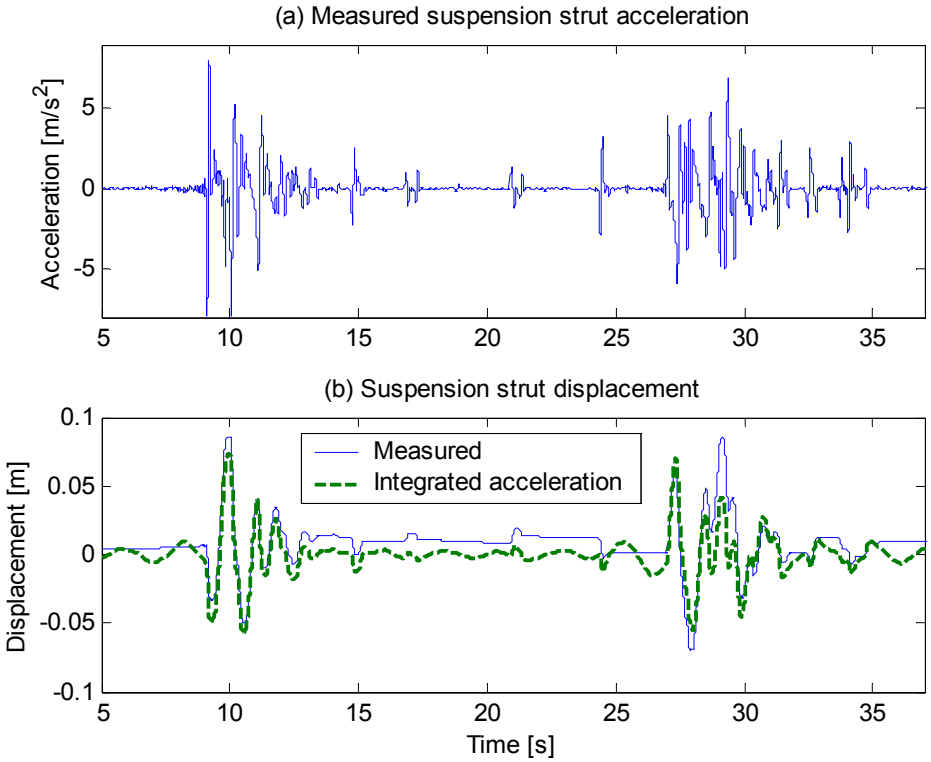

Figure D.3. Signal integration with a 0.45 Hz cut-off frequency.

Appendix E

Quarter vehicle modelling results

Figure 4.13 compares quarter vehicle modelling results to measured data for the truck driven over two closely spaced half-sine humps. This appendix compares measured responses to simulation results obtained with the same quarter vehicle model for driving over two larger defects.

Defect 1

Figure E.1a shows a half-sine hump in the time domain, as experienced by the truck. Figure E.1b shows the defect in the spatial domain. The circular rigid treadband tyre filtering procedure explained in section 4.2 was already applied at this stage. The defect has a height of 0.15 m and a width of 3.2 m. Figure E.2 compares modelling results to measured response.

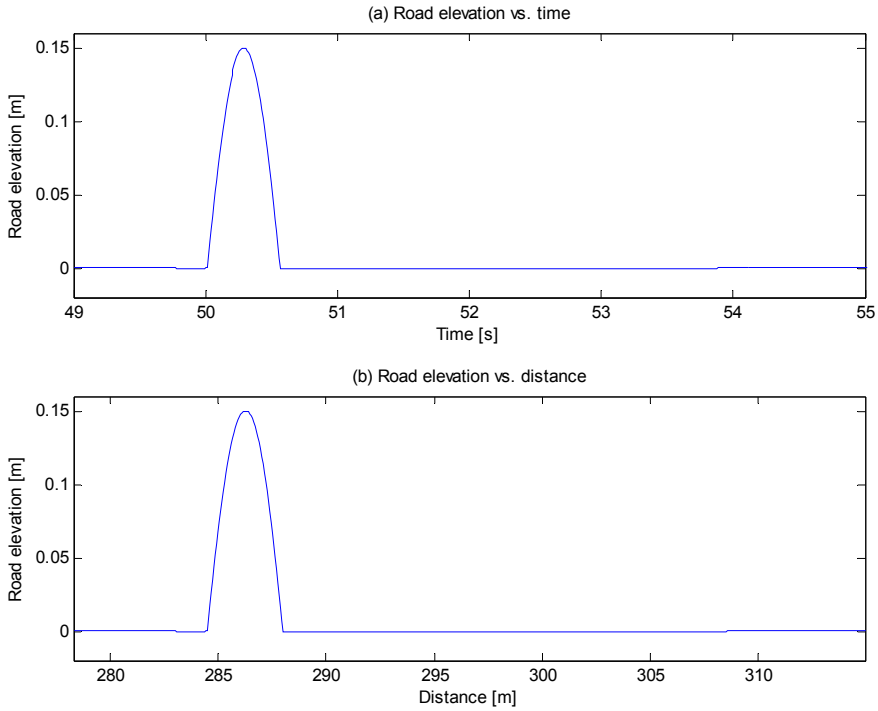

Figure E.1 Defect 1: Rigid treadband-filtered road input.

Defect 2

Figure E.3a shows a ditch that is directly followed by a hump in the time domain, as experienced by the truck. Figure E.3b shows the defect in the spatial domain. The circular rigid treadband tyre filtering procedure was already applied at this stage. Both the ditch and hump are 4.2 m wide, while the ditch is 250 mm deep and the hump is 250 mm high. Thus, the two defects form one cycle of a sinusoidal wave with an amplitude of 250 mm

and a wavelength of 8.4 m. Figure E.4 compares modelling results to measured responses.

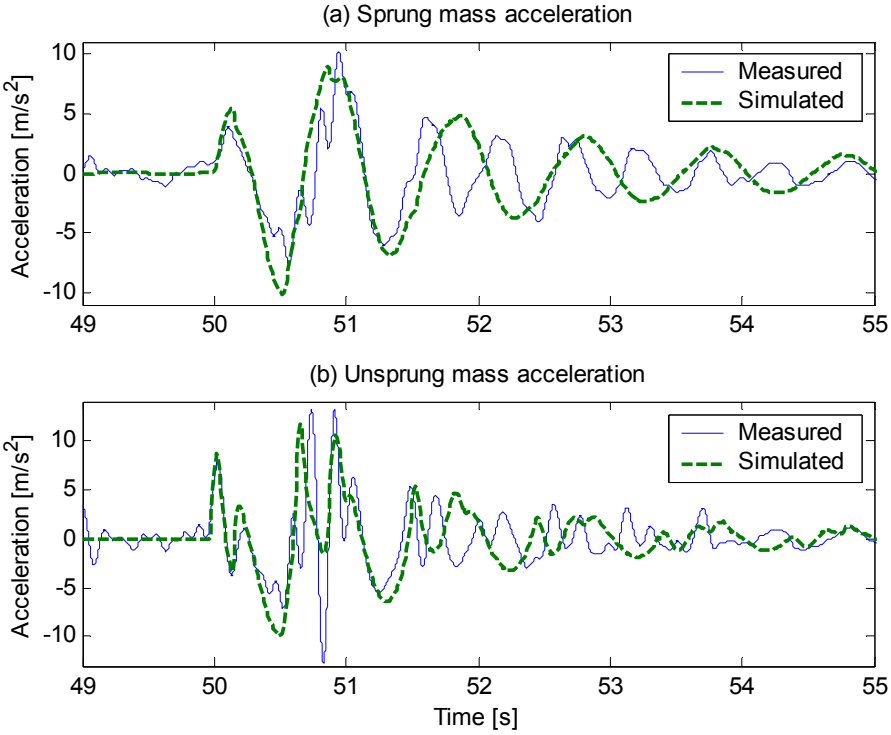

Figure E.2 Defect 1: Quarter vehicle modelling acceleration responses compared to measured data.

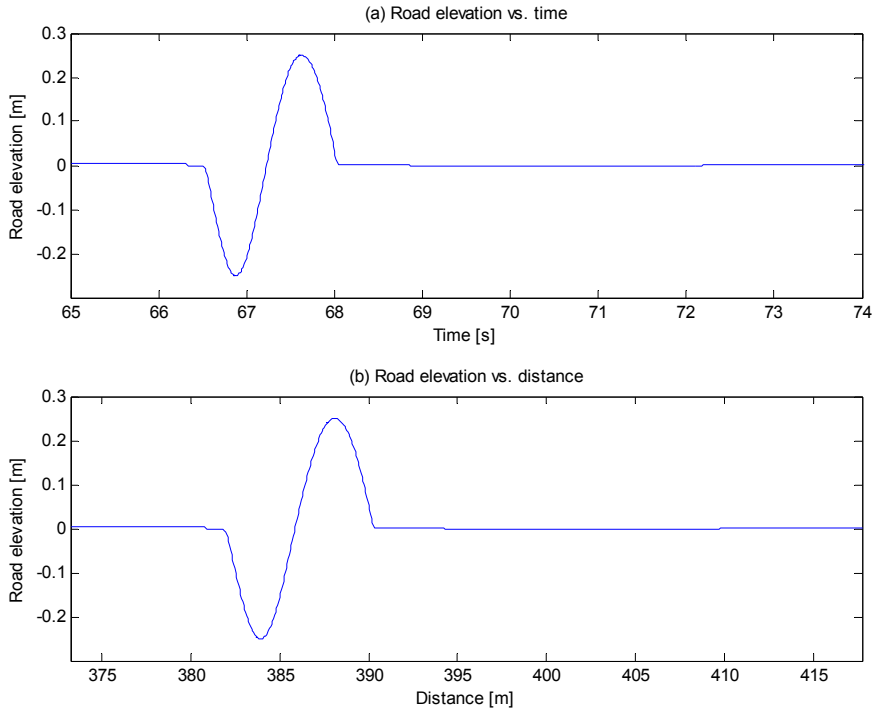

Figure E.3 Defect 2: Rigid treadband-filtered road input.

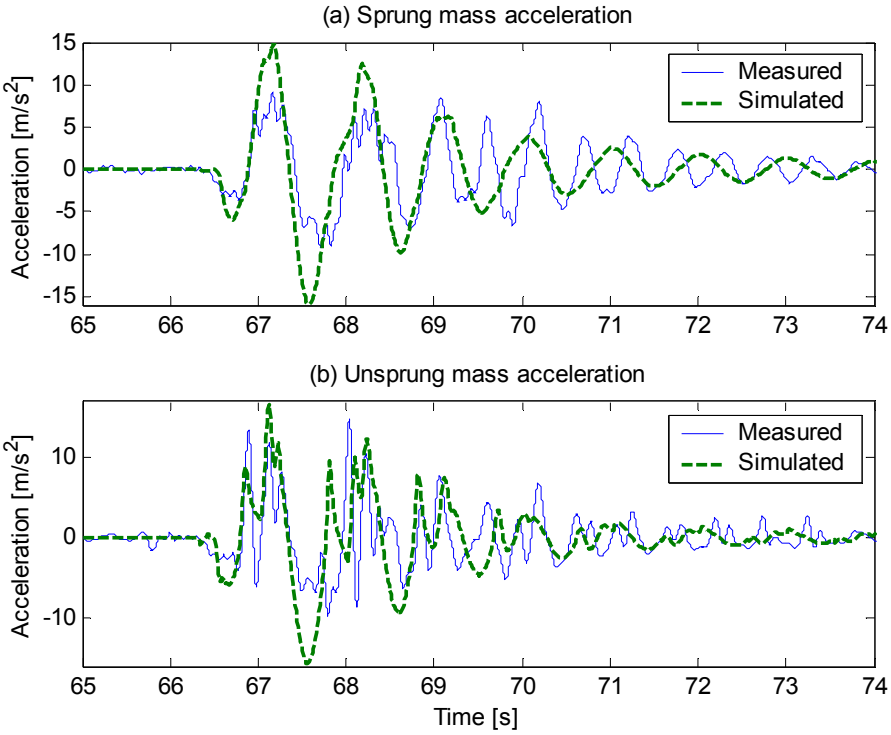

Figure E.4 Defect 2: Quarter vehicle modelling acceleration responses compared to measured data.

Appendix F

7DOF vehicle modelling results

Figure 4.20 compares 7DOF vehicle modelling results to measured data for the truck driven over two closely spaced half-sine humps. This appendix compares measured responses to simulation results obtained with the same 7DOF vehicle model for driving over the two larger defects in figures E.1 and E.3.

Defect 1

Figures F.1 compares measured and simulated acceleration responses for the truck driven over the defect in figure E.1.

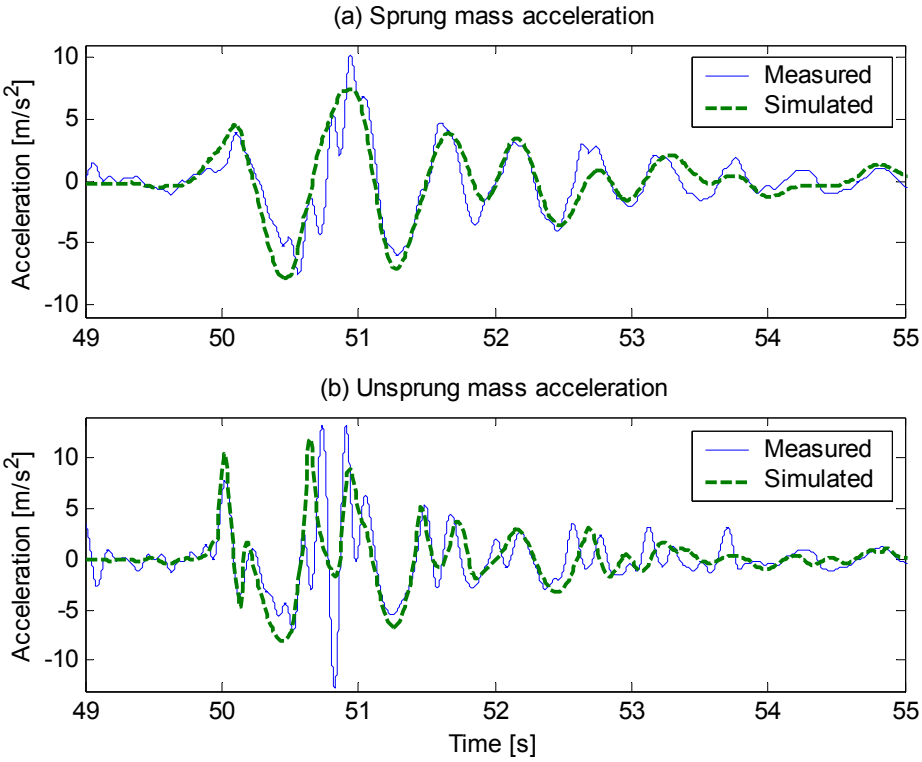

Figure F.1 Defect 1: 7DOF vehicle modelling acceleration responses compared to measured data.

Defect 2

Figures F.2 compares measured and simulated acceleration responses for the truck driven over the defect in figure E.3.

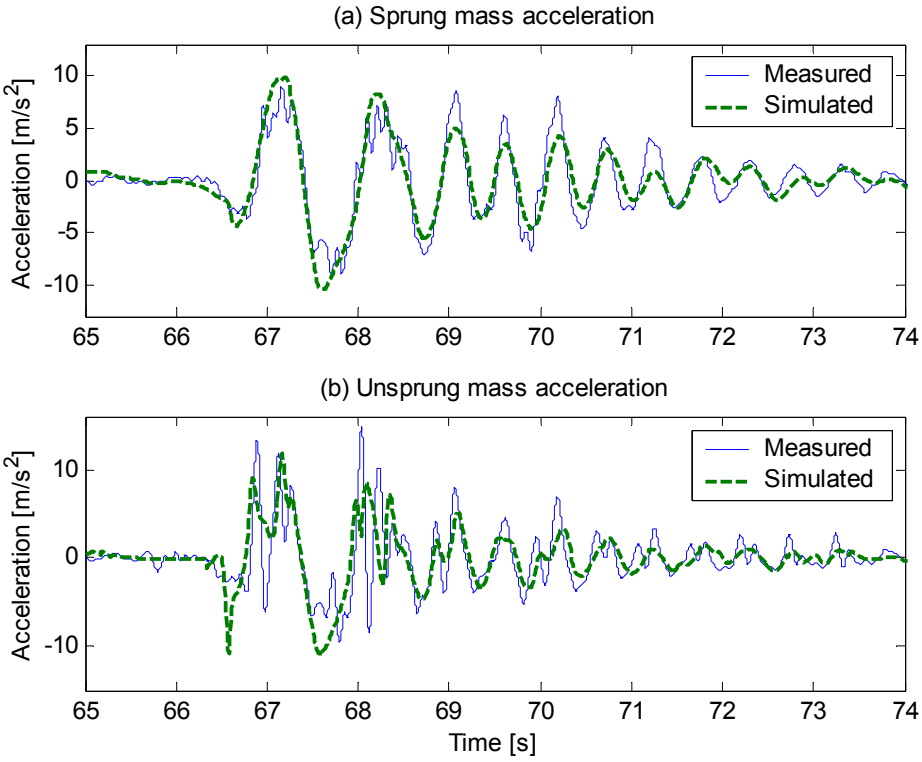

Figure F.1 Defect 2: 7DOF vehicle modelling acceleration responses compared to measured data.

Appendix G

Parameter sensitivity analysis

The sensitivity of the truck to parameter changes is assessed in this appendix through the use of the 7DOF vehicle model discussed in section 4.8. The parameters included in this study are the tyre stiffness value k_t, sprung mass value M_s, suspension strut stiffness constant C, suspension damping parameter $C_{damping}$ and the sprung mass pitch radius of gyration k_{pitch}. The simulated unsprung and sprung mass accelerations in figure 4.20 are each time reproduced and compared to simulation results for both decreasing and increasing each of the parameters by 10%. Results are presented in figures G.1 to G.5.

No significant change in acceleration response is seen for a 10 % change in any of these parameters. The parameters that have the greatest influence are the tyre spring stiffness, sprung mass and sprung mass pitch radius of gyration.

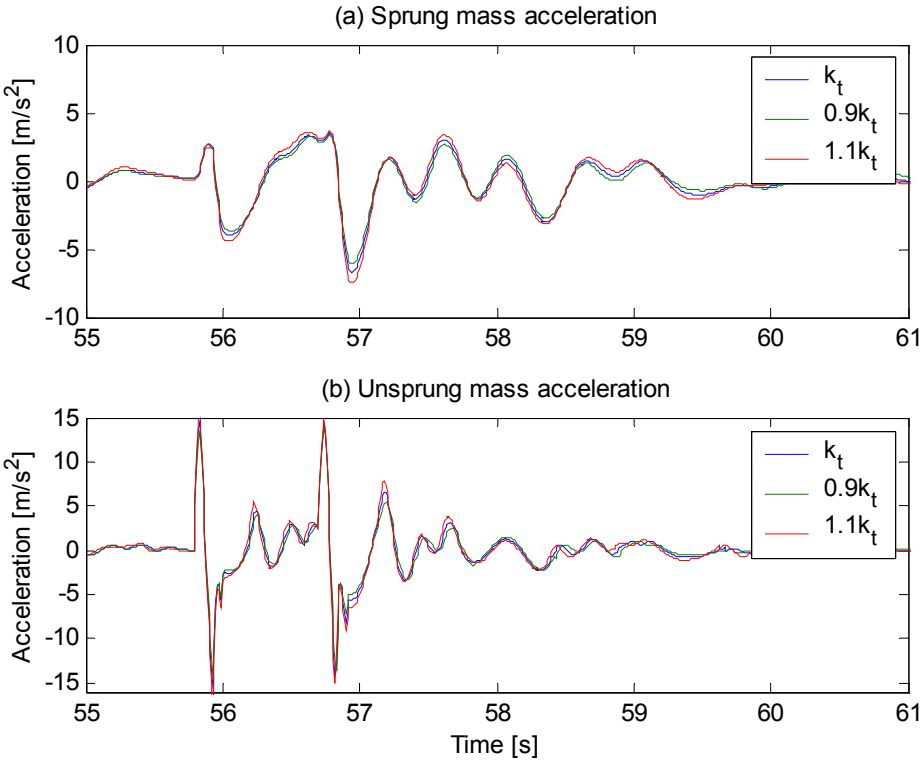

Figure G.1 7DOF vehicle modelling results when altering the tyre stiffness value k_t with 10%.

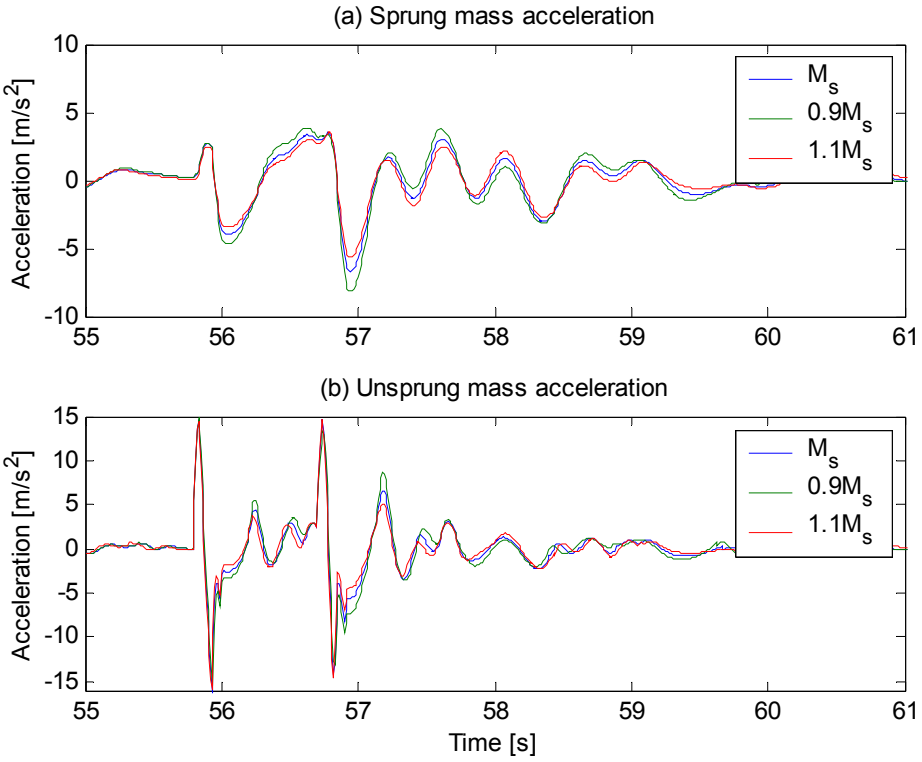

Figure G.2 7DOF vehicle modelling results when altering the sprung mass value M_s with 10%.

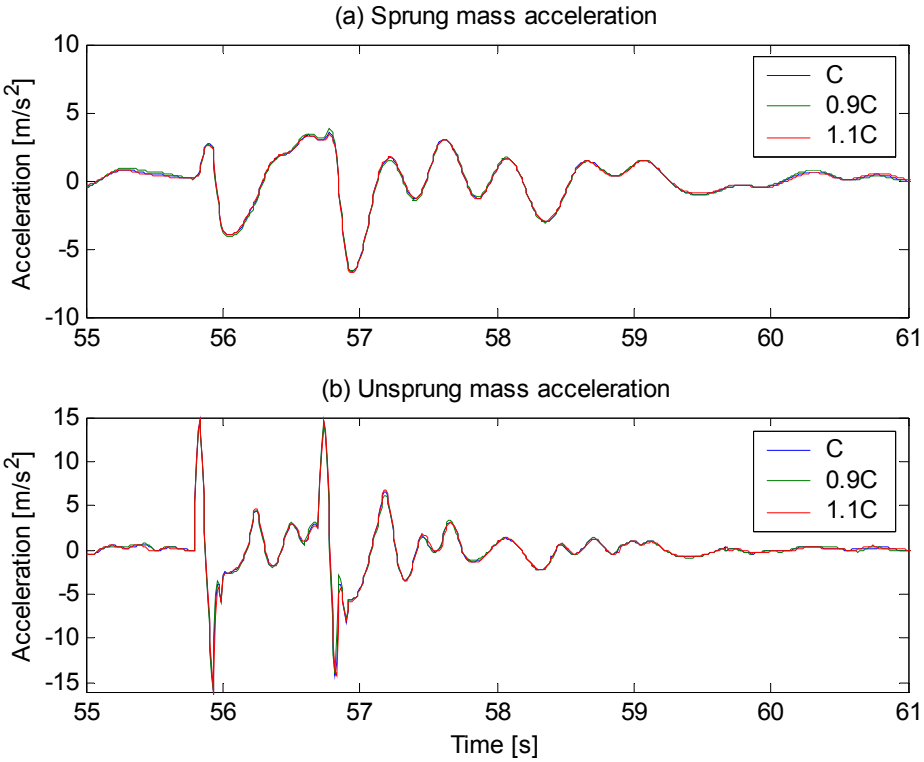

Figure G.3 7DOF vehicle modelling results when altering the suspension stiffness constant C with 10 %.

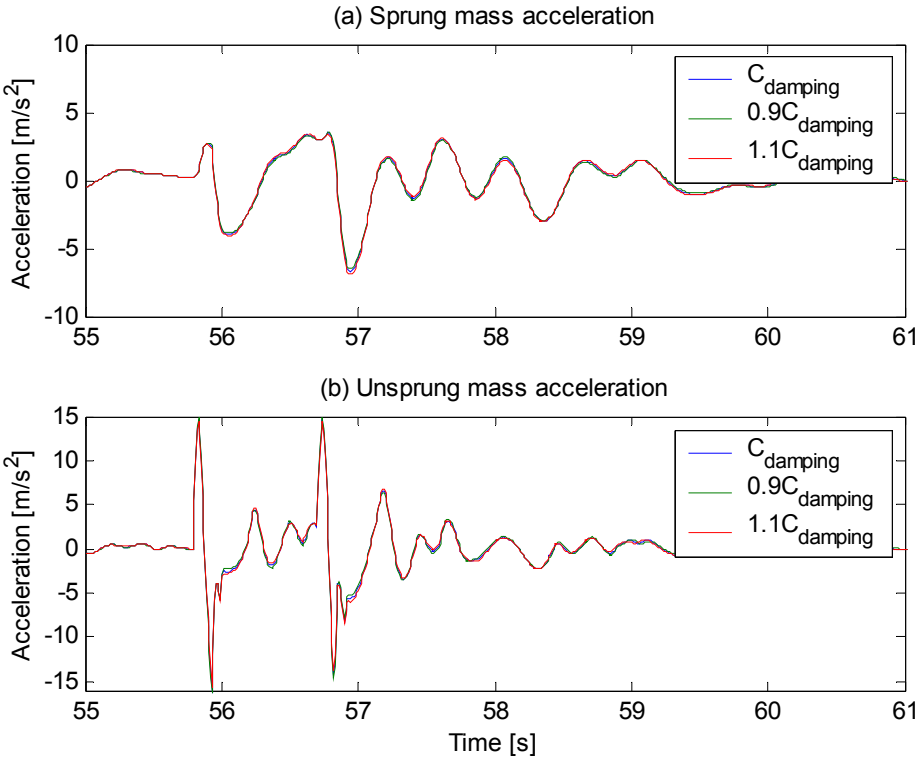

Figure G.4 7DOF vehicle modelling results when altering the suspension damping parameter $C_{damping}$ with 10%.

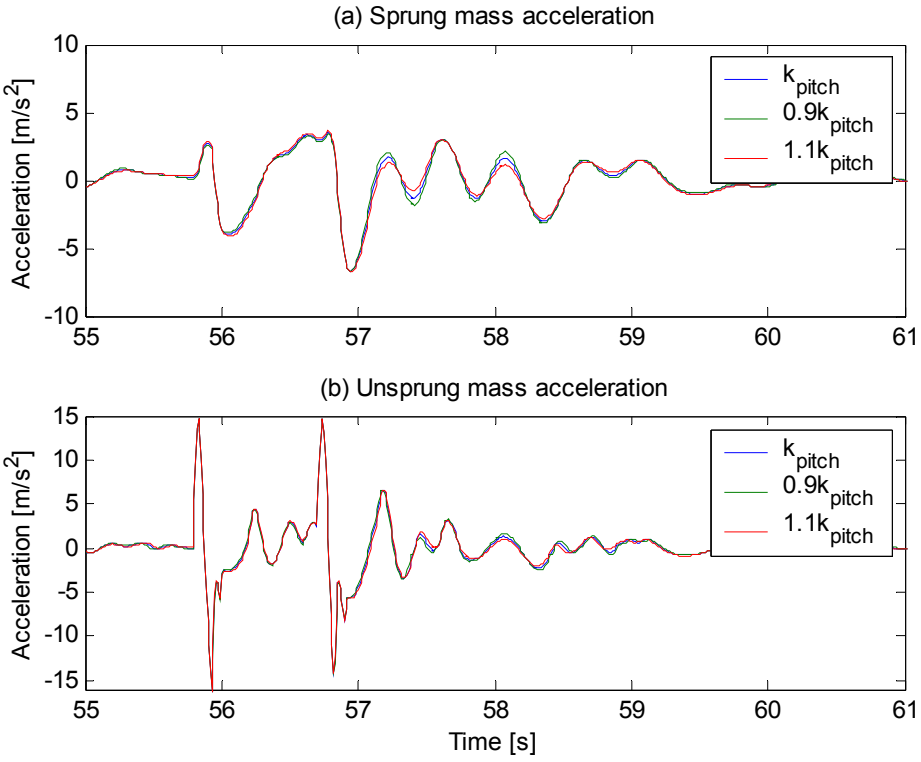

Figure G.5 7DOF vehicle modelling results when altering the pitch radius of gyration k_{pitch} with 10%.

Appendix H

Defect reconstruction results

The reconstructed defects presented in section 4.10 are reproduced in this appendix using a tyre stiffness value of $k_t = 5 \times 10^6 \, N/m$. Figure H.1 and H.2 respectively compare the reconstructed west and east section defects geometries to the simulated geometries of the actual defects.

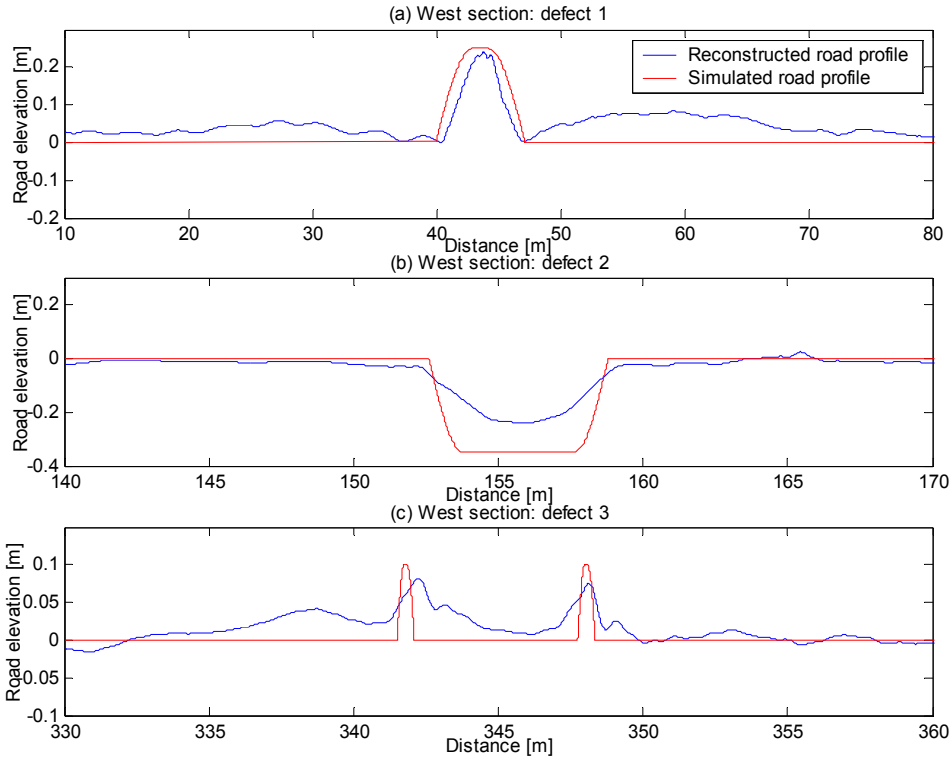

Figure H.1 Comparison between the simulated and reconstructed west section defects using a tyre stiffness $k_t = 5 \times 10^6 \, N/m$.

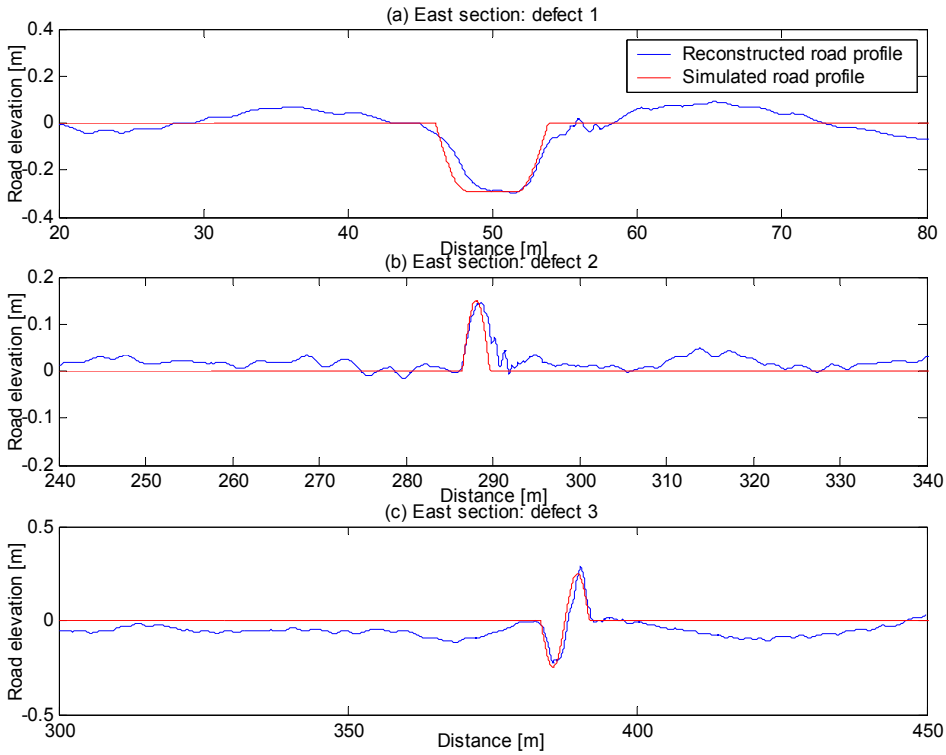

Figure H.2 Comparison between the simulated and reconstructed east section defects using a tyre stiffness $k_t = 5 \times 10^6\ N/m$.